Control of supersonic flow around bodies by means of a pulsed heat source

S. V. Guvernyuk and A. B. Samoĭlov

Institute of Mechanics at the M. V. Lomonosov State University, Moscow
(Submitted November 25, 1996)
Pis'ma Zh. Tekh. Fiz. **23**, 1–8 (May 12, 1997)

The influence of an external, pulse-periodic, energy supply source on the aerodynamic characteristics of a hemisphere positioned downstream is simulated. [S1063-7850(97)00105-5]

1. INTRODUCTION

It has been established theoretically[1] that when an external, continuous source of heat release is located in a supersonic stream of gas under steady-state flow conditions, the aerodynamic drag of bodies positioned in the wake of the source may be reduced substantially. The practical aspect of producing a heat spot in a supersonic stream by stabilizing an optical discharge, was considered in Ref. 2. It was shown that the most promising method of achieving a stable supply of laser energy to a supersonic stream, involves using discontinuous radiation, comprising short, high-power pulses at a high repetition frequency. It was observed experimentally[3] that the reduction in the drag of bodies depends strongly on the pulse repetition frequency, at constant average input power. In the present paper, we report some results of theoretical modeling of the influence of a pulsed source of heat release on the supersonic flow around bodies.

2. FORMULATION OF THE PROBLEM

We consider the steady-state, axisymmetric flow of a uniform supersonic stream of ideal gas around a hemisphere $x^2+r^2=R^2$, $x\leqslant 0$. Here and subsequently, we adopt the notation: x and r are cylindrical coordinates, R is the radius of the sphere, $\{u_\infty,0\}$ is the velocity of the unperturbed stream, p_∞, ρ_∞, and γ are the pressure, density, and adiabatic exponent, and $M_\infty=u_\infty\rho_\infty^{1/2}(\gamma p_\infty)^{-1/2}$ is the Mach number, where $M_\infty>1$. We assume that at zero time $t=0$, a pulsed source of energy supply with the mass heat-release density $q(x,r,t)$ begins to act in the incoming stream ahead of the sphere. Everywhere in the region of motion, we use the model of an ideal gas with constant sources of external heat influx[4] and we write the system of time-dependent axisymmetric Euler equations in the form of the conservation laws:

$$Q_t+E_x+E_r+H=0, \tag{1}$$

where the vector of the dependent variables Q, the flux vectors E and F, and the source term H are expressed as follows:

$$Q=\begin{bmatrix} e \\ \rho \\ \rho u \\ \rho v \end{bmatrix}, \quad E=\begin{bmatrix} (e+p)u \\ \rho u \\ \rho u^2+p \\ \rho v u \end{bmatrix}, \quad F=\begin{bmatrix} (e+p)v \\ \rho v \\ \rho u v \\ \rho v^2+p \end{bmatrix},$$

$$H=\begin{bmatrix} (e+p)v/r-\rho q \\ \rho v/r \\ \rho u v/r \\ \rho v^2/r \end{bmatrix}.$$

Here, $e=p/(\gamma-1)+\rho[(u^2+v^2)/2]$ is the specific energy per unit volume, ρ is the density, u and v are the velocity components along the x and r axes, respectively. The energy supply q will be defined as:[5]

$$q=W(x,r)\sum_{n=1}^{\infty}\frac{1}{f}\,\delta\left(t-\frac{n}{f}\right),$$

where δ is the Dirac delta function, f is the pulse repetition frequency, and W is the average mass density of the energy supply, which we write in the form:[1]

$$W=W_0\left(\frac{p_\infty}{\rho_\infty}\right)^{3/2}\frac{1}{R}\exp\left(-\frac{r^2+(x-x_0)^2}{L^2}\right).$$

The presence of a pulsed source term in Eq. (1) may give rise to discontinuities of the parameters at times $t=t_n=nf^{-1}$, and thus we need to use particular analytic solutions in the neighborhoods of singularity points when constructing a numerical algorithm for the solution of system (1). Integrating the vector equation (1) over t on the intervals $t\in[t_n-\varepsilon,t_n+\varepsilon]$ and going to the limit as $\varepsilon\to 0$, we easily obtain the following simple rule for passage through the singularity points $t=t_n$ (the splicing conditions of the solution): the density and velocity components remain continuous with respect to t but the pressure undergoes a jump

$$p(t_n+0)=p(t_n-0)+(\gamma-1)\rho(t_n)\frac{1}{f}W(x,r). \tag{2}$$

3. METHOD OF SOLUTION

The calculations were performed using an explicit TVD method in the Chakravarthy finite-volume formulation,[6] which can provide good resolution near strong discontinuities (shock waves and contact surfaces). We used a transformed coordinate system $x=x(\xi,\eta)$, $r=r(\xi,\eta)$ which provides a large cluster of mesh points near the body and in regions of high flow gradients (there were 84 mesh points along ξ and 56 along η). In terms of the variables ξ and η, the system (1) may also be written in the conservative form: $\overline{Q}_t+\overline{E}_\xi+F_\eta+H=0$, where $\overline{Q}=Q/J$, $\overline{E}=(x_\xi E+x_\eta F)/J$, $F=(x_\xi E+r_\eta F)/J$ and J is the Jacobian

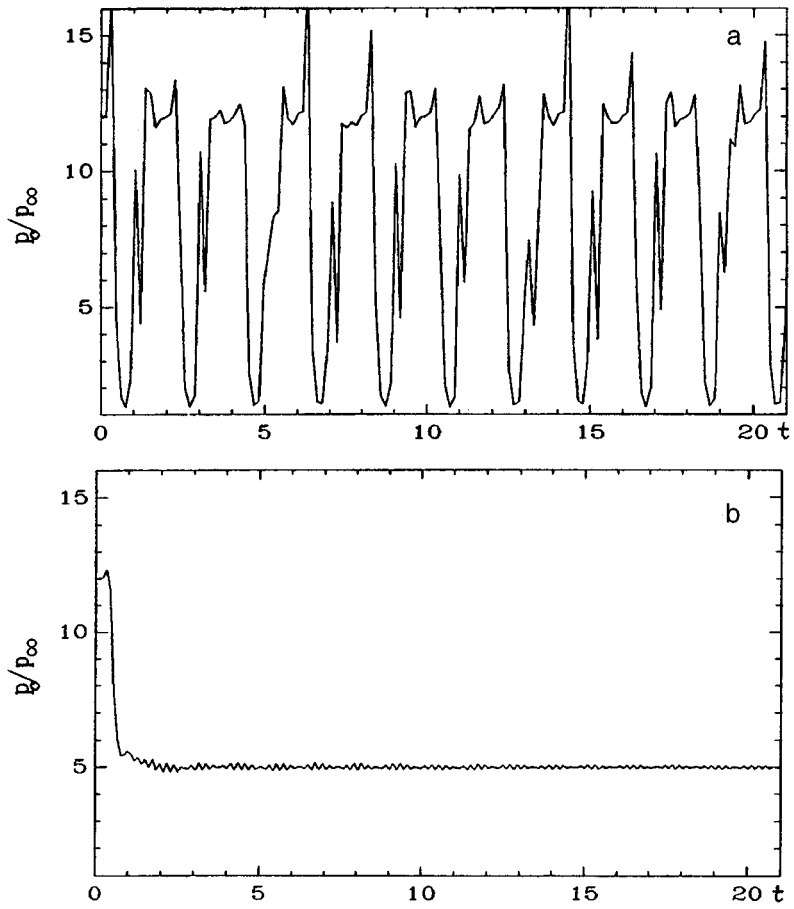

FIG. 1. Pressure p_0/p_∞ at the stagnation point as a function of dimensionless time at pulse repetition frequencies: a — $f=0.5$ and b — $f=5$.

of the transformation $\partial(x,r)/\partial(\xi,\eta)$. Relating the indices j and k to the directions ξ and η, we obtain the numerical approximation

$$(\hat{Q}_{j,k})+(\hat{E}_{j+1/2k}+\hat{E}_{j-1/2,k})+(\hat{F}_{j,k+1/2}+\hat{F}_{j,k-1/2})+\hat{H}_{j,k}=0,$$

where $\hat{E}$ and $\hat{F}$ is the numerical approximation of the fluxes across the faces the particular cell, and $\hat{Q}$ is a term comprising an approximation of the vector of the dependent variables Q, taken over the value at the center of the cell and averaged over the entire volume. The half-integer indices denote the faces of the cell and the integer values denote the cell itself or its center. Omitting the details of the numerical approximation of the flux vectors $\overline{E}$ and $\overline{F}$, note that we used a modified version of the method[7] corresponding to a third-order difference scheme for smooth solutions, which ensures that there are no parasitic oscillations near surfaces of discontinuity, where the order of the approximation is reduced.

The numerical solution procedure included determining the steady-state flow of a uniform supersonic stream around the frontal section of a sphere using the method of iteration. The distribution of the parameters thus obtained was then taken as the initial conditions for $t=0$. The numerical solution was then constructed within the time layers $t_{n-1}<t<t_n$ $1\leqslant n\leqslant N$, and the transition from one layer to another was made by means of the splicing conditions (2) specified above. Throughout the entire time, the parameters of the unperturbed stream were maintained at the entrance boundary of the calculation region, soft conditions were imposed at the exit boundary, and the condition of impenetrability was imposed at the surface of the body. The maximum number of pulses $N\gg 1$ was selected to ensure stabilization of the average flow characteristics on the intervals $t\in[t_*-T,t_8]$, $t_*\leqslant t_N$, and $T=10f^{-1}$.

4. RESULTS

Results are presented for the case $M_\infty=3$ and $\gamma=\frac{7}{5}$,

$$q=\gamma^{-3/2}W_0\ \exp\left(-\frac{r^2+(x-x_0)^2}{L^2}\right)\sum_{n=1}^{N}\frac{t_n}{n}\,\delta(t-t_n),$$

$x_0=-3.5$, $L=0.5$, $W_0=20$, $N=10^2f^{-1}$, and $t_n=nf^{-1}$ for various frequencies in the range $10^{-1}<f<10^1$.

All the quantities are cast in dimensionless form. The principal scales of length, density, and velocity are taken as R, ρ_∞, and $c_\infty=(\gamma p_\infty/\rho_\infty)^{1/2}$. The pressure is normalized to $\rho_\infty c_\infty^2$, the external energy supply density to $c_\infty^3\,R^{-1}$, and the time to $c_\infty^{-1}R$.

At pulse repetition frequencies less than $f=f_1\approx 0.5$, the thermal wake behind the source exhibits a well-defined, discrete structure of diverging waves. For $f>f_2\approx 5.0$, the wake is almost continuous. Figure 1 shows the pressure $p_0(t)=p(-1,0,t-f^{-1})$ at the critical point on a sphere, which includes a transition section from the initial steady-state flow to a quasiperiodic state in the presence of a heat source, pulsed with the frequency $f=f_1$ or $f=f_2$.

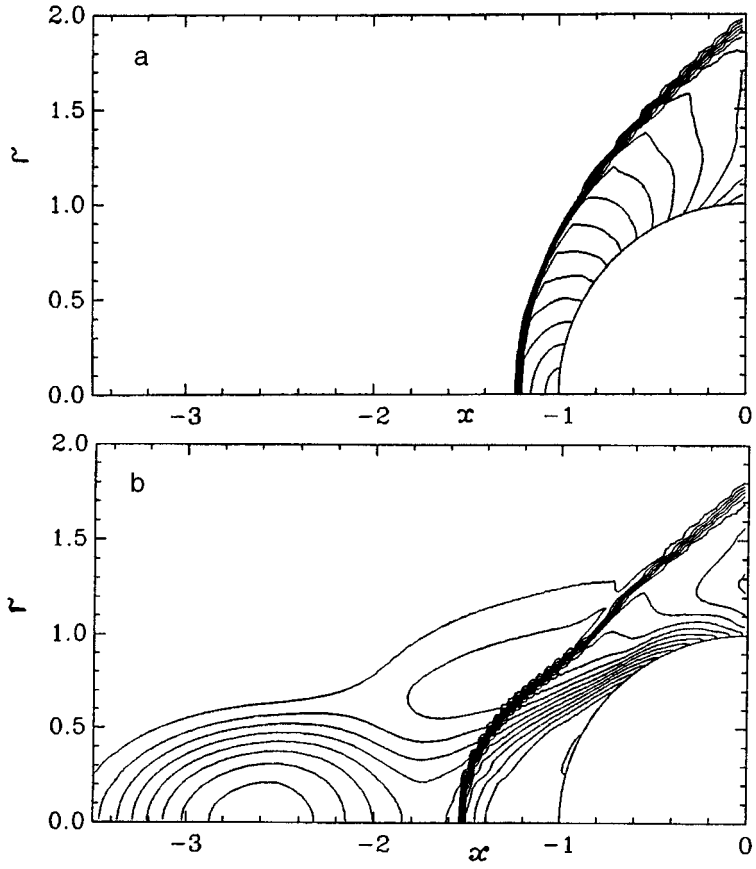

FIG. 2. Mach number contours for flow of a supersonic gas stream around a sphere: a — no energy supplied and b — at a pulse repetition frequency $f=2$ ($t=11.2$).

Figure 2 shows the rearrangement of the flow around a sphere under the influence of a pulsed heat source. The bow shock shows considerably increased separation, and recirculation zones are formed in the shock layer, in good agreement with the results of Ref. 1, which were obtained for steady-state heat release conditions.

The following formulas were used to determine the averages

$$G(f)=\int_{v_*}\left(\frac{1}{T}\int_{t_*-T}^{t_*}\rho q\,dt\right)dV, \quad C(f)=\frac{1}{T}\int_{t_*-T}^{t_*}C_x\,dt,$$

where G is the average power supplied in the time $T=10/f$ in the heat spot V_*: $r^2+(x-x_0)^2\leqslant L^2$, and C_x is the instantaneous drag coefficient of the hemisphere:

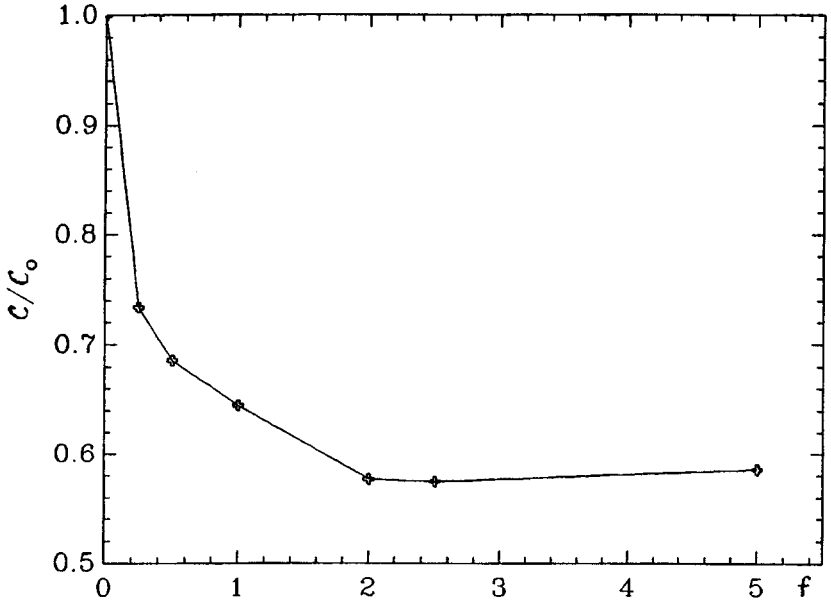

FIG. 3. Drag coefficient C/C_0 versus pulse repetition frequency f for $W_0=20$.

$$C_x(t)=\frac{4}{\gamma M_\infty^2}\int_0^1(\gamma p_c-1)r\,dr,\quad p_c=p(-\sqrt{1-r^2},r,t).$$

Figure 3 shows the influence of the heat source frequency f on the average drag coefficient of the hemisphere for W_0 = const as compared with flow conditions without any energy supply, $C_0=C_x(0)$. An appreciable reduction in the loading is observed even for $f=1$ (up to 65% of the flow regime with no energy supply). A saturation effect is observed whereby the drag shows very little decrease above a certain pulse repetition frequency: a minimum $C(f_*)\approx 0.58C_0$ is reached at $f=f_*\approx 2$ and is then followed by a slow increase in $C(f)$ for $f>f_*$. It may therefore be concluded that a pulsed heat supply is more effective than a steady-state supply.

These results agree qualitatively with the experimental data.[3]

[1] P. Yu. Georgievskiĭ and V. A. Levin, Pis'ma Zh. Tekh. Fiz. **14**, 684 (1988) [Sov. Tech. Phys. Lett. **14**, 303 (1988)].
[2] P. K. Tret'yakov, G. P. Grachev, A. I. Ivanchenko *et al.*, Dokl. Akad. Nauk **336**, 466 (1994).
[3] P. K. Tret'yakov, A. F. Garanin, G. N. Grachev *et al.*, Dokl. Akad. Nauk **351**, No. 3, (1996).
[4] G. G. Chernyĭ, *Gasdynamics* [in Russian], Nauka, Moscow (1988).
[5] S. V. Guvernyuk and K. G. Savinov, Izv. Ross. Akad. Nauk Ser. Mekh. Zhidk. Gaz. No. 2, 164 (1996).
[6] S. R. Chakravarthy and S. Osher, ''A new class of high-accuracy TVD schemes for hyperbolic conservation laws,'' AIAA Paper 85–0363 (1988).
[7] S. R. Chakravarthy, ''The versatility and reliability of Euler solvers based on high-accuracy TVD formulations,'' AIAA Paper 86–0243 (1986).

Translated by R. M. Durham

A possible method to measure accurately the refractive index of a transparent liquid

Kh. V. Nerkararyan, N. L. Markaryan, and E. Dzh. Ogannisyan

Erevan State University
(Submitted December 15, 1996)
Pis'ma Zh. Tekh. Fiz. **23**, 9–13 (May 12, 1997)

An analysis is made of some characteristics of the propagation of a light wave through a semiconductor-gap-semiconductor structure, where the thickness of the gap between the parallel planes of the crystals is of the order of a micron. It is shown that a combination of multiple reflection and interference processes produces an exponential dependence of the transmitted radiation intensity on the refractive index of the material filling the gap. This circumstance can be used to set up a simple method for accurate determination of the refractive index of a transparent liquid. © *1997 American Institute of Physics.*
[S1063-7850(97)00205-X]

Methods of measuring the refractive indices of various media can be classified into several groups according to the phenomena used. Information on the refractive index may be obtained by determining the angle of refraction of a light beam, the intensity and polarization of reflected radiation, or the path difference between interfering beams.[1–4]

In the present paper we propose a new method of measuring the refractive index of a transparent liquid, which involves determining the intensity of radiation emerging from a quasiwaveguide structure. Here, a combination of multiple reflection and interference processes produces an exponential dependence of the output intensity on the refractive index and thereby creates favorable conditions for accurate measurement of the refractive index.

Crystals exhibiting cleavage properties may be used to fabricate a structure consisting of two crystals separated by a distance of less than or of the order of a micron. In this case, the parallel facing surfaces of the crystals are cleavage planes. The electronic properties of this type of crystal–gap–crystal structure were identified and investigated in Refs. 5–7 for the case of a plane capacitor with semiconductor plates. In Ref. 8, we discussed the feasibility of using this structure to fabricate a planar optical waveguide with movable boundaries, capable of efficiently modulating the phase of the wave. Waveguide propagation of the radiation through the crystal-gap-crystal structure is obtained when the refractive index of the liquid filling the gap is higher than that of the crystal. The other limiting case, when the refractive index of the crystal is considerably higher than that of the liquid filling the gap, is also of decided interest. In this case, a quasiwaveguide propagation regime is established where the intensity losses of radiation propagating through the structure are low over distances of the order of the wavelength. This situation is analyzed theoretically and experimentally in the present study.

We consider some characteristics of the propagation of transverse electric (TE) modes through a structure under conditions where the refractive index of the crystals (n_1) is higher than that (n_2) of the material filling the gap. The y-component of the electric field of a wave with the frequency ω may be expressed in the following form:

$$E_y = E_0^{(a)}[\exp\, i(\gamma_1 + i\gamma_2)x + \exp(-i(\gamma_1 + i\gamma_2)x)] \times \exp\, i[(\beta + i\beta_2)z - \omega t], \quad |x| \leqslant d/2; \tag{1}$$

$$E_y = E_0^{(b)}[\exp\, i(\chi_1 + i\chi_2)(|x| - d/2)] \times \exp\, i[(\beta_1 + i\beta_2)z - \omega t], \quad |x| \geqslant d/2. \tag{2}$$

It then follows from the wave equation that

$$n_2^2(2\pi/\lambda_0)^2 = \gamma_1^2 - \gamma_2^2 + \beta_1^2 - \beta_2^2, \quad \gamma_1\gamma_2 + \beta_1\beta_2 = 0, \tag{3}$$

$$n_1^2(2\pi/\lambda_0)^2 = \chi_1^2 - \chi_2^2 + \beta_1^2 - \beta_2^2, \quad \chi_1\chi_2 + \beta_1\beta_2 = 0. \tag{4}$$

Here, d is the thickness of the gap, c is the velocity of light, and λ_0 is the wavelength in vacuum. Joining the fields at the interfaces by a standard procedure, in the limiting case $n_1 \gg n_2$ and $\lambda_0/d \ll 2n_1$, we obtain the wave parameters:

$$\gamma_1 \approx \frac{\pi}{d}, \quad \gamma_2 \approx -\frac{\lambda_0}{n_1 d^2}, \quad \chi_1 = \frac{2\pi n_1}{\lambda_0}, \quad \chi_2 = -\frac{\lambda_0^2}{2n_1^2 d^3}, \tag{5}$$

$$\beta_1 \approx \frac{2\pi}{\lambda_0} n_2, \quad \beta_2 \approx \frac{\lambda_0^2}{2n_1 n_2 d^3}. \tag{6}$$

We neglect the imaginary part of the crystal refractive index, assuming that the absorption coefficient is considerably less than the wave vector. Quasiwaveguide propagation of the TE mode takes place because in this particular case, the attenuation constant β_2 is considerably smaller than all the wave-vector components (γ_1, χ_1, and β_1). A simple analysis shows that transverse magnetic modes cannot propagate through the structure in the quasiwaveguide regime because TM modes are rapidly attenuated.

We now discuss the feasibility of applying these formulas for the case where the crystal–gap–crystal structure is formed by a GaAs crystal, and helium–neon laser radiation propagates through the gap. In this case, the wave vector χ_1 ($\chi_1 \ll \beta_1$, χ_2, β_2) is an order of magnitude greater than the absorption coefficient and our formulas can be applied with a fairly high degree of accuracy to the gap and its immediate vicinity. Absorption begins to play an important role when the radiation propagating through the crystal is some

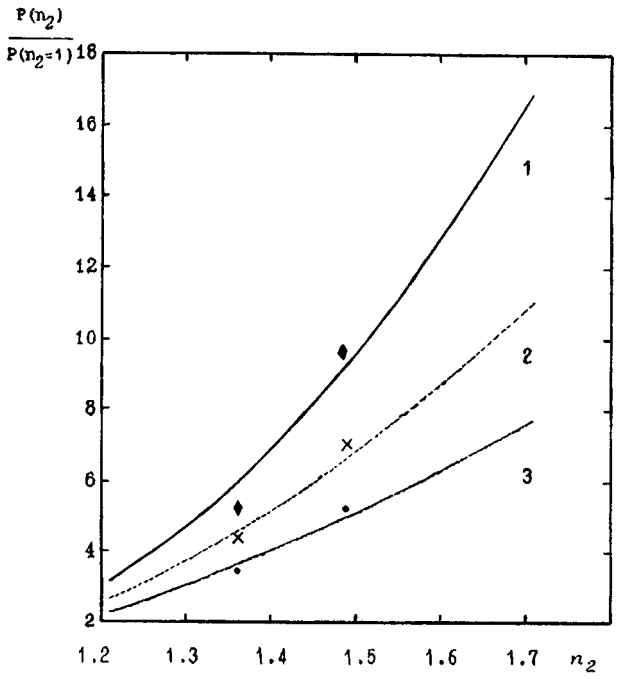

FIG. 1. Results of experimental investigations for three different structures indicated by the symbols. Curves *1*, *2*, and *3*, obtained using formula (7), correspond to the cases $\alpha=6.87$, $\alpha=5.84$, and $\alpha=4.86$, respectively.

distance from the gap. Thus, only the radiation component concentrated within the gap leaves the structure. As a result, the output radiation power may be given by the following formula:

$$P(n_2)=SP_0\ \exp\left(-\frac{\alpha}{n_2}\right),\quad \alpha=2\beta_2/ln_2=\frac{\lambda_0^2 l}{n_1 d^3}. \qquad (7)$$

Here, P_0 is the radiation power incident on the structure, l is the length of the structure, and the parameter S is less than unity and indicates the radiation insertion losses.

It follows from formula (7) that, as the refractive index of the material filling the gap increases, the losses decrease and the output radiation power increases. This is because in this case, the x-component of the wave vector (γ_1) remains constant but, as a result of the higher refractive index, its z-component (β_1) increases, causing an increase in the angle of incidence. In consequence, the coefficient of reflection from the interfaces also increases and the wave power is more effectively concentrated in the gap.

Simple estimates reveal that the radiation leaving the structure can easily be recorded even for fairly high values of the parameter α ($\alpha/n_2\approx 10$) and relatively low input powers ($P_0\approx 1$ mW). Under these conditions, a small change in the refractive index of the material filling the gap may substantially change the output radiation power. This factor may play an important role in measurements of the refractive index. Measurements were made of the output power from a crystal-gap-crystal structure, fabricated using a GaAs crystal with $l=0.35$ mm, on which focused helium–neon laser radiation was incident. Three structures with gaps of different thickness (with different α) were investigated. The output power was measured for the case of a vacuum gap ($n_2=1$) and also when the gap was filled with alcohol ($n_2=1.36$) and toluene ($n_2=1.5$). Figure 1 shows the experimental values of $P(n_2)/P(n_2=1)$ and the corresponding theoretical curves. It is important to note that compared with the vacuum gap, the output radiation power increases sharply when the gap is filled with liquid. The satisfactory agreement between the experimental and theoretical results suggests that this process may serve as the basis for a new, fairly simple method of measuring the refractive index of a transparent liquid.

[1] A. A. Shishlovskiĭ, *Applied Physical Optics* [in Russian], Moscow (1961).
[2] B. V. Ioffe, *Refractometric Methods in Chemistry* [in Russian], Leningrad (1983).
[3] T. Ding and E. Garmire, Appl. Opt. **22**, 3177 (1983).
[4] R. Th. Kersten, Opt. Commun. **13**, 327 (1977).
[5] V. M. Arutyunyan and Kh. V. Nerkararyan, Pis'ma Zh. Tekh. Fiz. **19**(21), 44 (1993) [Tech. Phys. Lett. **19**, 684 (1993)].
[6] V. M. Arutyunyan and Kh. V. Nerkararyan, Fiz. Tverd. Tela. (St. Petersburg) **36**, 1513 (1994) [Phys. Solid State **36**, 827 (1994)].
[7] Vl. M. Aroutionian and Kh. V. Nerkararian, Sensors Actuators **24–25**, 353 (1995).
[8] Vl. M. Arutyunyan and Kh. V. Nerkararyan, Pis'ma Zh. Tekh. Fiz. **21**(16), 52 [Tech. Phys. Lett. **21**, 656 (1995)].

Translated by R. M. Durham

Application of a nuclear quadrupole resonance method to measure stress in a matrix-tracer system in composites

N. E. Aĭnbinder, A. S. Azheganov, V. P. Begishev, and N. K. Shestakova

Perm State University
(Submitted December 16, 1996)
Pis'ma Zh. Tekh. Fiz. **23**, 14–18 (April 12, 1997)

A quantitative correlation has been established between the shift of the nuclear quadrupole resonance frequency of the tracer and the stress in a matrix-tracer system in composites. Measurements are made of the ^{63}Cu resonance frequencies in samples of epoxy resin containing cuprous oxide powder. The stresses in the resin and their dependences on temperature and external pressure are determined. © *1997 American Institute of Physics.*
[S1063-7850(97)00305-4]

Test samples containing powder of a crystalline substance as a tracer may be used to study the mechanical interaction between composite binders and fillers having different thermal and elastic properties. The tracer crystals should contain quadrupole nuclei at which nuclear quadrupole resonance signals may be observed. In experiments carried out with epoxy resins, shifts of the tracer resonance frequency have been observed and measured during hardening of the resin[1] and during compression, tension, and heating of the samples.[2,3] In the present paper, we show that there is a correlation between the shift of the nuclear quadrupole resonance frequency of the powder tracer and the magnitude of the stresses in the polymer matrix.

For our investigations we used ÉD-10 epoxy resin, hardened with polyethylene polyamine and containing cuprous oxide (Cu_2O) tracer powder, having a concentration C_l between 0.016 and 0.34 parts by volume. Cuprous oxide was chosen because these crystals have a cubic structure and behave as isotropic bodies under thermal expansion and uniform hydrostatic compression. The resonance frequency of ^{63}Cu in Cu_2O at 293 K is 26 012 kHz and decreases monotonically with increasing temperature. The pressure dependence of the frequency $\nu(p)$ is linear in the pressure range up to hundreds of megapascals. The samples were tested under the isotropic action of hydrostatic compression and uniform heating (cooling). The experimental method and apparatus were described in detail in Ref. 3.

To investigate the temperature dependence of the nuclear quadrupole resonance frequency shift of the tracer, samples of tracer-containing polymer and a control sample (pure cuprous oxide powder) were heated in an oil bath. The bath was heated to 423 K and then slowly cooled. Measurements were made of the frequency difference $\Delta\nu_i=\nu_i-\nu_0$ for Cu_2O in the polymer, ν_i, and control samples, ν_0, in the temperature range 393–293 K at 10 K intervals. An example of the $\Delta\nu_i(T)$ curves obtained is shown in Fig. 1. In the range of 293–373 K, which corresponds to the vitrified state of the resin, $\Delta\nu_i(T)$ increases linearly with decreasing temperature.

The samples were subjected to hydrostatic compression in a high-pressure chamber filled with oil and thermostatically controlled at $T_0=293$ K. The frequencies ν_i of the ^{63}Cu nuclei in the tracer were measured at external pressures p_e between 0 and 49.03 MPa. A linear dependence of ν_i on the pressure applied to the sample was observed. A shift of the resonance frequency $\nu_i(p_e,T_0)$ of the cuprous oxide crystals was detected in the sample compressed to a pressure p_e, relative to the frequency $\nu_0(p=0,T_0)$ of the free crystals at the same temperature:

$$\Delta\nu_i(p_e)=\nu_i(p_e,T_0)-\nu_0(p=0,T_0). \tag{1}$$

The values of $\Delta\nu_i(p_e)$ for a sample with $C_i=0.34$ are plotted in Fig. 1.

A clear dependence of the frequency shifts on the tracer concentration C_i was observed experimentally. The slope of the curves $\Delta\nu_i(p_e)$ and $\Delta\nu_i(T)$ decreases monotonically with increasing concentration.

The frequency shift $\Delta\nu_i$ is caused by the pressure p_i of the polymer on the surface of the tracer particles. Since the signal is observed experimentally from the entire volume of the sample and the average signal frequency shift is recorded, we find the pressure p_i averaged over all the tracer crystals:

$$p_i=\Delta\nu_i(p_e,T)/(\partial\nu/\partial p)_T, \tag{2}$$

where $(\partial\nu/\partial p)_T=0.369\pm0.002$ kHz/MPa is the pressure coefficient of the ^{63}Cu nuclear quadrupole resonance frequency in Cu_2O (Ref. 3), determined under hydrostatic compression of the crystal. In Fig. 1, a pressure axis, calculated according to Eq. (2), is juxtaposed with the frequency axis.

We now calculate the stresses in the polymer matrix. As a mechanical model of a tracer-containing polymer, we assume a homogeneous, isotropic, linearly elastic medium with isotropic, linearly elastic, spherical inclusions distributed uniformly in its bulk. Similar models were analyzed in Refs. 4 and 5. We assume that this medium undergoes hydrostatic compression at the pressure p_e without any temperature gradient in the medium. Since the model and the external influences are isotropic, the tracer particles should undergo uniform hydrostatic compression at the pressure p_i, which is numerically equal to the component of the stress tensor in the polymer matrix, normal to the surface.

We take the polymer state at the glass-transition temperature T_g as the initial unstressed state. In spherical coordinates with origin at the center of a spherical tracer particle,

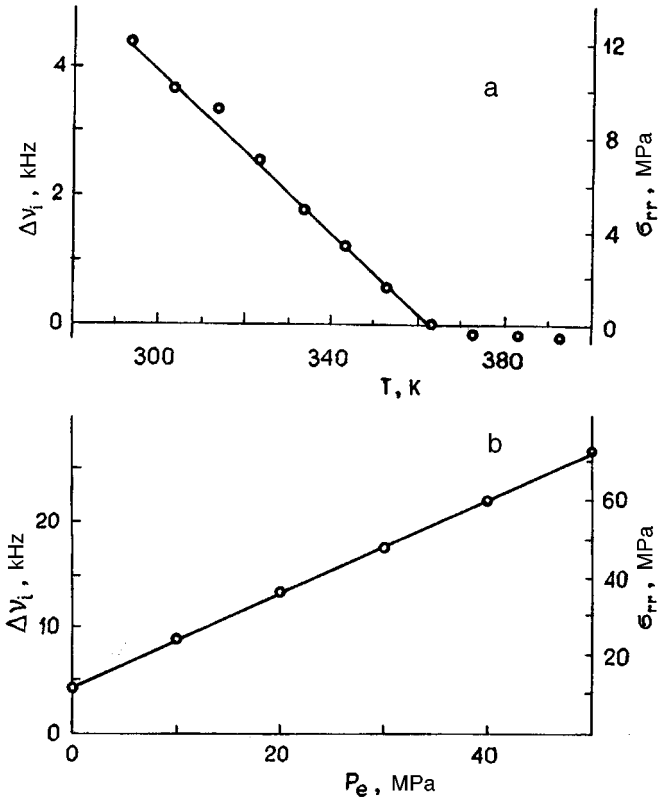

FIG. 1. Nuclear quadrupole resonance frequency shift $\Delta\nu_i$ and internal stress σ versus temperature T (a) and external pressure p_e (b) for a sample with a tracer concentration $C_i=34$ wt.%. The solid curve gives the calculations.

the radial and tangential components of the stress tensor in the polymer matrix at the surface of a tracer particle are:

$$\sigma_{rr(i)}=-\frac{(1-C_i)(\alpha_i-\alpha)(T-T_g)+(\chi+3/4\mu)\sigma_{rr(e)}}{\chi_i+C_i(\chi-\chi_i)+3/4\mu}, \tag{3}$$

$$\sigma_{\theta\theta(i)}=\sigma_{\varphi\varphi(i)}=-[(1+2C_i)\sigma_{rr(i)}-3\sigma_{rr(e)}]/2(1-C_i), \tag{4}$$

where $\alpha=(1/V)(\partial V/\partial T)_p$ is the bulk coefficient of thermal expansion, $\chi=-(1/V)(\partial V/\partial p)_T$ is the bulk modulus, μ is the shear modulus of the polymer material, α_i and χ_i are the corresponding coefficients of the tracer material, and $\sigma_{rr(e)}=-p_e$ is the stress at the external surface of the sample.

Curves of $\sigma_{rr}(T)$ and $\sigma_{rr}(p_e)$, calculated according to formula (3), for $\alpha=1.8\times10^{-4}$ K^{-1}, $\chi=0.224$ GPa^{-1}, and $\mu=1.27$ GPa (Ref. 7), $\alpha_i=0.06\times10^{-4}$ K^{-1} and $\chi_i=0.0198$ GPa^{-1} (Ref. 8) are given by the solid curves in Fig. 1 for $T_g=363$ K and a tracer concentration $C_i=0.34$.

It was found that the values of the pressure p_i obtained from the frequency shifts agreed numerically with the values of the radial component of the stress in the polymer matrix, calculated using the mechanical model of a tracer-containing polymer. Similar agreement between the numerical values of p_i and σ_{rr} was also obtained for other samples with a lower tracer concentration.

To sum up, we draw the following conclusions:

1) Nuclear quadrupole resonance can be used for experimental measurements of the stresses induced in the matrix-tracer system in composites;

2) This relatively simple isotropic model is suitable for predicting the magnitude of the stresses induced by incorporating powder tracers in a polymer.

[1] H. S. Gutowsky, R. A. Bernheim, and H. Tarkow, J. Polymer Sci. **44**, 143 (1960).
[2] R. R. Hewitt and B. Mazelsky, J. Appl. Phys. **43**, 3386 (1972).
[3] N. E. Ainbinder, A. S. Azheganov, A. V. Danilov, and N. K. Shestakova, J. Mol. Struct. **345**, 105 (1995).
[4] N. E. Aĭnbinder, *Radiospectroscopy* [in Russian], Perm University, Perm (1989).
[5] R. Christensen, *Introduction to the Mechanics of Composites* [Russ. transl., Mir, Moscow, 1982].
[6] *Handbook of Composites*, edited by G. Lubin, Book. 1 (Van Nostrand Reinhold, New York, 1982) [Russ. transl., Mashinostroenie, Moscow, 1988].
[7] *Handbook of Physical Quantities*, edited by I. S. Grigor'ev and E. Z. Meĭlikhov [in Russian], Energoatomizdat, Moscow (1991).

Translated by R. M. Durham

Flexoelectric response of a liquid crystal layer with a temperature-induced orientational transition

M. V. Khazimullin, A. P. Krekhov, Yu. A. Lebedev, and O. A. Scaldin

Institute of Physics of Molecules and Crystals, Ufa Scientific Center, Russian Academy of Sciences
(Submitted October 28, 1996)
Pis'ma Zh. Tekh. Fiz. **23**, 19–23 (May 12, 1997)

It has been confirmed that the flexoelectric polarization model can provide an adequate interpretation of the temperature behavior of the electrical response of homeotropically oriented samples of *n*-methoxybenzylidene-*n*-butylaniline nematic liquid crystals at twice the excitation frequency. The temperature dependence of samples with different director orientations has been investigated experimentally. © *1997 American Institute of Physics.* [S1063-7850(97)00405-9]

It is known that the periodic deformation of a thin layer of nematic liquid crystal gives rise to an electrical signal induced by the formation of a macroscopic polarization, which may be related to the existence of a surface layer of molecules with uncompensated dipole moments (surface polarization), distortion of the director field (flexoelectric polarization), and so forth.[1] It was demonstrated in Ref. 1 that for homeotropically oriented samples of *n*-methoxybenzylidene-*n*-butylaniline (MBBA), a flexoelectric polarization model can provide an adequate interpretation of experimental data on the temperature behavior of the electrical response at twice the excitation frequency $U_{2f}(T)$. However, samples with different director orientations must be investigated to provide definite confirmation that the flexoelectric effect makes the dominant contribution to U_{2f}. A method of depositing silicon monoxide on substrates confining a nematic liquid-crystal layer is frequently used to fabricate such layers. The temperature dependence of the angle of tilt of the director on these substrates may be described using an orientational transition model proposed earlier.[2] In the present paper, we investigate the temperature dependence of the electrical response on substrates with an orientational transition, and we show that the behavior of $U_{2f}(T)$ for obliquely oriented layers is also consistent with the flexoelectric polarization model.

Layers of MBBA of thickness $d=40$ μm, with different initial director orientations(at room temperature), were studied experimentally. The substrates were of glass with a conducting coating, on which silicon monoxide was deposited in vacuum at an oblique angle, the director orientation depending on the angle of deposition. The crystal layer was deformed by periodic oscillations of the lower, thinner, substrate (thickness $h\sim 100-200$ μm) at frequency $f=1$ kHz and small amplitude ($a\sim 0.1$ μm), so that the director oscillations were damped near the upper substrate. The electrical response of the cell was recorded by a tuned voltmeter at twice the excitation frequency. Details of the experimental technique are described in Ref. 3.

Experimental temperature dependences of the second harmonic $U_{2f}(T)$ for cells with different initial tilt angles of the director are plotted in Fig. 1. At low temperatures, the absolute value of U_{2f} increases with increasing steady-state angle, but near the point of transition to an isotropic liquid (T_c), it tends to the fixed value U_{2f}^h. Observation of the optical polarization revealed that at the temperature corresponding to U_{2f}^h, all the samples became uniformly homeotropic, i.e., a temperature-induced tilt–homeotropic orientational transition occurred in all the cells.

Let us consider a thin layer of nematic liquid crystal oriented at the angle θ to the surface of the substrates. Let us assume that the lower substrate undergoes mechanical deformation at the frequency f, whereupon the director will oscillate around the angle θ induced by the substrate, following the relation $\theta_d=\theta_0\cos(2\pi ft)$, where θ_0 is the amplitude of the oscillations which, for fixed amplitude and frequency of the mechanical excitation, depends on the viscous properties of the nematic and the tilt angle θ. It can be shown that when the amplitudes of the mechanical oscillations are small ($a/d\ll 1$), the potential difference on the substrates, induced by the flexoelectric polarization,[1] will be given by

$$U_{2f}=2\pi e\,\frac{(\varepsilon_\parallel \sin^2\theta-\varepsilon_\perp\cos^2\theta)}{(\varepsilon_\parallel \sin^2\theta+\varepsilon_\perp\cos^2\theta)^2}\,\theta_0^2, \tag{1}$$

where $\varepsilon_\parallel$, $\varepsilon_\perp$ are the components of the dielectric tensor and $e=e_{11}+e_{33}$ is the sum of the flexoelectric coefficients. The temperature behavior of the substrate-induced steady-state tilt angle of the director for these cells is described by:[2]

$$\cos^2\theta=\frac{S_t(S-S_{th})}{S(S_t-S_{th})}\cos^2\theta_i, \tag{2}$$

where S is the scalar order parameter, and S_{th} and S_t are the values of S corresponding to the temperatures of the transition to homeotropy and of the measurement of the initial tilt angle (θ_i).

The mechanical oscillations of the substrate cause an axisymmetric oscillatory flow of nematic liquid crystal, and for small-amplitude director oscillations, we can use the expression:[4]

$$\theta_0=\frac{A\eta_1(\lambda\cos^2\theta-\sin^2\theta)(1+\lambda)}{(1-\lambda^2)(\eta_1\cos^2\theta+\eta_2\sin^2\theta)+(\eta_1-\eta_2)(\lambda\cos^2\theta-\sin^2\theta)^2}, \tag{3}$$

where $\eta_1=(\alpha_3+\alpha_4+\alpha_6)/2$, $\eta_2=(-\alpha_2+\alpha_4+\alpha_5)/2$, $\lambda=\alpha_3/\alpha_2$ (α_i are the Leslie viscosity coefficients). The dimensionless coefficient A, which is determined by the cell

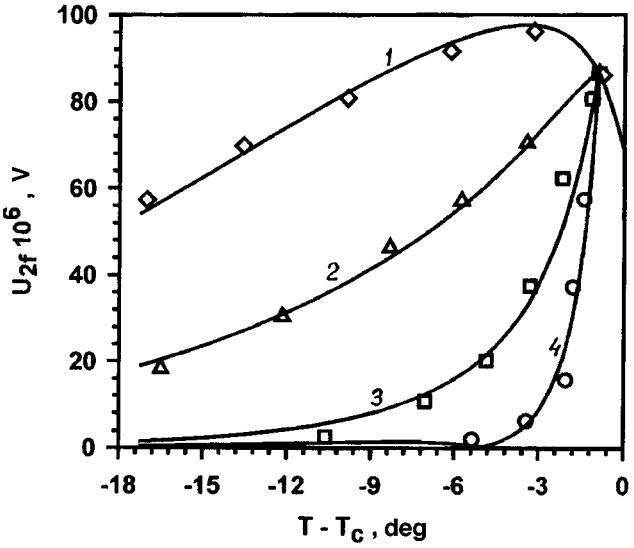

FIG. 1. Temperature behavior of the second harmonic $U_{2f}(T)$ for cells with different initial tilt angles θ_i: *1* — 81.5°, *2* —68°, *3* — 50°, and *4* — 10°.

geometry and is independent of temperature, may be found by considering oscillations of a thin circular membrane. In our case, for a membrane thickness $h=100$ μm, radius $R=5$ mm, oscillation frequency $f=1$ kHz, and the deformation amplitude at the center $a=0.1$ μm, we have $A=2.4\times10^{-2}$.

Using published data on the temperature dependences of $\varepsilon_{\parallel}$, $\varepsilon_{\perp}$, λ (Ref. 5), η_1, η_2 (Ref. 6), and S (Ref. 7), and substituting the experimental values of $U_{2f}(T)$ into Eq. (1) with allowance for Eqs. (2) and (3), we obtain the temperature dependence of the sum of the flexoelectric coefficients $e=e_{11}+e_{33}$ (Fig. 2). The value of $e\sim10^{-11}$ C/m obtained at room temperature is of the same order of magnitude as the data obtained by other researchers.[5] Using the approximation $e(T)=\alpha S(T)+\beta S^2(T)+\gamma S^3(T)$ (Fig. 2, solid curve, $\alpha=-1.1573\times10^{-11}$ C/m, $\beta=9.2530\times10^{-11}$ C/m, and $\gamma=-8.0362\times10^{-11}$ C/m) yields a theoretical dependence

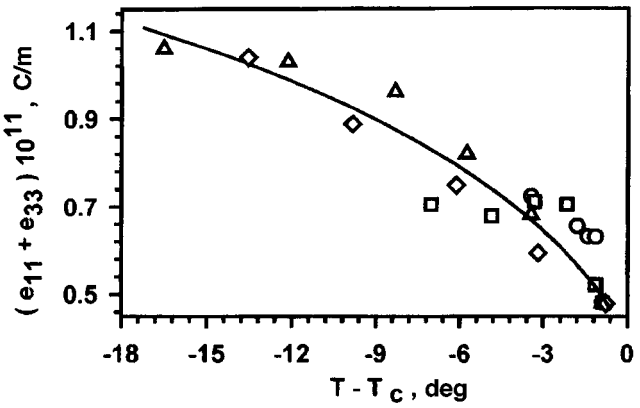

FIG. 2. Temperature dependence of the flexoelectric coefficients $e=e_{11}+e_{33}$.

of the temperature behavior of the second harmonic U_{2f} (Fig. 1, solid curve), which shows good agreement with the experimental data.

To conclude, this model of flexoelectric polarization and temperature-induced orientational transitions can be used to describe the experimentally observed temperature behavior of the second harmonic of the electrical response in MBBA on substrates with an orientational transition. The model can also be used to determine the temperature dependence of the sum of the flexoelectric coefficients $e_{11}+e_{33}$.

[1] G. Barbero, A. N. Chuvyrov, A. P. Krekhov *et al.*, J. Appl. Phys. **69**, 6343 (1991).
[2] A. P. Krekhov, M. V. Khazimullin, and Yu. A. Lebedev, Kristallografiya **40**, 137 (1995) [Crystallogr. Rep. **40**, 124 (1995)].
[3] O. A. Skaldin, A. P. Krekhov, and A. N. Chuvyrov, Kristallografiya **34**, 951 (1989) [Sov. J. Crystallogr. **34**, 572 (1989)].
[4] A. P. Krekhov and L. Kramer, Phys. Rev. E **53**, 4925 (1996).
[5] H. Kelker and R. Hatz, *Handbook of Liquid Crystals* (Verlag Chemie, Weinheim, 1980), p. 917.
[6] Ch. Gahwiller, Mol. Cryst. Liquid Cryst. **20**, 301 (1973).
[7] S. Jen, N. A. Clark, P. I. Pershan *et al.*, Phys. Rev. Lett. **31**, 1552 (1973).

Translated by R. M. Durham

Photoresonant ionization of gaseous media by excimer laser radiation

B. A. Knyazev, P. I. Mel'nikov, G. Blyum, A. A. Doroshkin, and A. N. Matveenko

Novosibirsk State University, G. I. Budker Institute of Nuclear Physics, State Scientific Center, Novosibirsk
(Submitted December 24, 1996)
Pis'ma Zh. Tekh. Fiz. **23**, 24–32 (May 12, 1997)

An identification is made of twenty five elements whose resonance lines overlap the emission lines of high-power pulsed ultraviolet gas lasers or lie in the immediate vicinity of them, so that the mechanism laser ionization based on resonance saturation (LIBORS) can be used to ionize the vapor of these elements. Resonance transitions of atoms and ions excited by the same laser (by krypton fluoride and xenon fluoride lasers, respectively) are observed for tantalum and uranium. It ishas been suggested that these elements may be used as ''catalysts'' for ''catalytic'' resonance ionization (CATRION) of dense multicomponent gas mixtures. Experiments have been carried out to study the krypton fluoride laser irradiation of expanding vapor clouds of different elemental composition, created by the evaporation of targets with a ruby laser. Photographs obtained with an image converter, measurements of the refractive index gradient from the deflection of the laser beam, as well as probe and spectroscopic measurements indicate that the clouds undergo photoresonant ionization if they contain tantalum vapor but that the laser radiation has no influence otherwise. [S1063-7850(97)00505-3]

The ionization of dense metal vapor in a high-intensity resonant laser radiation field was observed in Ref. 1. The mechanism for this multistage process was explained in Refs. 2 and 3. The process begins with the heating of seed electrons by superelastic collisions with atoms excited to saturation of the resonance level and/or by resonant stimulated bremsstrahlung absorption of photons. The electron-atom collisions result in filling of the upper excited levels. The process concludes with the rapid impact ionization of the gas by the heated electrons. The laser pulse length, the radiation power density, and the gas density must obviously be sufficient to transfer the process to the ''explosive'' phase. This type of photoresonant ionization, which has been termed Laser Ionization Based on Resonance Saturation (LIBORS), has recently been widely used to excite steady-state vapor of group-I and group-II metals with narrow-band radiation from tunable dye lasers. More recently, LIBORS has been used to create a lithium plasma at the anode of the PBFA-II high-power pulsed ion accelerator.[4]

The advantage of photoresonant ionization is that it is entirely noncontact, and the ion temperature is substantially lower than that observed when plasmas are generated by other methods. However, the scope for the practical implementation of the classical LIBORS technique is rather limited because the operating life and reliability of flashlamp-pumped dye lasers are poor, and the resonance transitions of very many elements lie in the ultraviolet (or even in the vacuum ultraviolet), where no high-power sources of tunable radiation are available. Fortunately, more than twenty elements have resonance transitions which lie close to, or coincide with, the emission bands of high-power pulsed gas lasers. For instance, such matches have already been established for Al (Ref. 5) and Fe (Ref. 6). The position of these transitions relative to the emission spectra of nitrogen and excimer lasers is shown in Fig. 1, and their atomic characteristics are summarized in a table given in Ref. 7. It can be seen that these elements include some very commonly used ones and also some of particular interest for many applications (such as uranium and arsenic). Since the emission wavelengths of these lasers lie in the ultraviolet, this variant of the photoresonant ionization technique may be called ultraviolet LIBORS.

An important advantage of ultraviolet LIBORS is that the resonance excited atoms undergo direct one-photon ionization by the exciting laser radiation (in the visible, this is only possible for a few elements). This mechanism is not as effective as LIBORS itself, but may significantly reduce the requirements for the initial number of seed electrons in the gas and may speed up the ionization process. A second factor is the large spectral width of excimer laser radiation, close to 1 nm, which is difficult to narrow and tune (within the fluorescence band shown in Fig. 1) without substantial energy losses that are unacceptable for practical applications. However, there is probably no need for narrowing of the spectrum because the width of a resonance atomic transition in the case described may be of the order of 1 nm as a result of pressure broadening[8] or dynamic field broadening.[9] Substantial resonance broadening was observed, for instance, in Refs. 4 and 5. This means that atoms whose transitions lie in the immediate vicinity of the lasing spectrum may also undergo photoresonant ionization. These factors make it significantly easier to achieve ultraviolet LIBORS with excimer lasers and ensure a highly efficient process.

In view of the appreciable difficulties involved in making calculations, and the lack of much data for complex atomic systems, experimental investigations are a better method of determining the optimum gas and radiation parameters to maximize the ionization efficiency. Assuming that the atomic transitions are saturated, we can initially say that the optimum spectral power density F_{opt} of the laser radiation should be roughly the same order of magnitude as the saturation intensity of the transition,

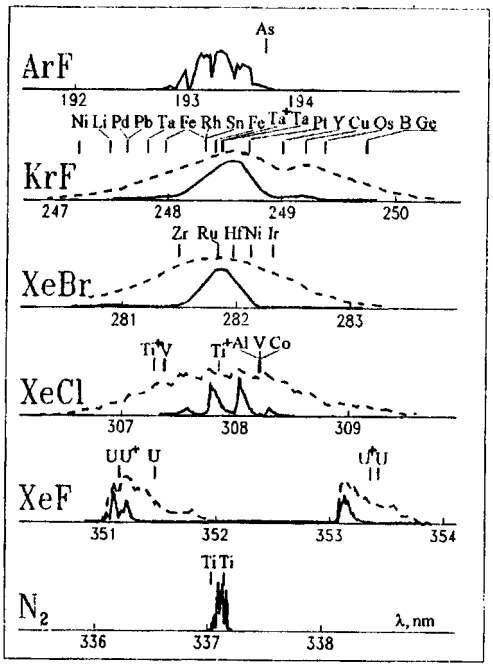

FIG. 1. Emission spectra of excimer and nitrogen lasers (solid curves) and resonance lines of atoms and some ions. Dashed curves — luminescence spectra of corresponding excimer molecules.

$$F_\lambda^s = \frac{16\pi^2\hbar c^2}{\lambda^5}\left(1+\frac{\Sigma_k A_{2k}}{A_{21}}\right) = \frac{1.4\cdot 10^{14}\xi}{\lambda^5[\mathrm{nm}]}\left[\frac{\mathrm{kW}}{\mathrm{cm}^2\cdot\mathrm{nm}}\right],$$

where A_{lm} are the Einstein coefficients, the subscripts 1 and 2 denote the ground and resonance levels, respectively, k are the intermediate levels (if they exist), and ξ denotes the expression in parenthesis. The value of F_λ^s depends very weakly on the wavelength and for a KrF laser is 150 kW/cm^2nm, which is quite feasible for ordinary lasers.

The superior reliability of excimer lasers, combined with their long operating life and their capacity to operate at frequencies of the order of 100 Hz, suggests that ultraviolet LIBORS may be a convenient means of creating a ''cold'' plasma of the elements shown in Fig. 1 for various applications, such as ion sources. Moreover, ultraviolet LIBORS may be used to generate a plasma of almost any elemental composition provided that, depending on the particular conditions, the plasma contains a certain amount of a suitable element to absorb the laser radiation and serve as a catalyst for the ionization processes. This method, which may be called ''catalytic resonance ionization'' (CATRION), may be suitable for ion sources with subsequent separation of the accelerated ions. It may also be used to generate the anode plasma in pulsed light-ion accelerators for thermonuclear fusion, where a small percentage of significantly heavier impurities is permissible.

Special investigations of the processes in multicomponent media in a resonant radiation field are required to optimize the conditions for CATRION, although one factor which may prove critical for the implementation of this method can be immediately identified. This is the high probability for electron-induced ionization of the catalyst atoms compared with other atoms in the mixture, because of the high population of the resonance level in the laser radiation field. This factor may result in the complete loss of atoms that absorb the laser radiation and in termination of the process before the medium has been completely ionized.[1)] However, there are two elements, uranium and tantalum, for which the resonance transitions of the atom and the singly charged ion are excited by the same excimer laser (XeF and KrF, respectively). When these elements are used as the catalyst, even after they have been completely ionized, the gas will continue to be ionized by heating of electrons in collisions with resonantly excited catalyst ions, which are difficult to ionize because of their higher ionization potential.

Experiments in which single-component tantalum and molybdenum targets were evaporated in vacuum by a focused KrF laser beam, showed that the threshold power density at which Langmuir probes record significant ionization of the expanding vapor is 1.6 times lower for tantalum compared with molybdenum, even though in accordance with the thermodynamic and atomic characteristics of these elements with no allowance made for resonance effects, this threshold power density should be higher for tantalum. Resonance effects were observed earlier in Ref. 5, when aluminum was exposed to XeCl laser radiation. The use of a single laser pulse both for evaporation and for ionization obviously prevents the process from being optimized, as was demonstrated in Ref. 10. Thus, in subsequent experiments, the vapor cloud was created independently by evaporating a target with ruby laser radiation (0.2 J, 25 ns), and was then irradiated by a KrF laser (0.2 J, 150 ns) with a controllable delay.

A planar target of specific elemental composition was placed in a vacuum chamber. The ruby laser beam was incident normally on the target and a broad KrF laser beam irradiated the cloud from the side, at an angle between 50° and 0°. The expanding gas (plasma) cloud was investigated with the aid of three Langmuir probes, a Faraday cup, a secondary-emission detector, a two-section photodiode measuring the deflection of an HeNe laser beam in the cloud,[11] a PIM-104V image converter, and two monochromators, one with a photomultiplier to monitor the intensity and the other, with an LI-602 dissector, to measure the spectral line width. The spatial distribution of the ruby and HeNe laser intensity was measured with a linear CCD array. In the experiments we used single-component (Ta, Ti, Mo, Pb, Fe, Sn, Cu, and Ni) and two-component (TaTi, Ta–B, and Fe–B) targets. The latter were fabricated by pressing from powders either explosively (TaTi) or at high temperature. Results are presented below only for targets containing tantalum and titanium.

After evaporation of the target by ruby laser radiation, a cloud of vapor containing a total number N_0 of up to 3×10^{16} particles expands into vacuum at characteristic velocities of $0.1-1$ cm/μs. The initial degree of ionization of the cloud depends on the power density of the incident radiation, and at the optimum power density[13] corresponds to the evaporation temperature of the target material. Since the density of the cloud needed to achieve the LIBORS mechanism in a time of around 0.1 μs may be estimated as $10^{15}-10^{16}$ cm^{-3}, the delay of the ionizing KrF laser pulse should not exceed a few microseconds. Frame-mode photo-

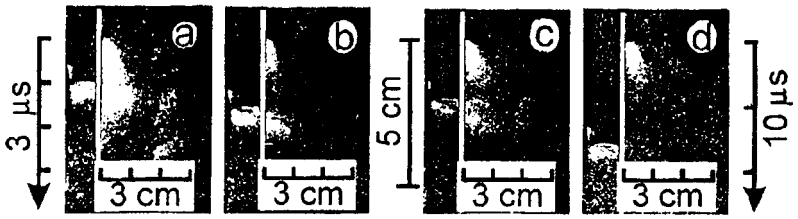

FIG. 2. Frame photograph (with simultaneous vertical sweeping of the image) of gas cloud evaporated by a ruby laser pulse from a tantalum target in vacuum (the light strip shows the position of the target). The expanding cloud is irradiated by a broad KrF laser beam whose triggering time can be seen from the bright spot 'behind'' the target.

graphs in the visible range obtained with the image converter, as well as the signals from the Langmuir probes and the spectroscopic diagnostics, confirm that additional ionization occurs in the part of the cloud adjacent to the target for the tantalum and tantalum-titanium targets, and is entirely absent in the titanium cloud.

Figure 2 shows photographs of the luminescence from the cloud, obtained with the image converter operated in a mixed, framing–streak-camera mode. The cloud was imaged onto the photocathode of the image converter and its electronic image at the exit was swept parallel to the target (downward in the figure) during exposure by applying a linearly rising voltage to the deflector plates. Initially, after irradiation of the target by the ruby laser, we observe an expanding weakly ionized cloud of vapor emitting in the continuum, as shown by the spectroscopic diagnostics. This emission is caused by the high temperature of the cloud (of the order of the evaporation temperature of the material) and decays in a time of the order of a microsecond as a result of a drop in the temperature and density of the cloud. If the intensity of the ruby laser radiation is not too high, the cloud exhibits negligible ionization, as is shown by the Langmuir probe signals.

Irradiation of a cloud containing no catalyst element (Ti target) with a KrF laser does not change the observed pattern (Ref. 11, Fig. 5). However, if the cloud contains tantalum (Ta and TaTi targets), provided that the delay of the KrF laser pulse does not exceed 5 μs, we observe a repeated, rapidly decaying flash of vapor luminescence, which initially contains intense, continuum emission and then, at the decay stage, contains line emission of atoms and ions. The observed emission cannot be scattered laser radiation which has not been transmitted by the glass optics, and is attributed to additional ionization of the cloud by heated electrons. This supposition is supported by the appearance of a second peak, of slightly greater amplitude than the main peak, on the 'tails'' of the probe signals (Ref. 11, Fig. 7) for the tantalum–titanium target, by the absence of such a peak for the titanium target, as well as by the spectroscopic measurements. When the triggering delay of the KrF laser is increased, the second peak of the probe current shifts to the right and decreases in magnitude. A small increase in the probe current in the second peak should not confuse the issue because, even when the cloud is completely ionized, the characteristic three-particle recombination time at a density of $\sim 10^{15}$ cm^{-3} and a temperature of ~ 0.5 eV does not exceed a microsecond,[13] and at the expansion stage, a fairly low degree of ionization, weakly dependent on the initial degree, is established in the cloud. The most reliable evidence that the cloud is ionized by the excimer laser radiation is provided by the experimentally observed change direction, and simultaneous increase in the angle, of deflection of the HeNe laser beam (Ref. 14, Fig. 5) propagating at a distance of 1 mm from the surface of the target, at the instant when the cloud is irradiated by the KrF laser. This 'positive'' deflection (by electrons) is between two and three times greater than that predicted from the polarizability ratio between a ground-state tantalum atom ($+7$ Å^3, Ref. 15) and an electron (-28 Å^3, Ref. 15), which may well be caused by the incorporation of dissolved gases in the tantalum, which then appears in the cloud. The deflection returns to its former 'negative'' value 100 ns after the end of the pulse, probably as a result of rapid three-particle recombination at the estimated cloud density of $\sim 10^{16}$ cm^{-3}.

According to estimates, which are not given here because of a lack of space, direct photoionization of resonantly excited atoms cannot produce any significant ionization of the cloud, whereas all the experimental observations support the radiative collisional mechanism for the ionization processes.

The authors would like to thank I. M. Bushuev and Art. Ivanov for assistance with the experiment.

The work was carried out using the CATRION system (Reg. No. 06-06) with the financial support of the Russian Ministry of Science, Grant 95-0-5.2-185, the 'Russian Universities'' Program of the State Committee for Higher Education of the Russian Federation, and also the Forschungszentrum, Karlsruhe.

[1)]In principle, this process may be used to develop a laser negative-ion source by creating conditions for the attachment of electrons to specially added electronegative atoms during decay of the plasma.

[1] T. B. Lucatorto and T. J. McIlrath, Phys. Rev. Lett. **7**, 280 (1976).
[2] R. M. Measures and P. G. Cardinal, Phys Rev. A **23**, 804 (1981).
[3] V. A. Kas'yanov and A. N. Starostin, in *Plasma Chemistry* [in Russian], Énergoatomizdat, Moscow (1990), p. 67.
[4] K. V. Bieg, G. C. Tisone, T. R. Lokner *et al.*, *Proceedings of the Eighth International Conference on High-Power Particle Beams*, Novosibirsk, 1990, Vol. 2 (World Scientific), p. 933.
[5] D. V. Gaidarenko and A. G. Leonov, Laser Phys. **2**, 901 (1992).
[6] H. Yoshida, R. Tamaki, and H. Ninomiya, Opt. Commun. **102**, 461 (1993).
[7] B. A. Knyazev, P. I. Melnikov, and H. Bluhm, Preprint No. 94–8, Budker Institute of Nuclear Physics, Novosibirsk (1994).
[8] I. I. Sobelman, L. A. Vainshtein, and E. A. Yukov, *Excitation of Atoms and Broadening of Spectral Lines* (Springer-Verlag, Berlin, 1981) [Russ. original, Nauka, Moscow, 1979].
[9] V. M. Akulin and N. V. Karlov, *Intense Resonance Interactions in Quantum Electronics* [in Russian], Nauka, Moscow (1987).
[10] B. A. Knyazev, S. V. Lebedev, and K. I. Mekler, Zh. Tekh. Fiz. **56**, 1319 (1986) [Sov. Phys. Tech. Phys. **31**, 773 (1986)].
[11] I. M. Bushujev, A. A. Doroshkin, A. A. Ivanov *et al.*, Proc. SPIE **2619**, 216 (1995).

[12] S. I. Anisimov, Yu. A. Imas, G. S. Romanov, and Yu. V. Khodyko, *Action of High-Power Radiation on Metals* [in Russian], Nauka, Moscow (1970).
[13] Yu. P. Raĭzer, *Physics of Gas Discharges* [in Russian], Nauka, Moscow (1987).
[14] B. A. Knyazev, P. I. Melnikov, A. A. Doroshkin *et al.*, *Proceedings of the 11th International Conference on High-Power Particle Beams*, Prague, 1996, Vol. 2, p. 1195.
[15] S. Fraga and J. Muszyńska, in *Physical Sciences Data 8. Atoms in External Fields* (Elsevier, 1981), p. 53.

Translated by R. M. Durham

Simulation of iron fracture caused by a blast wave

A. V. Chizhov, V. O. Chistyakov, and A. A. Schmidt

A. F. Ioffe Physicotechnical Institute, Russian Academy of Sciences, St. Petersburg
(Submitted December 9, 1996)
Pis'ma Zh. Tekh. Fiz. **23**, 33–39 (May 12, 1997)

A numerical simulation is made of the fracture of iron caused by a blast wave. The numerical method is described and results of calculations using a one-dimensional formulation of three qualitatively different explosion regimes are presented. © *1997 American Institute of Physics.* [S1063-7850(97)00605-8]

1. An analysis is made of a planar layer of metal, at one of whose free surfaces explosion energy is released over a certain time interval, which determines the pressure on the surface. A shock compression wave and rarefaction waves propagate in the metal. The compression wave interacts with the other free boundary of the metal, forming secondary rarefaction waves propagating inside the sample. Depending on the parameters of the explosion, either the secondary rarefaction waves near the free surface, or interaction between the primary and secondary rarefaction waves inside the metal, induce tensile stresses exceeding the strength threshold, i.e., they cause the metal to fracture.

Over a wide range of explosion powers, the state of iron is described by the isothermal equation of state.[1] This equation of state has the following characteristics: at a pressure of the order of 1.3×10^5 bar an $\alpha\rightarrow\varepsilon$ phase transition is initiated, and the tensile strength is reached at tensile stresses of the order of 3000 Mbar.

These characteristics are responsible for rarefaction shock waves in the iron.

2. Mathematical modeling of the wave interaction in a metal involves solving a system of equations for the flow of a compressible fluid. In the Lagrangian formulation, these equations have the form

$$\rho\frac{\partial u}{\partial t}+\frac{\partial p}{\partial x}=0,$$

$$\frac{1}{\rho}\frac{\partial \rho}{\partial t}+\frac{\partial u}{\partial x}=0, \tag{1}$$

$$p=p(\rho).$$

Here we have $x=x(\xi,t)$, where ξ is the Lagrangian coordinate; $0<\xi<L$, where L is the initial thickness of the sample.

Equation of state. We used the equation of state written in the Mie–Grüneisen form:

$$p=\left(\frac{\rho}{\rho_0}\right)^{\frac{2}{3}}\exp\left[b\left(1-\left(\frac{\rho}{\rho_0}\right)^{-\frac{1}{3}}\right)\right]-K\left(\frac{\rho}{\rho_0}\right)^{\frac{4}{3}},$$

where, for the first phase ($\rho\leqslant 8418$ kg/m^3): $A=9.974\times10^5$ bar, $K=10.164\times10^5$ bar, and $b_1=7.098$, and for the second phase ($\rho\geqslant 8810$ kg/m^3): $A=9.439\times10^5$ bar, $K=10.740\times10^5$ bar, and $b_1=7.784$. The phase transition condition is assumed to be: $p=1.3\times10^5$ bar for 8418 kg/m$^3<\rho<$8810 kg/m^3. The fracture condition is assumed to be: $p=3000$ bar for $\rho<7846$ kg/m^3. The curve $p(\rho)$ is plotted in Fig. 1.

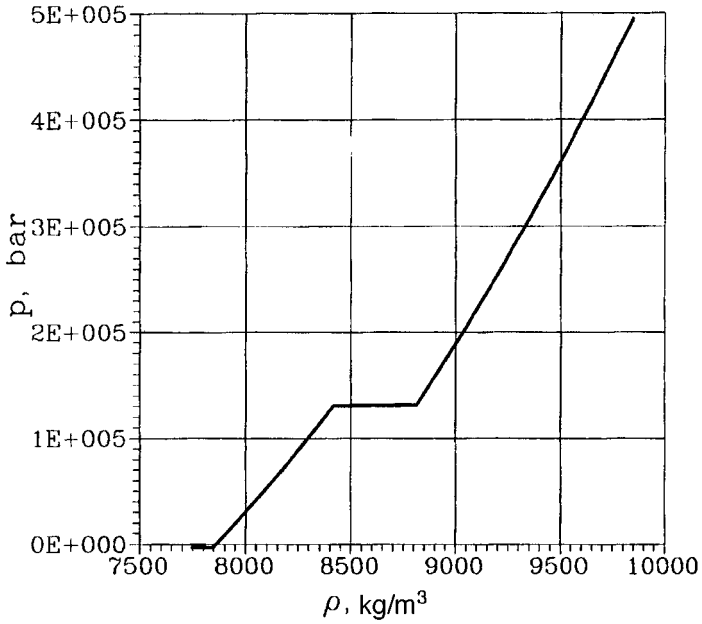

FIG. 1. Equation of state for iron.

 1063-7850/97/050347-03$10.00

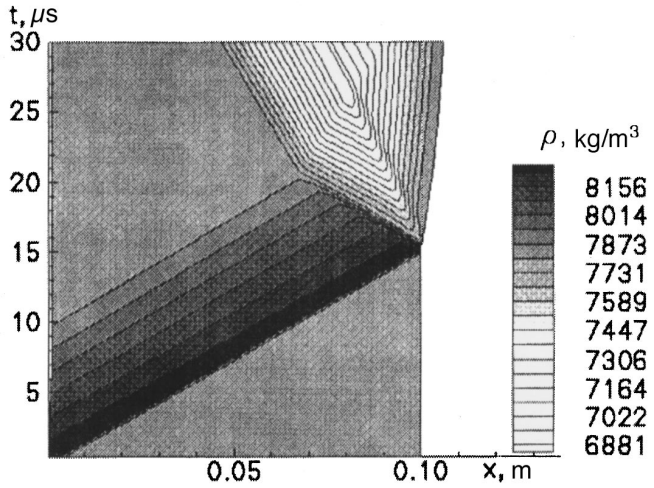

FIG. 2. Density: $p_{\max}=0.1\times10^6$ bar, $E=800$ J/m^2.

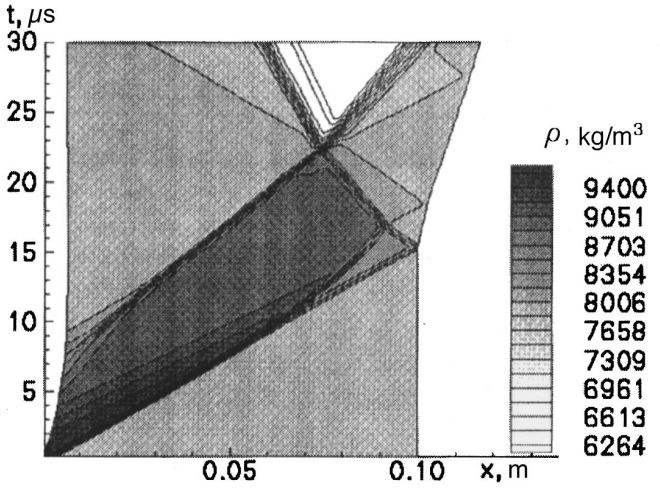

FIG. 3. Density: $p_{\max}=0.5\times10^6$ bar, $E=9300$ J/m^2.

Boundary conditions. The release of energy is simulated by setting a linear time dependence for the pressure at the ''left'' boundary of the metal:

$$\rho|_{\xi=0}=(\rho_w-\rho_0)\left(1-\frac{t}{\Delta t_w}\right)+\rho_0, \quad \text{for } t<\Delta t_w.$$

Here, Δt_m is the duration of the explosion and ρ_w determines the maximum pressure of the explosive on the surface of the metal. These quantities define the energy transferred per unit surface area of the metal:

$$E_w=\int_{x(0,t)}^{x(L,t)}\left(\frac{\rho u^2}{2}+\varepsilon\right)dx, \quad \text{for } t\geqslant\Delta t_w,$$

where the internal energy is determined from the equation of state

$$\varepsilon=\int_{\rho_0}^{\rho}\frac{p(\rho)}{\rho^2}d\rho.$$

The boundary conditions on the free surfaces are

$$\rho|_{\xi=o}=\rho_0 \quad \text{for } t\geqslant\Delta t_w, \quad \rho|_{\xi=L}=\rho_0 \quad \text{for } t\geqslant0.$$

3. The construction of the numerical scheme is described in detail in Ref. 2. For a nearly conservative formulation of the equations (1), the numerical scheme at point i is written as

$$u_t+\Theta\left[\phi_x-\frac{\Delta x}{2}au_{xx}+\frac{\delta x}{2}a(\overline{u_x})_x-\frac{\delta x}{2}\frac{\Delta x}{2}a^2(\overline{(\ln\rho)_x})_{xx}\right]=0,$$

$$(\ln\rho)_t+\Theta\left[u_x-\frac{\Delta x}{2}a(\ln\rho)_{xx}+\frac{\delta x}{2}a(\overline{(\ln\rho)_x})_x-\frac{\delta x}{2}\frac{\Delta x}{2}(\overline{u_x})_{xx}\right]=0,$$

$$x_t=u,$$

where

$$\Theta=1+\frac{\Delta t\rho}{2a}\frac{\partial a}{\partial\rho}(\ln\rho)_t,$$

$$\Delta x=\max(x_{i+1}-x_i,x_i-x_{i-1}), \quad \delta x=\Delta x-a\Delta t.$$

The limited derivatives $\overline{u_x}$ and $(\ln\rho)_x$ are expressed in terms of the variables $r^+=u+a\ln\rho$ and $r^-=u-a\ln\rho$:

$$\overline{r_x^{\pm}}=\text{limiter}\left[r_x^{\pm}-\frac{\Delta x}{2}r_{xx}^{\pm},r_x^{\pm}+\frac{\Delta x}{2}r_{xx}^{\pm}\right].$$

Here, $a=\sqrt{\partial p/\partial\rho}$ is the velocity of sound and $\phi=\int_{\rho_0}^{\rho}(a^2/\rho)d\rho$. The subscripts indicate numerical derivatives. The time derivatives are constructed following a two-layer scheme, and the spatial derivatives are constructed using the Galerkin finite-element method. We use a limiter expressed in the Van–Leer form.

The proposed scheme is quasimonotonic for $(a+|n|)\Delta t/\Delta x<1$.

4. The simulation revealed that there are three qualitatively different regimes of interaction between a plane blast wave and a planar layer of iron, caused by the presence of a $\alpha\rightarrow\varepsilon$ transition.

The first case corresponds to a blast wave of small amplitude when no phase transition takes place. In this case, the blast wave inside the metal has the form characteristic of a normal gas, i.e., the compression shock is followed by a rarefaction wave (no rarefaction shocks are formed). The blast wave is reflected from the ''right'' free boundary as a strong but smooth rarefaction wave. The free boundary is accelerated, and the tensile stresses near the boundary exceed the tensile strength of the metal, thus causing fracture. The fracture region on the $x-t$ density diagram (Fig. 2), can be identified as the region where the density is below the critical limit for continuity.

In the second case (Fig. 3), the amplitude of the blast wave is such that a phase transition takes place at the fronts of the compression shock wave and the rarefaction wave. For short transition times, applicable to a wide range of parameters, the compression wave splits into two compression shocks connected by a phase transition zone at constant pres-

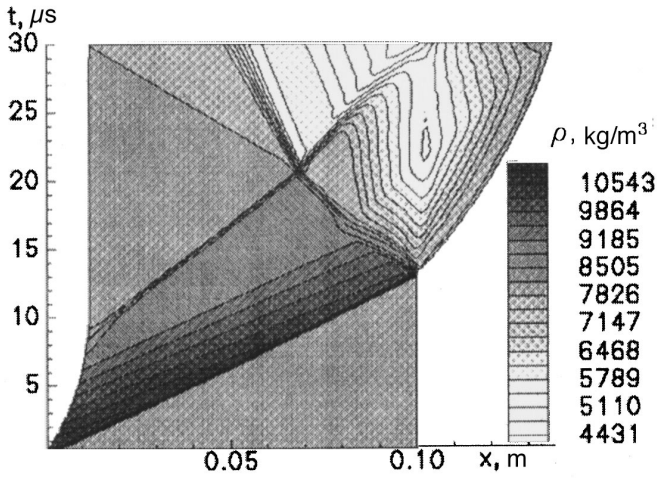

FIG. 4. Density: $p_{max}=1.2\times10^6$ bar, $E=36000$ J/m^2.

sure. The rarefaction wave comprises a region of continuously decreasing density, a region of constant density, a rarefaction shock wave, and another region, where the density falls smoothly to its initial value. The first compression shock, corresponding to the α-phase, is reflected as a rarefaction wave from the right-hand boundary, accelerating the free surface, beyond which the pressure is restored to its unperturbed level. The rarefaction wave interacts with the second compression shock, corresponding to the ε-phase, and acquires the form of a shock. This rarefaction shock interacts with the incident rarefaction shock on a certain line in the metal (at the point $x=0.075$ m, $t=23$ μs on the diagram), causing fracture of the metal. This pattern of interaction between a blast wave and a layer of iron agrees with the experimental data.[1]

In the third case (Fig. 4), the amplitude of the blast wave is so great than the compression wavefront does not split and is reflected from the free surface as a smooth, but strong, rarefaction wave, causing fracture of the metal near the free surface. The reflected rarefaction wave interacts with the continuous section of the incident rarefaction wave, forming a rarefaction shock wave. This rarefaction shock wave interacts with the rarefaction shock wave of the incident wave on a certain line in the metal (at a certain point $x=0.07$ m, $t=21$ μs), causing another fracture in the metal, as in the second case.

5. To sum up, we have proposed an algorithm to simulate fracture of a metal and have obtained three qualitatively different wave propagation and interaction regimes in a sample that undergoes a phase transition.

This work has been partially supported by the Russian Fund for Fundamental Research (Grant No. 95-01-00521a).

[1] L. V. Al'tshuler, Usp. Fiz. Nauk. **85**, 197 (1965) [Sov. Phys. Usp. **8**, 52 (1965)].
[2] A. V. Chizhov and A. A. Schmidt, *Proceedings of the Ninth International Conference on Finite Elements in Fluids*, Italy, 1995, Vol. 2, pp. 1019–1028.

Translated by R. M. Durham

Mechanism for electrochemical synthesis of diamond-like carbon

V. P. Novikov and V. P. Dymont

Institute of Solid-State Physics and Semiconductors, Belarus Academy of Sciences
(Submitted November 28, 1996)
Pis'ma Zh. Tekh. Fiz. **23**, 40–45 (May 12, 1997)

Some unusual features of the low-temperature electrochemical synthesis of diamond-like carbon are described. It is shown that the electrochemical synthesis of carbon is catalyzed by transition metals, and the formation of a film on the electrode is preceded by the formation of a colloidal solution and a carbon gel. © *1997 American Institute of Physics.* [S1063-7850(97)00705-2]

In Refs. 1 and 2 we demonstrated the possibility of obtaining diamond-like carbon films from a liquid electrolyte by an electrochemical method. The process has various unusual features, such as the electrolytic growth of high-resistivity films, as well as the strong influence of the anode material on the synthesis process and the properties of the films. This behavior may be explained if we assume that the carbon synthesis is catalyzed by metal ions, and that the carbon particles are nucleated in the anode region, and then move toward the electrode by electrophoresis.

The aim of the present paper is to check out these assumptions, and also to study in greater detail the properties of electrochemically synthesized carbon.

The carbon was synthesized by the method described in Ref. 1. The electrolyte consisted of a solution of acetylene in liquid ammonia. The parameters of the deposition process varied in the following ranges: solution temperature between -33 and -70 °C, voltage 2–5 V, and cycle duration 5–10 h.

We tested two electrode materials — nickel and graphite — to determine the influence of the electrode material on the carbon synthesis process.

After electrolysis had been completed, the electrolyte was poured into a flat dish, and evaporated to observe the colloidal particles.

Fabric was stretched over the surface of the anode to observe the gel, which was retained in the cells of the fabric by capillary forces.

By carrying out experiments using this procedure, we established that with a nickel electrode, a layer of colorless, transparent, gel-like substance was formed on the surface of the solid, glassy film and after the electrolyte had evaporated, a transparent, gel-like film was left at the bottom of the dish. When the graphite anode was used for the electrolysis, no films were synthesized and no deposit was formed. However, the addition of soluble nickel salts (and also the salts of some other transition metals, such as Co and Fe) to the electrolyte initiated the electrochemical synthesis of carbon with the graphite anode. These experiments demonstrate that transition metal ions play an important role in the electrochemical synthesis of carbon.

The gel-like substance, collected from the surface of the electrode and from the bulk of the electrolyte, exhibited unusual behavior: when heated between $+20$ and $+100$ °C, this substance spontaneously transformed into a collection of thin, colorless, transparent fibers and leaves. At temperatures of $100-900°$, the size and shape of these formations remained constant. However, at temperatures above 950 °C, the thickness of these fibers and leaves began to decrease further and their length increased (Fig. 1). The annealed samples did not dissolve in acids or in organic solvents. Their resistivity was higher than $10^{12}\ \Omega\cdot$cm.

Auger spectroscopic data indicate that the amount of carbon in the annealed fiber samples was 95–99.9 wt .%. The total amount of nickel, nitrogen, and oxygen was $\leqslant 5\%$. Layer-by-layer ion etching revealed that the composition of the film does not vary with thickness. The Raman scattering spectrum, shown in Fig. 2, allows us to classify this substance as diamond-like carbon.

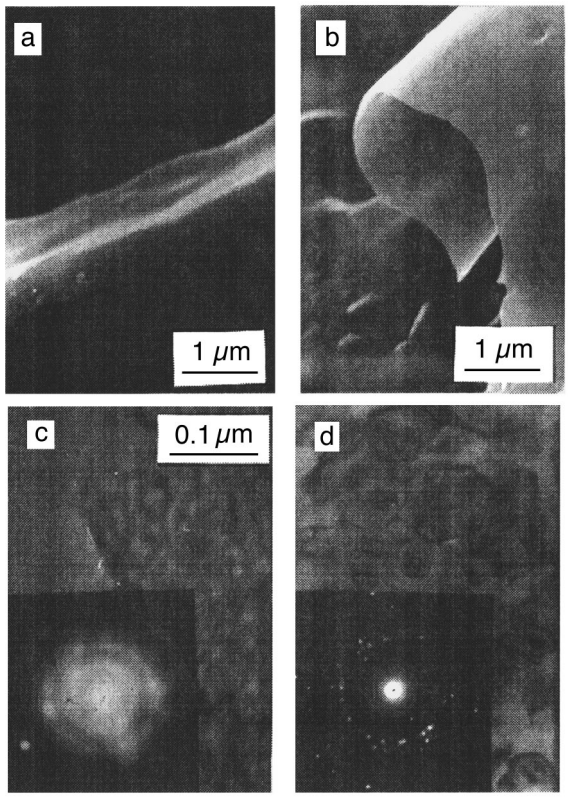

FIG. 1. Electron microscope images of diamond-like carbon obtained from a gel: a, b — surface microrelief of samples annealed at 950 °C/2 h; c — ''transmission'' image of sample obtained by drying the gel at 50 °C, and d — sample annealed at 900 °C/2 h. The insets show the corresponding electron diffraction patterns.

 1063-7850/97/050350-02$10.00

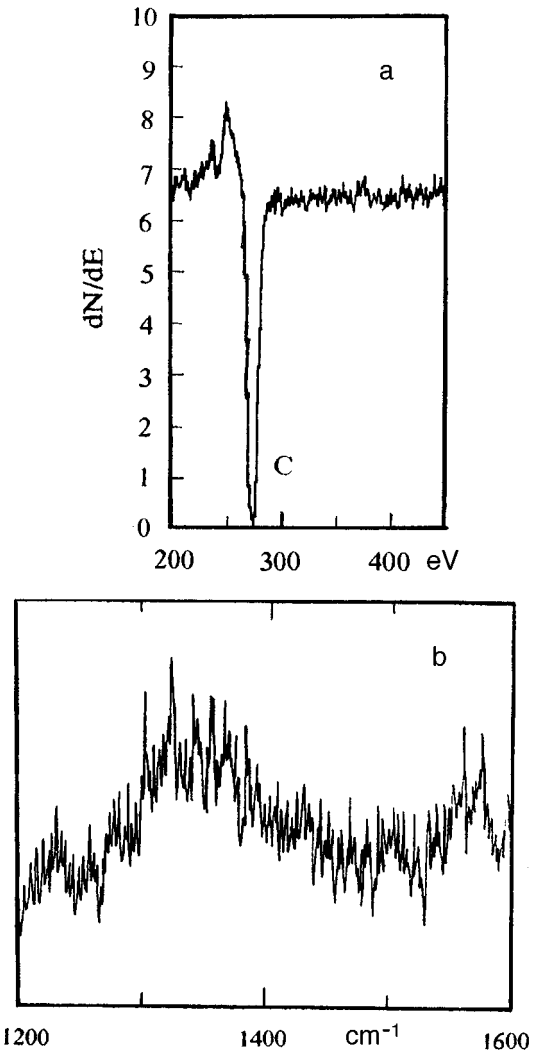

FIG. 2. Spectra of sample obtained by drying the gel at 50 °C (a — Auger spectrum, b — Raman spectrum).

The structure of the carbon obtained by this electrochemical method was investigated by transmission electron diffraction. Samples obtained from the gel at room temperature contained amorphous and crystalline components. The samples annealed at 900 °C exhibited a polycrystalline structure with a crystallite size of 0.1 μm (Fig. 1). The interplanar spacings d, calculated from the diffraction patterns, agreed with similar data calculated for diamond (see Table I). However, the diffraction pattern of this substance revealed peaks whose positions matched forbidden peaks in diamond. A similar effect is observed in diamond films and is attributed to distortion of the crystal lattice.[3] However, such an interpretation is unconvincing in our case, because the intensity of the ''forbidden'' peaks is comparable with that of the allowed ones. We put forward the hypothesis that this substance is a new modification of carbon.

We propose a mechanism for the electrochemical synthesis of carbon, which takes into account the catalytic action of transition metals on this process as well as the known property of transition-metal ions to form complexes with acetylene.[4] We postulate that the ions entering the electrolyte take part in the following reactions:

1) coordination of acetylene molecules by the formation of a π-complex;

2) dehydrogenation of oligomers and the formation of molecule-radicals. These molecule-radicals are then polymerize to form a diamond-like substance.

The overall process may be expressed by the following equations:

$$C_2H^- + Me^{+2} \overset{NH_3}{\Rightarrow} Me(C_2H)_4^{-2} \quad \overset{electrode-8e}{\Rightarrow} \quad 8C + Me^{+2} + 4H^+.$$

The capacity of ammonia to stabilize free radicals[5] probably plays an important role in the synthesis mechanism, allowing the synthesis process to take place, not only at the electrode surface but also in the bulk of the electrolyte, to form a colloidal solution of carbon. The carbon particles move toward the anode by electrophoresis, where they become concentrated, forming a layer of gel near the anode, and then a solid film.

These experiments have demonstrated that the electrochemical synthesis of carbon is catalyzed by transition-metal ions, and that the formation of a film on the electrode is preceded by the formation of a colloidal solution and a gel. After drying or annealing, this substance possesses properties characteristic of diamond: transparency, high electrical resistivity, and thermal stability, but its structure differs from that of diamond, as does its capacity for spontaneous formation of fibers and leaves. This behavior suggests that this substance is a new form of carbon.

To conclude, we note that because the observed substance may be obtained as a gel and because of its capacity for spontaneous formation of leaves and fibers, it may be a convenient component in the technology of composites.

TABLE I. Interplanar spacings of electrolytic carbon and diamond.

Electrolytic carbon		Diamond ($a=0.357$ nm) (ASTM data)	
Intensity	d, nm	d, nm	$h^2+k^2+l^2$
Strong	0.36	0.357	1
Weak	0.24	0.251	2
Very strong	0.21	0.206	3
Weak	0.18	0.178	4
Strong	0.13	0.126	8
Weak	0.11	0.107	12

[1] V. P. Novikov and V. P. Dymont, Dokl. Akad. Nauk Belarus **40**(1), C7 60 (1996).
[2] V. P. Novikov and V. P. Dymont, Pis'ma Zh. Tekh. Fiz. **22**(7), 39 (1996) [Tech. Phys. Lett. **22**, 283 (1996)].
[3] E. G. Spenser, P. H. Schmidt, D. C. Joy *et al.*, Appl. Phys. Lett. **29**, 118 (1976).
[4] A. N. Nesmeyanov and N. A. Nesmeyanov, *Principles of Organic Chemistry*, Vol. II [in Russian], Khimiya, Moscow (1970), p. 474.
[5] H. Remy, *Treatise on Inorganic Chemistry* [Russ. transl., Mir, Moscow, 1974], p. 716.

Translated by R. M. Durham

Formation of a honeycomb domain structure in magnetic films

M. V. Logunov and N. V. Moiseev

N. P. Ogarev Mordovian State University, Saransk
(Submitted November 4, 1996)
Pis'ma Zh. Tekh. Fiz. **23**, 46–51 (May 12, 1997)

An analysis is made of the possible formation of a honeycomb domain structure directly from a labyrinth structure in uniaxial magnetic films exposed to a series of uniform magnetic field pulses. It is shown that the scenario for the formation of a honeycomb structure depends on the pulse parameters and on the magnitude of the static magnetizing magnetic field. © *1997 American Institute of Physics.* [S1063-7850(97)00805-7]

Processes involving the dynamic self-organization of the magnetic moment in thin magnetic films have recently attracted major interest. In addition to the thoroughly studied stripe and magnetic bubble domain structures,[1] ring and spiral domains, and various modifications of magnetic bubble patterns have been observed and studied.[2–5] A honeycomb domain structure is usually formed from a disordered (labyrinth) structure in several stages:[1,6] a pattern is nucleated, for example, by a pulsed magnetic field, the pattern evolves into an ordered hexagonal structure under the action of a smoothly decreasing ac field, and a honeycomb structure is finally formed by applying a static magnetic field in the opposite direction to the magnetization in the magnetic bubble domains.

In the present paper, we consider the possible formation of a honeycomb domain structure directly from a labyrinth structure in uniaxial magnetic films exposed to a series of uniform magnetic field pulses. The scenario for formation of the honeycomb structure depends on the pulse parameters and on the static magnetic field magnetizing the film.

The domain structure was studied by high-speed photography,[7] utilizing the Faraday effect. The magnetic field pulses were generated by an electromagnet, formed by a ten-turn Helmholz coil with a diameter of 2.5 mm, and a current pulse generator. The samples were single-crystal iron garnet films with the easy axis perpendicular to the plane of the film. Results are presented for a sample having the composition $(Bi, Yb)_3(Fe,Ga)_5O_{12}$ (Ref. 8) with the parameters: thickness $h=9.5$ μm, equilibrium stripe-domain period $P_0=11.9$ μm, saturation magnetization $4\pi M_s=127$ G, and uniaxial anisotropy field $H_k=720$ Oe.

A static magnetic bias field H_b was applied to the film in the initial state along the easy axis. The field H_b changes the size and shape of the labyrinth domains, but the structure remains disordered (Fig. 1a). The application of small-amplitude magnetic field pulses H_p in the direction opposite to H_b has a similar effect. The response of the domain structure to the pulsed action changes fundamentally above the threshold H_p and the pulse length t_p: the labyrinth structure undergoes rearrangement and domain clusters are formed with a new topology — a honeycomb domain structure (Fig. 1b). The cells of the honeycomb structure are mainly formed at the 'branching'' points of stripe domains. When a series of pulses is applied, the cluster fields migrate over the area of the film and join together to form large sections with a honeycomb structure (Fig. 1c). Ultimately, the entire observable area of the sample exhibits a honeycomb structure (Fig. 1d). Each cell is bounded by six others and some cells have five, seven, or eight neighbors.

We note the following main features of the formation of the honeycomb structure: the process is observed in a narrow range of pulsed magnetic fields H_p, which depends on the pulse length t_p and the bias field H_b. For fixed H_b and H_p, the process may be characterized by the number of H_p pulses needed to form the simplest elements of the honeycomb structure — clusters of four cells (Fig. 2a). Clusters of two or three cells are unstable. The formation of the honeycomb structure does not depend on the repetition frequency of the magnetic field pulses, only on their number (Fig. 2b).

After saturation has been reached (Fig. 2b), the honeycomb structure occupies the entire observable area of the sample, around 1 mm in diameter. Subsequent H_p pulses do not change its density. The honeycomb structure is more stable than the labyrinth structure and the action of H_p does not cause major rearrangement or displacement of the structure over the sample. Only local rearrangements may occur, involving the nucleation or collapse of individual cells (these are usually cells having a number of neighbors other than six), which lead to disordering of the structure and the formation of hexagonal cells.

The formation process depends very strongly on the magnetic field pulse length t_p. For given H_p and H_b, there is a minimum of t_p below which the process is not observed. For $t_p > t_p$, the range of fields capable of sustaining a honeycomb structure is increased. In our experiments, the threshold is $t_p=0.4$ μs and the results plotted in Figs. 1 and 2 are given for a pulse length $t_p=2$ μs.

The honeycomb structure is formed by breakup of stripe domains under the action of the H_p field pulses, followed by ordering as a result of the magnetostatic interaction of the domains in the bias field H_b. It can be seen from Fig. 2a that there is an optimum ratio of the fields $\tilde{H}_p$ and H_b most conducive to the formation of a honeycomb domain structure. The left-hand boundary of the region of H_b where the structure is formed (Fig. 2a), exists because the magnetic field $H_d=H_p-H_b$ acting on the domain structure is sufficient to magnetize the sample to saturation during a field pulse, and after the end of the pulse, a characteristic 'comb'' structure is formed as a result of demagnetization.[4,9] At the right-hand boundary, the driving field H_d (minimum) coincides with the

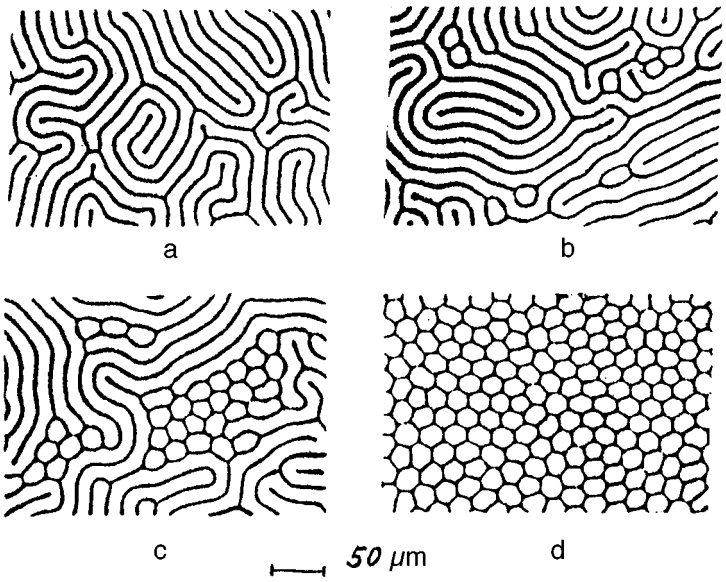

FIG. 1. Domain structures in the magnetic film in a bias field $H_b = 36$ Oe before (a) and after the application of n pulses of the field $H_p = 108$ Oe, where n, (10^3) is 5 (b), 25 (c), and 200 (d).

static field H_{cr} for deformation instability of an isolated stripe domain, calculated in Ref. 10, and the stripe domain contraction field in magnetic bubble domains.[11] The optimum field H_d for the formation of a honeycomb structure is 3–5 Oe less than H_{cr}.

However, according to Ref. 11, a stripe domain with fixed ends can only be broken down for $H_d \to 4\pi M_s$ ($H_d \gg H_{cr}$), which was confirmed by quasistatic experiments.[12] The probabilistic nature of the formation of a honeycomb structure in the present case, and the fact that this structure is observed in driving fields H_d, comparable with the critical field of linear domain boundary dynamics for this sample,[8] but smaller than the static field for breakdown of a stripe domain, indicate that the process is strongly influenced by the structure of the dynamic domain boundaries.

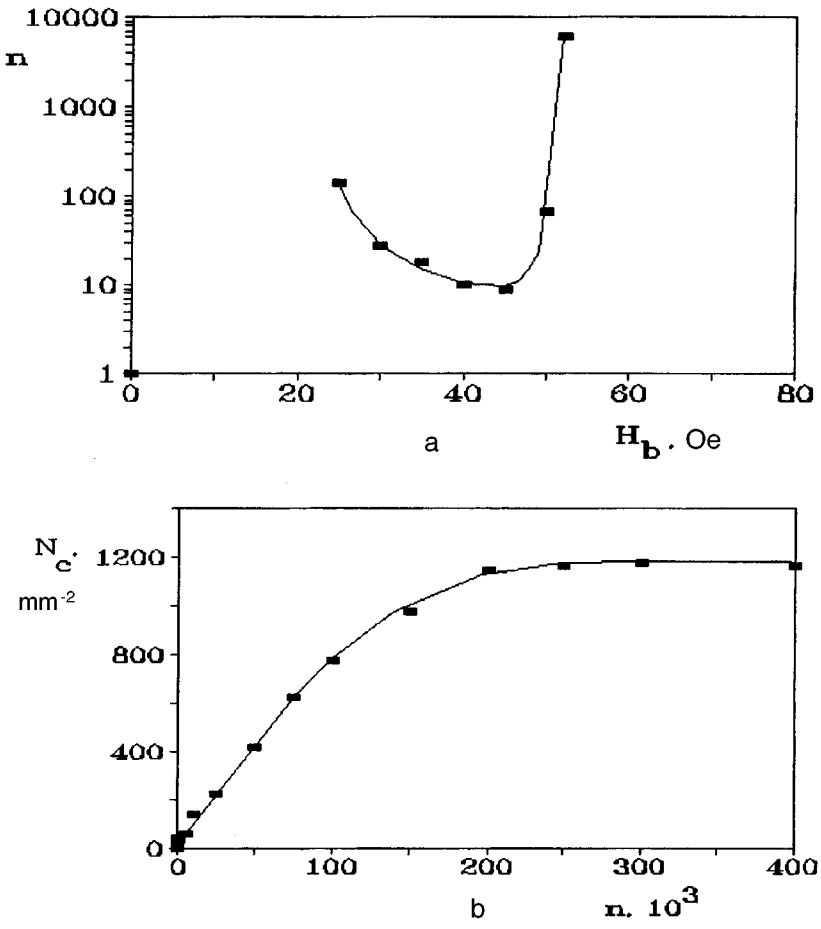

FIG. 2. a — Number of magnetic field pulses n needed to form the first cluster of four cells in a labyrinth structure as a function of the bias field H_b for $H_p = 116$ Oe; b — density of honeycomb structure N_c as a function of the number of magnetic field pulses n: $H_p = 108$ Oe, $H_b = 36$ Oe.

In intervals between magnetic field pulses, the honeycomb structure remains frozen for an arbitrarily long time. Thus, in the terminology adopted in Refs. 4 and 13, the honeycomb structure is a type of reflexive structure. Studies of the laws governing the behavior of a honeycomb domain structure in magnetic fields will provide a deeper understanding of the phenomenology of other honeycomb systems, such as the melting process of solids.[6]

The authors would like to thank V. V. Randoshkin and V. I. Chani for supplying the iron garnet films for this investigation.

[1] A. P. Malozemoff and J. C. Slonczewski, *Magnetic Domain Walls in Bubble Materials* (Academic Press, New York, 1973) [Russ. transl., Mir, Moscow, 1982].
[2] G. S. Kandaurova and A. É Sviderskiĭ. Zh. Éksp. Teor. Fiz. **97**, 1218 (1990) [Sov. Phys. JETP **70**, 684 (1990)].
[3] G. S. Kandaurova and A. E. Sviderskiy, Physica B **176**, 213 (1992).
[4] I. E. Dikshteĭn, F. V. Lisovskiĭ, E. G. Mansvetova, and E. S. Chizhik, Zh. Éksp. Teor. Fiz. **100**, 1606 (1991) [Sov. Phys. JETP **73**, 888 (1991)].
[5] F. V. Lisovskiĭ, E. G. Mansvetova, E. P. Nikolaeva, and A. V. Nikolaev, Zh. Éksp. Teor. Fiz. **103**, 213 (1993) [JETP **76**, 116 (1993)].
[6] K. L. Babcock, R. Seshadri, and R. M. Westervelt, Phys. Rev. A **41**, 1952 (1990).
[7] M. V. Logunov, V. V. Randoshkin, and V. B. Sigachev, Prib. Tekh. Éksp. No. 5, 247 (1985).
[8] A. A. Airapetov, M. V. Logunov, V. V. Randoshkin, and V. I. Chani, Pis'ma Zh Tekh. Fiz. **18**(2), 74 (1992) [Sov. Tech. Phys. Lett. **18**, 53 (1992)].
[9] V. G. Bar'yakhtar, V. L. Dorman, Yu. A. Kuzin *et al.*, Pis'ma Zh. Tekh. Fiz. **8**, 1306 (1982) [Sov. Tech. Phys. Lett. **8**, 562(1982)].
[10] F. L. Vaĭsman, Yu. N. Gorobets, and S. I. Denisyuk, Ukr. Fiz. Zh. **31**, 1234 (1986).
[11] J. A. Cape and G. W. Lehman, J. Appl. Phys. **42**, 5732 (1971).
[12] V. G. Bar'yakhtar, F. L. Vaĭsman, Yu. I. Gorobets, and V. L. Dorman, Ukr. Fiz. Zh. **29**, 872 (1984).
[13] A. A. Kal'yanin, *Microelectronics and Semiconductor Devices*, Part 10, [in Russian], Radio i Svyaz', Moscow (1989).

Translated by R. M. Durham

Influence of sulfide treatment of profiled-interface Au–GaAs Schottky diodes on the polariton peak of the photoresponse

M. L. Dmitruk, O. I. Maeva, S. V. Mamykin, and O. B. Yastrubchak

Institute of Semiconductor Physics, Academy of Sciences of Ukraine, Kiev
(Submitted December 23, 1996)
Pis'ma Zh. Tekh. Fiz. **23**, 52–57 (May 12, 1997)

We discuss the feasibility of controlling the photosensitivity of metal/thin intrinsic-oxide/semiconductor surface-barrier structures under conditions of excitation of surface polaritons. These structures may be used as polarization-sensitive photodetectors. © *1997 American Institute of Physics.* [S1063-7850(97)00905-1]

It has been established[1,2] that the excitation of surface polaritons at the external surface of the metal electrode in profiled-interface Schottky diodes may cause a resonant enhancement of the photoresponse of the structure in the fundamental absorption region of the semiconductor. The spectral position of the polariton peak is determined by the dispersion relation for the surface polaritons in a three-layer air/thin metal oxide/semiconductor system, slightly perturbed by the nonplanarity of the interface. Under conditions of plasma polariton resonance, the intensity of the electromagnetic field at the metal surface increases substantially, which is responsible for the parameters of the surface polaritons being highly sensitive to the optical properties of the adjacent media[3] and is used to control the resonance parameters.[4]

Sulfide passivation of the surface and metal–semiconductor interfaces has been used to reduce the surface recombination velocity by reducing the density of surface electronic states and improving the characteristics of surface-barrier structures utilizing III–V semiconductors.[5,6]

In the present paper, we examine the feasibility of controlling the spectral, polarization, and angular characteristics of the photoresponse of nonpassivated profiled-interface GaAs–Au Schottky diodes by means of sulfide treatment.

A diffraction grating with the period $a=0.826$ μm was created by holographic exposure of a photoresist to an Ar laser ($\lambda=0.488$ μm) on an n-GaAs wafer ($n_0=1\times10^{16}$ cm^{-3}). The sinusoidal profile was then transferred from the photoresist to the semiconductor substrate by chemical etching. The grating depth h was determined by measuring the intensity of the first diffraction order in s-polarized light and was 0.190 μm. An Ohmic contact was formed on the back of the wafer by alloying with indium. The Schottky diodes were prepared by vacuum evaporation of a gold film through a mask with $\sim$1 mm apertures. Sulfide passivation of the surface was accomplished by immersing the surface-barrier structures in a 2N aqueous solution of $Na_2S\cdot9H_2O$ for 20 s at room temperature under diffuse illumination. The samples were washed with distilled water and dried. The parameters of the Schottky barriers were determined from measurements of the current–voltage and rf capacitance-voltage characteristics, and from their photoemission. The spectral characteristics of the photocurrent were measured in the 0.3–1 μm wavelength range by using a DMR-4 monochromator, with a DKSSh-100 flashlamp at the entrance and a Glan prism at the exit. All the measurements were made using three types of preformed GaAs–Au structures: 1) initial structures, 2) sulfided structures after deposition of Au, and 3) structures

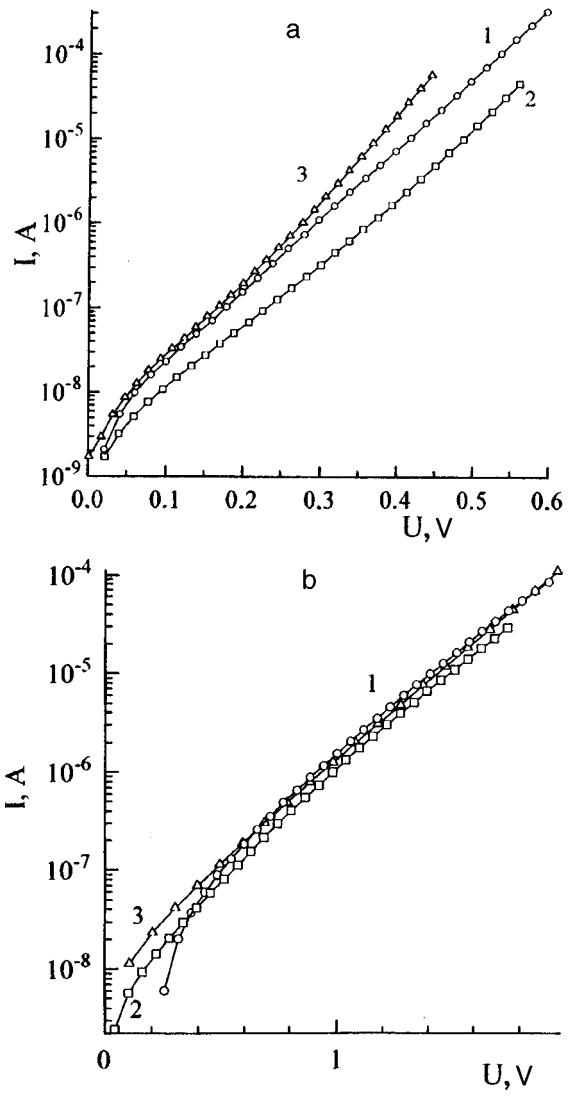

FIG. 1. Forward (a) and reverse (b) current–voltage characteristics of Au–GaAs surface-barrier structures before (*1*) and after (*2*) sulfide treatment, and after deposition of gold (*3*).

 1063-7850/97/050355-03$10.00

TABLE I. Influence of sulfide treatment on the parameters of surface-barrier structures.

Type of treatment	N diode	n (current–voltage characteristics)	Φ_B, V (current–voltage characteristics)	V_i, V (capacitance–voltage characteristics)	Φ_B, V (photo-emission)
GaAs–Au	1	3.79	0.645	1.945	0.99
	2	2.22	0.765	1.747	1.02
	3	1.7	0.724	1.602	1.016
	4	2.0	0.74	1.516	1.18
	5	1.98	0.72	1.487	0.989
GaAs–Au(S)	1	3.97	0.65	2.06	0.82
	4	2.13	0.763	1.516	–
	5	2.22	0.72	1.487	0.98
GaAs–Au(S)–Au	2	1.95	0.765	1.73	1.014
	3	1.69	0.755	0.99	0.99

formed by repeated (control) deposition of Au on sulfided Au electrodes.

Figures 1a and 1b give current–voltage characteristics before (curve *1*) and after (curve *2*) sulfiding, typical of several similar surface-barrier structures fabricated on the same GaAs wafer. The dark current on the forward current–voltage characteristics is considerably lower for the sulfided surface-barrier structures, whereas sulfiding has a weaker influence on the reverse current–voltage characteristics. The ideality factor (n) of the forward current–voltage characteristics and the barrier height are given in Table I for the three methods of determination.

It can be seen that the ideality factor n and the barrier height in the contact depend weakly on the sulfide treatment. The low values of Φ_B, obtained from the current–voltage characteristics for the initial GaAs–Au contact before sulfiding, can be attributed to the influence of the interface relief.[7] The decrease in the forward currents can be explained by the suppression of edge effects over the perimeter of the metal electrode[8] and by a reduction in the surface recombination velocity caused by the sulfide passivation.

Figures 2a and 2b show how sulfidation of the gate electrodes influences the photocurrent of GaAs–Au surface-barrier structures under conditions of excitation of surface polaritons. The photocurrent spectra in p-polarized light clearly show a polariton peak, which is not observed for s-polarized light and whose position shifts as a function of the angle of incidence of the light on the grating. Curve *2* in Fig. 2b demonstrates the change in the angular dependence of the sensitivity caused by sulfiding the preformed diodes. The observed shift of the peak on the angular dependence is caused by a change in the frequency of the surface polaritons propagating along the air–metal interface. Sulfide treatment not only shifts the resonance toward large wave vectors but also influences the distribution of the surface polaritons at the air–metal interface. This leads to changes in the conditions for re-emission of surface polaritons into a volume light wave, which slightly reduces the photocurrent. Weak absorption of light by the sulfide film also has a similar effect. The polarization sensitivity (the photocurrent ratio I_p/I_s at resonance) changes very little (or decreases negligibly), because all three conditions: 1) reduced recombination over the perimeter of the field electrode, 2) absorption of light, and 3)

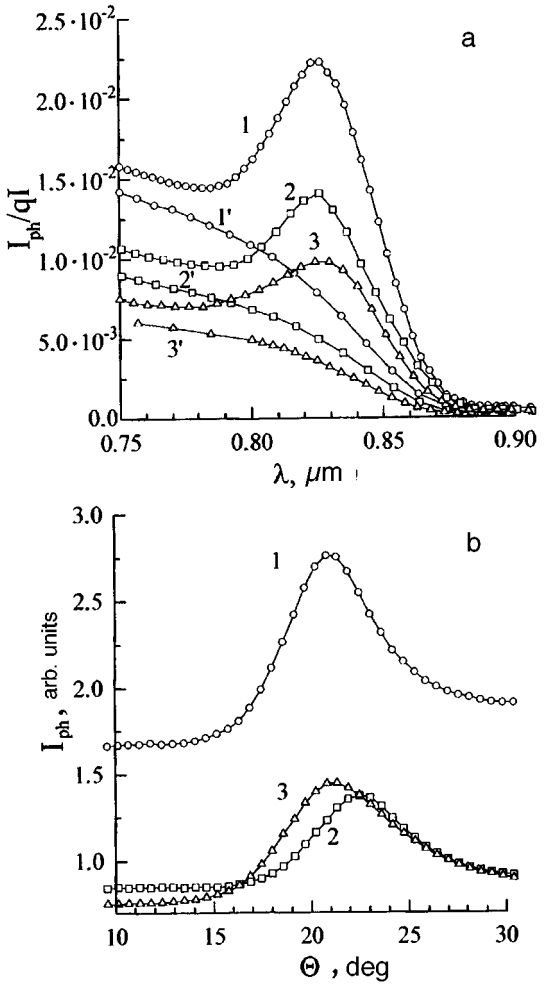

FIG. 2. a — Photocurrent spectra of Au–GaAs surface-barrier structures with a diffraction grating at the interface, measured with normally incident p-(*1*, *2*, *3*) and s-(*1′*, *2′*, *3′*) polarized light before (*1*, *1′*) and after (*2*, *2′*) sulfide treatment , and after repeated deposition of Au (*3*, *3′*). Gold thickness: *1*, *2* — 30 nm, *3* — 80 nm. b — Angular dependences of the photocurrent of Au–GaAs surface-barrier structures with a diffraction grating for p-polarized light ($\lambda = 0.6$ μm) before (*1*) and after (*2*) sulfide treatment, and after repeated deposition of Au (*3*).

changes in the intermediate layer at the metal–semiconductor interface induced by surface diffusion of S ions, have the same influence on the photosensitivity for both polarizations (Fig. 2a). Subsequent deposition (increase in the thickness of the gold layer) regularly broadens and shifts the photoresponse peak on the angular dependence (Fig. 2b, curve *3*). The slight heating (120 °C, 30 min) of the surface-barrier structures caused by the repeated deposition of Au, reduces the ideality n (the oxide becomes thicker), the barrier height tends to its initial value, and the forward currents even slightly exceed their initial values (Fig. 1a, curve *3*). Thus, the photoresponse characteristics under conditions of excitation of surface polaritons are mainly controlled by the air–metal interface, as is indicated by experiments involving the repeated deposition of gold.

The results of this investigation suggest that edge effects over the perimeter of the metal electrode, surface diffusion of sulfide ions, and passivation of the Au electrode all contribute to the change in the resonance and the photoresponse caused by sulfiding. The results of ellipsometric measurements indicate that the resonance shift (from $\Theta = 20.8°$ to 22°) and the change in its width and peak are attributed to a change in its imaginary part.

[1] S. R. J. Brueck, V. Diadiuk, T. Jones, and W. Lenth, Appl. Phys. Lett. **46**, 915 (1985).
[2] L. V. Belyakov, D. N. Goryachev, O. M. Sreseli, and I. D. Yaroshetskiĭ, Pis'ma Zh. Tekh. Fiz. **11**, 1162 (1985) [Sov. Tech. Phys. Lett. **11**, 481 (1985)].
[3] N. L. Dmitruk, V. G. Litovchenko, and V. L. Strizhevskiĭ, *Surface Polaritons in Semiconductors* [in Russian], Naukova Dumka, Kiev (1989).
[4] J. N. Wilde, M. C. Petty, S. Houghton *et al.*, *Abstracts of Papers presented at the 6th European Conference on Organised Films*, ECOF6, Sheffield, 1996, p. 31.
[5] M. S. Carpenter, M. R. Melloch, M. S. Lundstrom, and S. P. Tobin, Appl. Phys. Lett. **52**, 2157 (1988).
[6] E. V. Basyuk, N. D. Dmitryuk, and O. I. Maeva, Fiz. Tekh. Poluprovodn. **27**, 415 (1993) [Semiconductors **27**, 232 (1993)].
[7] O. Yu. Vorkovskaya, T. Ya. Gorbach, N. L. Dmitryuk, and O. N. Mishchuk, Fiz. Tekh. Poluprovodn. **23**, 2113 (1989) [Sov. Phys. Semicond. **23**, 1309 (1989)].
[8] E. H. Rhoderick, *Metal–Semiconductor Contacts* (Clarendon Press, Oxford, 1978) [Russ. transl., Radio i Svyaz', Moscow, 1982], p. 210.

Translated by R. M. Durham

Some features of the hydrodynamic characteristics of a high-voltage electric discharge in a liquid with a two-pulse power deposition law

A. I. Vovchenko, V. G. Kovalev, and V. A. Pozdeev

Institute of Pulse Processes and Technologies, National Academy of Sciences of Ukraine, Nikolaev
(Submitted November 28, 1996)
Pis'ma Zh. Tekh. Fiz. **23**, 58–61 (May 12, 1997)

An analysis is made of the external hydrodynamic problem of an underwater electric discharge with a two-pulse power deposition law in the channel. As a result of an analytic solution of the problem, it is shown that the pressure function at the channel wall is a series of pulses of decaying amplitude, while the pressure function for a fixed point in the wave field is a series of increasing pulses. © *1997 American Institute of Physics.* [S1063-7850(97)01005-7]

For an electric discharge in a liquid, the power deposition law usually has the form of a single pulse, and in the active stage of the process the radius of the plasma channel is described by a smooth increasing function of time, and the pressure in the channel has the form of a single pulse.[1] It was demonstrated theoretically in Refs. 2–4 that the power deposition law can be varied fairly widely by parametric variation of the discharge circuit characteristics, and pressure pulses of complex shape can thus be obtained. In Ref. 5, a power deposition law in the form of two pulses of increasing amplitude was achieved experimentally by switching off part of the effective resistance in the discharge circuit at a specific time. We shall show that in this case, the behavior of the pressure functions exhibits particular features.

We consider the external hydrodynamic problem of determining the pressure field in a compressible, ideal liquid during the expansion of a cylindrical plasma channel. The law governing the variation of the channel radius with time is described by a linearly increasing function with superposed pulsations of small amplitude and kinks at points corresponding to the kinks on the power deposition curve in the channel

$$R_n(t)=R_0+v_0t+R_1\cdot|\sin\,\omega_0t|, \tag{1}$$

where R_0 is the channel radius at time $t=0$, v_0 is the rate of linear increase in the radius, R_1 is the pulsation amplitude, and ω_0 is the angular frequency, which is related to the period of the pulsations by $\omega_0=\pi/T_0$. Since the maximum rate of expansion of the channel does not exceed 300 m/s, we use the linear wave equation to describe the dynamics of the liquid. However, the channel radius varies some tens of times, so that the kinematic boundary condition should be set at the instantaneous position of the moving channel boundary.[6] In accordance with this reasoning, the mathematical formulation of the problem is given by

$$\frac{\partial^2\phi}{\partial r^2}+\frac{1}{r}\frac{\partial\phi}{\partial r}-\frac{1}{c_0^2}\frac{\partial^2\phi}{\partial t^2}=0, \tag{2}$$

$$v=\frac{\partial\phi}{\partial r};\quad p=-\rho_0\frac{\partial\phi}{\partial t}, \tag{3}$$

$$v|_{r=R_p(t)}=v_p(t);\quad p|_{r=R_p(t)}p_p(t), \tag{4}$$

where ϕ is the velocity potential of the induced motion of the medium, r is the radial coordinate, c_0 is the unperturbed velocity of sound, ρ_0 is the unperturbed density of the medium, v and p are the velocity and pressure of the medium, and v_p and p_p are the corresponding parameters of the channel. In addition, the velocity potential should satisfy zero initial conditions and the radiation condition. Note that, because of the small pulse amplitude, in Eq. (4) we can assume

$$R_p(t)\simeq R_0+v_0t,$$

$$v_p(t)=v_0+v_1\cdot\cos\,\omega_0(t-t_i), \tag{5}$$

where t_i is the kink in the curve ($t_i=iT_0$, $i=0,1,2$), and $v_1=R_1\omega_0$.

Since an accurate solution of the wave equation (2) poses major mathematical difficulties, we use an approximation

$$\phi(r,t)=f(t^0)/r^{1/2}, \tag{6}$$

where t^0 is the wave argument ($t^0=t-(r-R_0)/c_0$). We solve the problem (1)–(6) by a nonlinear time transformation method,[7] which gives

$$\overline{p}_p(t)=\overline{v}_p(t)-\frac{1}{2R_p(t)}\cdot\exp\left[-\frac{c_0}{2}\int_0^t\frac{dr}{R_p(\tau)}\right]\times\int_0^t v_p(\tau)\left[1-\frac{1}{c_0}\frac{dR_p}{d\tau}\right]\cdot\exp\left[\frac{c_0}{2}\int_0^\tau\frac{d\tau_1}{R_p(\tau_1)}\right]d\tau, \tag{7}$$

where $\overline{p}_p=p_p/(\rho_0c_0^2)$ and $\overline{v}_p=v_p/c_0$. With allowance for Eq. (5), expression (7) becomes

$$\overline{p}_p(t)=\frac{3M_0^2}{1+2M_0}\left[1+\frac{1-M_0}{3M_0}\left(1+\frac{v_0t}{R_0}\right)^{-(1+1/2M_0)}\right]+M_1\left[\cos\omega_0(t-t_i)-\frac{(1-M_0)c_0}{2R_0\left(1+\frac{v_0t}{R_0}\right)^{(1+1/2M_0)}}\times\int_0^t\cos\omega_0(\tau-t_i)\left(1+\frac{v_0\tau}{R_0}\right)^{1/2M_0}d\tau\right], \tag{8}$$

 1063-7850/97/050358-02$10.00

where $M_0 = v_0/c_0$ and $M_1 = v_1/c_1$. In Eq. (8) the first term gives the contribution made by the linear increase in the channel radius and is a decreasing function of time, which reaches a constant value, the second terms has discontinuities, and the third terms exhibits kinks at points $t = t_i$. An additional analysis of the pressure function for the channel wall (8) indicates that this is a series of pulses of decaying amplitude.

We can easily show that in general, the correlation between the pressure function for the channel wall and the pressure function for a fixed point in the wave field is given by

$$p_{\mathrm{p}}(t) = \left[\frac{r}{R_{\mathrm{p}}(t)}\right]^{1/2} \cdot p\left(t - \frac{R_{\mathrm{p}}(t) - R_0}{c_0}\right). \tag{9}$$

For the specific kinematics of the channel described by Eq. (5), the correlation (9) has the form

$$p(t) = \left(\frac{R_0}{r}\right)^{1/2} \cdot \left[1 + \frac{v_0(1+M_0)}{R_0}\right]^{1/2} \cdot p_{\mathrm{p}}((1+M_0)t). \tag{10}$$

Expression (10) gives the correlation between the amplitudes and periods for the pressure function at a fixed point in the wave field with the coordinate r and the corresponding parameters of the pressure function for the channel wall (8). A joint analysis of expressions (8) and (10) yields the following conclusions:

- the pressure function for a cavity wall with $M_0 > M_1$ consists of a series of pulses of decaying amplitude;

- the pressure function for a fixed point in the wave field consists of a series of pulses of increasing amplitude;

- the pulsation period of the pressure curve for the channel wall is equal to the pulsation period T_0 of the power deposition curve, while the pulsation period of the pressure curve for a fixed point in the field is $T_1 = T_0/(1+M_0)$, i.e., the pulses undergo compression.

[1] K. A. Naugol'nikh and N. A. Roĭ, *Electric Discharges in Water* [in Russian], Nauka, Moscow (1971).
[2] A. V. Ivanov, A. I. Vovchenko, and O. A. Bogachenko, Tekh. Elektrodinam. No. 6, 15 (1981).
[3] V. V. Ivanov, Elektron. Obrab. Mater. No. 3, 30 (1982).
[4] A. I. Vovchenko, Tekh. Elektrodinam. No. 1, 12 (1983).
[5] A. I. Vovchenko, V. A. Pozdeev, and I. V. Shtompel', Tekh. Elektrodinam. No. 3, 16 (1985).
[6] V. A. Pozdeev, Akust. Zh. **41**, 164 (1995) [Acoust. Rep. **41**, (1995)].
[7] V. A. Pozdeev, Prikl. Mat. Mekh. No. 6, 1055 (1991).

Translated by R. M. Durham

Influence of local pressure on the current–voltage characteristic of Au–Si⟨Ni⟩–Sb structures

O. O. Mamatkarimov

Ulugbek State University, Tashkent
(Submitted December 12, 1996)
Pis'ma Zh. Tekh. Fiz. **23**, 62–64 (May 12, 1997)

Results of an investigation of the influence of local pressure on the current–voltage characteristic of Au–Si⟨Ni⟩–Sb structures are presented for the first time. It is shown that nickel impurities in the silicon increase the total strain sensitivity n-Si⟨Ni⟩ structures. © *1997 American Institute of Physics.* [S1063-7850(97)01105-1]

It was shown in Refs. 1 and 2 that semiconductors compensated with deep-level impurities are distinguished from other materials by a high strain sensitivity, which is increased as the degree of compensation is increased.

The present paper is therefore devoted to studying the strain properties of Schottky-barrier structures, fabricated using initial silicon and nickel-compensated silicon.

Samples of n-Si⟨Ni⟩ were prepared by high-temperature ($T=1050$–1100 °C) diffusion from a layer of metallic nickel deposited on the surface. The samples were $3\times3\times0.3$ mm rectangular parallelepipeds with the [111] crystallographic orientation along a short edge. After diffusion, n-Si⟨Ni⟩ samples with the initial resistivity $\rho=80\ \Omega\cdot$cm retained their type of conduction, and at diffusion temperatures $T_D=1100$ °C and $T_D=1130$ °C, their resistivity became $\rho=5\times10^2\ \Omega\cdot$cm and $\rho=3\times10^3\ \Omega\cdot$cm, respectively.

Schottky-barrier structures were prepared by evaporation of gold and antimony on the opposite large faces of the samples.

We developed a special apparatus, shown schematically in Fig. 1, to study the strain properties of the structure. A metal needle *9*, with a tip radius $R=40\ \mu$m is moved downward by means of springs *13*. When the needle has covered the distance Δx, the springs *12* are also compressed by the amount Δx and the sample is exposed to the force $F=k\Delta x$, or the pressure $P=\Pi F^{1/3}$, where

$$\Pi=\frac{1}{\pi(RD)^{2/3}} \quad \text{and} \quad D=\frac{3}{y}\left(\frac{1-\sigma^2}{y}-\frac{1-\sigma_1^2}{y'}\right),$$

σ and σ_1 are the Poisson ratios and y' and y are Young's moduli for the semiconductor and the needle material, respectively. The piston *11* and the guide cylinder ensure that

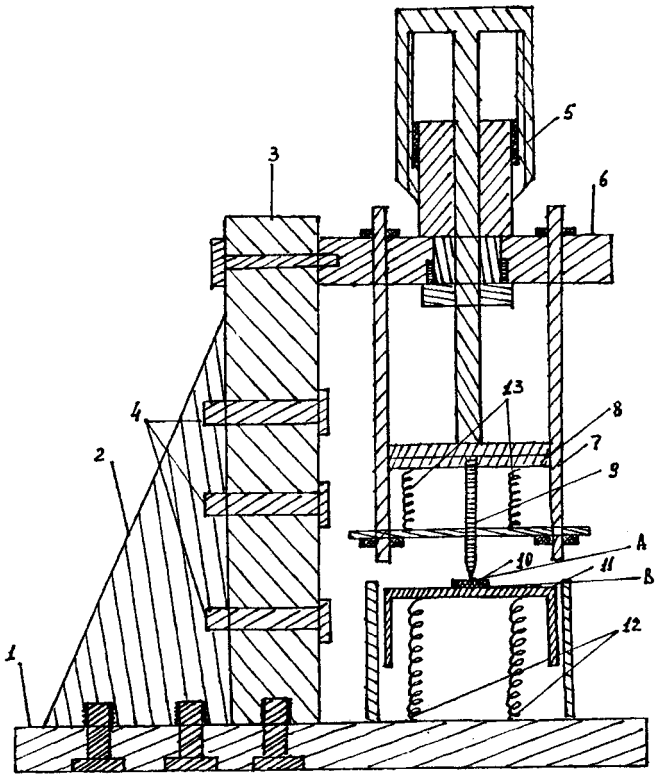

FIG. 1. Apparatus for application of local pressure.

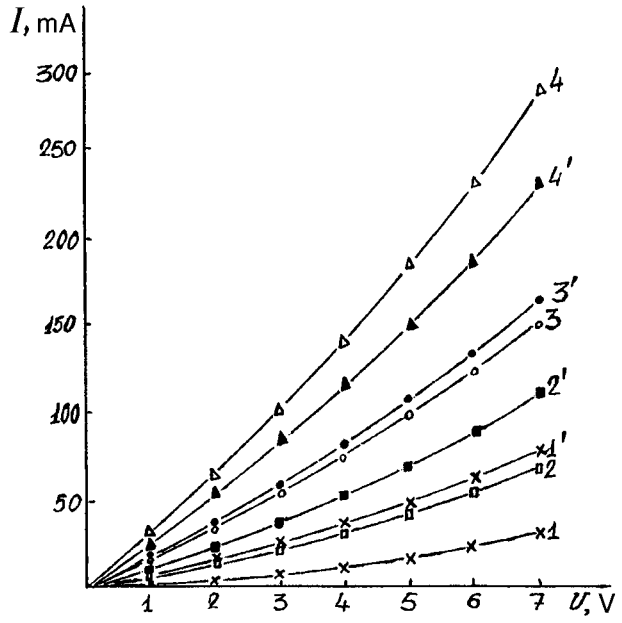

FIG. 2. Current–voltage characteristics of Schottky-barrier structures with $T=300$ K. Curves *1′–4′* correspond to the forward branches of the current–voltage characteristics of Au–⟨n-Si⟩–Sb structures and curves *1–4* give the current-voltage characteristics of Au–n-S⟨Ni⟩–Sb structures. *1, 1′* — $P=0$; *2, 2′* — $P=0.6\times10^8$ Pa; *3, 3′* — $P=1\times10^8$ Pa, and *4, 4′* — $P=1.6\times10^8$ Pa.

the sample is positioned perpendicular to the needle. Outputs A and B are used to record the current–voltage characteristics of the Schottky-barrier structures.

Figure 2 gives current–voltage characteristics of Schottky-barrier structures fabricated using initial silicon and nickel-compensated silicon. The figure shows that the forward current of the n-Si⟨Ni⟩ structures varies more strongly as a function of local pressure compared with the forward current of the initial-silicon structures.

It may be concluded from the experimental results that the nickel impurities in the silicon increase the total strain sensitivity of n-Si⟨Ni⟩ structures.

[1] A. Abduraimov, S. Z. Zaĭnabidinov, O. O. Mamatkarimov, and I. G. Tursunov, Uzbek. Fiz. Zh. No. 4, 68 (1992).
[2] A. Abduraimov, S. Z. Zaĭnabidinov, O. O. Mamatkarimov, Fiz. Tekh. Poluprovodn. **27**, 1216 (1993) [Semiconductors **27**, 671 (1993)].

Translated by R. M. Durham

Maximum input energy to gas-discharge active media

A. Yu. Sonin

Institute of General Physics, Russian Academy of Sciences, Moscow
(Submitted December 27, 1996)
Pis'ma Zh. Tekh. Fiz. **23**, 65–67 (May 12, 1997)

Fundamental relations are obtained to determine the conditions for utilization of a gas discharge as an active medium to develop lasers with the maximum efficiency. © *1997 American Institute of Physics.* [S1063-7850(97)01205-6]

The problem of efficient conversion of pump energy into laser radiation energy is extremely relevant for the development of high-efficiency compact laser systems.[1] The most widely used method of pumping large volumes of active medium is the electric discharge.

Let us consider the problem of depositing the discharge energy in the active medium. The input energy per particle can be written as:

$$\frac{W}{N}=\frac{P_\tau}{N}=\frac{en_k w_e E\tau}{N}=\frac{\hbar\omega}{\varphi}, \tag{1}$$

where W and P are the energy and power of the discharge pulse, τ is the time needed for transfer of the discharge energy to a given lasing transition, N is the particle density, $\hbar\omega$ and φ are the photon energy and the quantum efficiency of the active medium, e, n_k, and w_e are the electron charge, concentration, and drift velocity, and E is the electric field strength.

In self-sustained volume discharges, an upper limit is imposed on τ — the discharge formation time τ_f (Refs. 2 and 3), since this is the minimum lifetime of a discharge with given parameters N and E/N in the entire discharge volume:

$$\tau_f=[(\alpha-\eta)w_e]^{-1}\ln\left(\frac{n_k}{n_0}\right), \tag{2}$$

where n_0 is the initial electron concentration, and α and η are the coefficients of ionization and attachment.

According to Refs. 2 and 3, the following processes only take place during τ_f: transfer of energy from the supply source to the electrons, pumping of the lasing transition by these electrons, ionization of the gas, and redistribution of energy among electrons in the entire volume. Since 10^8 electron collisions take place in this time and $E/N=$ const in the entire discharge volume, we can talk of mean-statistical parameters. Note that the value of E/N determines both τ_f and the average electron energy, which, in the optimum case, should be close to the energy of a given upper laser level. After the time τ_f, the structure of the discharge undergoes rearrangement, the electric field becomes nonuniform over the length of the discharge volume, and in this case, relations (1) and (2) must be analyzed for different parts of the discharge volume.

Then, replacing τ in Eq. (1) with τ_f from Eq. (2), we obtain the maximum input energy and electron concentration:

$$W=en_k\left(\frac{E}{N}\right)\left(\frac{\alpha-\eta}{N}\right)^{-1}\ln\left(\frac{n_k}{n_0}\right), \tag{3}$$

$$\frac{n_k}{N}=\left(\frac{\hbar\omega}{\varphi}\right)\left(\frac{\alpha-\eta}{N}\right)\left[e\left(\frac{E}{N}\right)\ln\left(\frac{n_k}{n_0}\right)\right]^{-1}. \tag{4}$$

Thus, these expressions determine the maximum discharge parameters. For a given type of laser, the input energy can only be varied for a given parameter E/N by varying the electron concentration n_k, and it can be seen from Eqs. (3) and (4) that the initial electron concentration and the particle density play an important role. It follows from Eq. (4) that n_k/N depends only on E/N and this is confirmed by the results of Ref. 4. The parameter E/N should be determined from the equations for a discharge-excited laser active medium. These equations must be solved jointly with Eqs. (3) and (4). In addition, the discharge parameters must be such that the discharge energy is converted into the population inversion with the maximum efficiency.

For a self-limiting active medium, the rate equations for the inversion ΔN give:[5]

$$\Delta N=K_p\langle\sigma w\rangle n_k N\tau_p, \tag{5}$$

where K_p is a function determined by the values of τ_p and τ_f, $\langle\sigma w\rangle$ is the rate constant for excitation of the upper active level, and $\tau_p=\tau_0/1+(N/N_0)$ is the lifetime of this level, which is determined by the radiative lifetime τ_0 and the characteristic density N_0. Under optimum conditions, we find $\tau_p=\tau_f$ and $K_p=\max=\text{const}$. The condition for maximum inversion efficiency per electron is:

$$\frac{\partial}{\partial N}\left(\frac{\Delta N}{n_k}\right)=\frac{\partial}{\partial N}(\langle\sigma w\rangle N\tau_p)=0. \tag{6}$$

With allowance for the dependence of τ_p on the density of the gas mixture components and the equality $\tau_p=\tau_f$, we then obtain:

$$\frac{\partial\ \ln\langle\sigma w\rangle}{\partial\ \ln(E/N)}=\frac{\tau_p}{\tau_0}=\frac{\tau_f N}{\tau_0 N}. \tag{7}$$

The first equality in this system determines the particular optima for various field strengths E and densities N, and both equalities give the absolute maximum. Using graphs of

$\ln\langle\sigma w\rangle = f(E/N)$, $\tau_f N = f(E/N)$, and $\tau_p = f(N)$, we can find the optimum values of $(E/N)_{\text{opt}}$ and N_{opt} which would give $\tau_f = \tau_p$ and, at this point, the derivative $\partial \ln\langle\sigma w\rangle / \partial \ln(E/N)$ would be equal to (τ_p/τ_0). This value of $(E/N)_{\text{opt}}$, substituted into Eqs. (3) and (4), would determine the maximum input energy. Thus, optimum conditions exist for the conversion of discharge electron energy into stimulated emission energy utilizing self-terminating transitions, and these conditions also determine the maximum input energy.

[1] V. P. Gorkovskiĭ, N. V. Karlov, I. O. Kovalev *et al.*, Kvantovaya Elektron. (Moscow) **11**, 1867 (1984) [Sov. J. Quantum Electron. **14**, 1253 (1984)].
[2] H. Raether, *Electron Avalanches and Breakdown in Gases* (Butterworths, London, 1964) [Russ. transl., Mir, Moscow, 1968].
[3] V. V. Korobkin and A. Yu. Sonin, Pis'ma Zh. Tekh. Fiz. **19**(21), 49 (1993) [Tech. Phys. Lett. **23**, 686 (1993)].
[4] L. J. Denes and J. J. Lowke, Appl. Phys. Lett. **23**, 130 (1973).
[5] A. Yu. Sonin, Abstracts of Papers presented at Second Conf., NUTs, Patrice Lumumba Friendship of Nations University, Moscow, 1989 [in Russian], p. 103.

Translated by R. M. Durham

Superluminescence in an AlGaAsSb/InGaAsSb/AlGaAsSb double heterostructure

K. D. Moiseev, M. P. Mikhaĭlova, O. V. Andreĭchuk, B. E. Samorukov, and Yu. P. Yakovlev

A. F. Ioffe Physicotechnical Institute, Russian Academy of Sciences, St. Petersburg
(Submitted February 5, 1997)
Pis'ma Zh. Tekh. Fiz. **23**, 68–74 (May 12, 1997)

Intense electroluminescence is observed for the first time in a AlGaAsSb/$In_{0.9}Ga_{0.1}As_{0.89}Sb_{0.21}$/AlGaAsSb double heterostructure in the $3-4$ μm wavelength range at $T=77$ K. The structure was grown on a GaSb substrate by liquid-phase epitaxy. The photon energy at the maximum of the narrow emission band with a half-width of 9–10 eV is $h\nu=387$ meV which is 60 meV greater than the band gap of the narrow-gap InGaAsSb solid solution ($E_g=326$ meV). This behavior is attributed to the population inversion characteristics of the active region when an external bias is applied [S1063-7850(97)01305-0]

The development of middle-infrared (3–4 μm) lasers utilizing III–V compounds has recently attracted growing interest.[1–4] This interest has been stimulated by the extensive scope for using these devices for diode laser spectroscopy and ecological monitoring.[5] These applications require lasers operating at room temperature. So far, the maximum operating temperature of infrared lasers fabricated using InAs solid solutions by various methods (liquid-phase and molecular beam epitaxy and growth from metalorganic compounds) and emitting in the 3–4 μm wavelength range, has not exceeded 180–200 K with pulsed pumping and 110 K with cw pumping.[1,2,4] The main factors limiting the operation of long-wavelength lasers at room temperature are nonradiative Auger recombination and carrier leakage across the heteroboundary as a result of poor electron and hole confinement. Thus, attempts have been made to increase the barrier height in the conduction band at the heteroboundary with the active medium by using confining layers of wide-gap AlAsSb solid solutions, grown by molecular beam epitaxy.[6]

In the present paper, we report for the first time the observation of electroluminescence in the 3–4 μm wavelength range in an AlGaAsSb/$In_{0.9}Ga_{0.1}As_{0.89}Sb_{0.21}$/AlGaAsSb double heterostructure grown by liquid-phase epitaxy.

The double heterostructure was grown on a p-GaSb(100) substrate. The active layer was a narrow-gap $In_{0.9}Ga_{0.1}As_{0.89}Sb_{0.21}$ solid solution with a high indium arsenide content, and the coating layers were formed by a $Al_{0.34}Ga_{0.66}As_{0.03}Sb_{0.97}$ solid solution, which provides good electron confinement for the carriers because of a large offset in the conduction band with a narrow-gap InGaAsSb layer in the active region ($\Delta E_c\sim 1.0$ eV). It should be noted that this structure was grown by liquid-phase epitaxy for the first time. Up till now, the growth of narrow-gap solid solutions on wide-gap layers with high Al and Ga contents by liquid-phase epitaxy has presented considerable difficulty because of the complexity of matching the two materials. Epitaxial layers formed by a double heterostructure, consisting of solid solutions whose compositions have the same lattice period as the GaSb substrate and are enriched in InAs and AlSb, have abruptly differing physical constants. This particularly applies to the coefficients of thermal expansion. Our estimates indicate that the coefficient of thermal expansion for solid solutions enriched in GaSb is almost twice that for solid solutions enriched in InAs. Second, the unlimited solubility of GaSb in indium-enriched melts makes it impossible to correct and refine the equilibrium phase diagrams by the method of source saturation to select In(Ga)AsSb solid solutions with a high InAs content, having the same lattice period as the GaSb.

The narrow-gap quaternary solid solution $In_{0.9}Ga_{0.1}As_{0.89}Sb_{0.21}$ was chosen because it is easier to grow on a GaSb substrate, compared with solid solutions containing no gallium (such as $InAs_{0.9}Sb_{0.1}$). By using a method of calculating the phase diagrams proposed in Ref. 7, we succeeded in overcoming these difficulties and obtained layers of $In_{1-x}Ga_xAs_{1-y}Sb_y$ solid solution, for which the lattice mismatch did not exceed 2.5×10^{-3} at $T=300$ K in the composition range $0.01<x<0.1$, $y=x+0.12$. The lattice mismatch of the confining $Al_{0.34}Ga_{0.66}As_{0.03}Sb_{0.97}$ layers and the GaSb substrate was around $\Delta a/a\sim(4-8)\times 10^{-4}$ ($T=300$ K). The thicknesses of the epitaxial layers were 0.8–1.2 μm for the $In_{0.9}Ga_{0.1}As_{0.89}Sb_{0.21}$ solid solution and 2.5 μm for the $Al_{0.34}Ga_{0.66}As_{0.03}Sb_{0.97}$ solid solutions. The carrier concentrations in the confining layers were of the order $n,p\sim 5\times 10^{16}$ cm^{-3} and in the undoped n-$In_{0.9}Ga_{0.1}As_{0.89}Sb_{0.21}$ layer, the electron concentration was 1×10^{17} cm^{-3} at $T=77$ K. The structure is shown schematically in Fig. 1. The band gap of the narrow-gap solid solution, according to the photoluminescence data, was $E_g=326$ meV ($T=77$ K).

Stripe laser structures with a stripe width of 60–90 μm and a cavity length $L=300$–500 μm were prepared by a standard photolithographic technique. Ohmic contacts to the p and n layers were prepared by deposition from Au/Zn and Au/Te alloys, respectively, followed by brazing in a hydrogen atmosphere. The electroluminescence was investigated at $T=77$ K using an MDR-4, 300 lines/mm, grating monochromator by a synchronous detection technique. The signal was recorded with a detector using a liquid-nitrogen-cooled InSb photoresistor. The measurements were made in the pulsed mode with pulse length $\tau=2.5$ μs and repetition frequency $f=10^5$ Hz.

The p-AlGaAsSb/n-InGaAsSb/n-AlGaAsSb structures

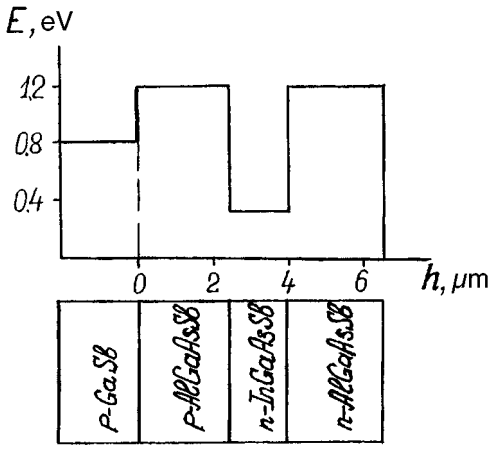

FIG. 1. Layer diagram of p-AlGaAsSb/n-InGaAsSb/p-AlGaAsSb double heterostructure isoperiodic with the GaSb substrate.

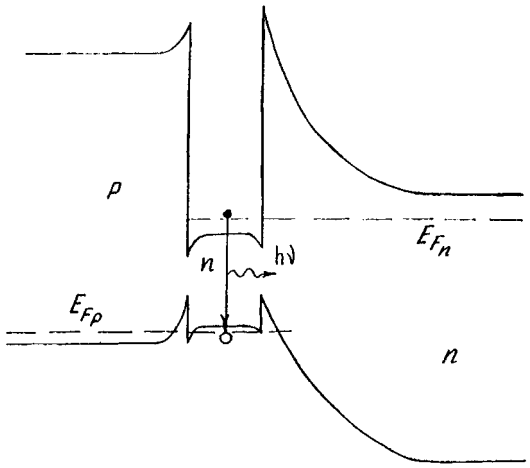

FIG. 3. Schematic of energy band diagram of a forward-biased p-AlGaAsSb/n-InGaAsSb/p-AlGaAsSb double heterostructure at $T=77$ K.

exhibited intense luminescence in the 3–4 μm wavelength range (Fig. 2). The electroluminescence spectra consisted of a single narrow band with a photon energy $h\nu=387$ meV at the emission maximum. The width of the emission peak at half height was $\Delta h\nu=9-10$ meV. The profile of the observed emission band was asymmetric and had a sharp edge on the high photon energy side. The electroluminescence intensity in these double heterostructures was comparable with the intensity at the lasing threshold of an ordinary diode laser utilizing indium arsenide solid solutions, emitting in the same wavelength range.

We note some features of the experimentally observed emission. This emission occurred when a forward bias was applied to the sample above a certain threshold $U>0.8$ V. The maximum of the emission band was 60 MeV greater than the band gap of the narrow-gap $In_{0.9}Ga_{0.1}As_{0.79}Sb_{0.2}$ solid solution ($Eg=326$ meV at $T=77$ K), but was much smaller than the band gap of the wide-gap $Al_{0.34}GaAs_{0.03}Sb$ confining layers ($Eg=1.214$ eV at $T=77$ K). It should be particularly stressed that the electroluminescence of these samples was only observed for long pump current pulses ($\tau=2.5$ ms) and did not occur with shorter pulses.

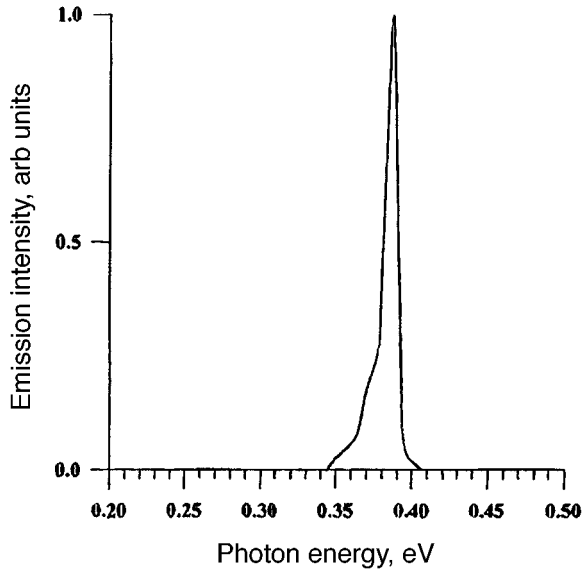

FIG. 2. Electroluminescence spectrum of a forward-biased p-AlGaAsSb/n-InGaAsSb/p-AlGaAsSb double heterostructure at $T=77$ K.

To explain these experimental results, we consider the energy band diagram of this double heterostructure under the application of a forward bias, shown schematically in Fig. 3. It can be seen that a potential barrier for the electrons exists at the heteroboundary between the n-active layer and the p-coating layer. A high potential barrier for the electrons also exists between the active layer and the n-type coating layer as a result of the large conduction band offset for the $Al_{0.34}Ga_{0.66}As_{0.03}Sb_{0.97}$ and $In_{0.9}Ga_{0.1}As_{0.89}Sb_{0.21}$ solid solutions. This offset increases the switching voltage and the series resistance of the entire structure because of the formation of an $n-n$ heteroboundary. A space-charge depletion region is formed on the wide-gap semiconductor side, while an n^+ accumulation layer is formed on the narrow-gap side. However, the high built-in potential at the $n-n$ heteroboundary confines the holes in the active layer of the double heterostructure.

When the bias voltage is increased by injection of carriers from the p and n emitter regions of the p-AlGaAsSb/n-InGaAsSb/n-AlGaAsSb double heterostructure, an efficient population inversion is created in the active region. In this case, the quasi-Fermi levels for the electrons and holes are located in the conduction band and in the valence band of the narrow-gap layer. This energy band diagram explains why the observed photon energy at the maximum of the emission band is greater than the band gap of the InGaAsSb solid solution.

In our case, an increase in the pump current density across the sample did not lead to further narrowing of the emission band and the establishment of coherence. In our view, this is attributable to the inadequate optical confinement in the structure. By using additional wide-gap confining layers, such as GaSb or GaInAsSb, it may be possible to achieve better wave confinement and obtain coherent long-wavelength emission in this structure.

To sum up, an isoperiodic p-AlGaAsSb/n-InGaAsSb/

n-AlGaAsSb double heterostructure on a GaSb substrate with good electron confinement has been fabricated by liquid-phase epitaxy and the first results have been obtained. Superluminescence has been achieved in this heterostructure and its electroluminescence properties have been studied. The potential for developing lasers for the 3–4 μm spectral range has been demonstrated.

The authors would like to thank A. M. Monakhov for useful discussions.

This work was partially supported under the Program of the Russian Ministry of Science entitled ''Physics of Solid-State Nanostructures,'' Project No. 1-077/4, and also by the U.S. European Office of Aerospace Research and Development (US EOARD), Contract No. F61708-96-W0078.

[1] H. K. Choi, S. J. Eglash, and G. W. Turner, Appl. Phys. Lett. **64**, 812 (1994).
[2] T. N. Danilova, O. G. Ershov, A. N. Imenkov, M. V. Stepanov, V. V. Sherstnev, and Yu. P. Yakovlev, Fiz. Tekh. Poluprovodn. **30**, 1265 (1995) [Semiconductors **30**, 667 (1995)].
[3] T. C. Hasenberg, A. Cost, R. Miles *et al.*, Electron. Lett. **31**, 275 (1995).
[4] Yu. P. Yakovlev, K. D. Moiseev, M. P. Mikhailova, O. G. Ershov, and G. G. Zegrya, *Technical Digest of Papers presented at CLEO-96*, Anaheim, 1996, pp. 170–171.
[5] A. Nadezhdinski and A. M. Prokhorov, Proc. SPIE **1724**, 2 (1992).
[6] H. K. Choi, G. W. Turner, and Z. L. Liau, Appl. Phys. Lett. **65**, 2251 (1994).
[7] A. N. Baranov, A. M. Litvak, K. D. Moiseev, V. V. Sherstnev, and Yu. P. Yakovlev, Zh. Prikl. Khim. **67**, 1956 (1994).

Translated by R. M. Durham

Analytic relations between the parameters of a high-voltage discharge channel plasma in a liquid and a plasma jet in an evacuated chamber

V. A. Pozdeev

Institute of Pulse Processes and Technologies, National Academy of Sciences of Ukraine, Nikolaev
(Submitted December 31, 1996)
Pis'ma Zh. Tekh. Fiz. **23**, 75–78 (May 12, 1997)

Analytic relations are derived between the parameters of a high-voltage electric discharge plasma in a liquid and the parameters of a plasma jet in an evacuated chamber. These relations can be used to calculate the plasma temperature and pressure in the axial zone of the discharge channel by using the experimentally measured temperature of the plasma jet and its geometric characteristics. © *1997 American Institute of Physics.* [S1063-7850(97)01405-5]

One of the fundamental problems in the physics of a high-voltage electric-discharge plasma in a liquid involves determining the distribution of the plasma parameters over the channel radius. It may be considered that heating of the surface layer of the channel plasma has been fairly well studied experimentally and the results obtained by various researchers show good agreement. The temperature of the internal region of the discharge channel was first estimated experimentally by an original method in Ref. 1 and the experimental results were discussed in Ref. 2. The experimental method essentially involves measuring the temperature of a plasma jet emitted through an aperture in a planar electrode positioned along the axis of the channel. It was established experimentally that the temperature of the jet is higher than that at the channel surface. However, the authors of Refs. 1 and 2 did not estimate the difference between the temperature of the channel plasma and the temperature of the jet plasma. In Ref. 3, the present author analyzed a mathematical model of a method for diagnostics of the plasma temperature in the inner region of a discharge channel, which was proposed in Ref. 1.

As in Ref. 3, we make the following assumptions to derive analytic relations between the parameters of the channel plasma and the jet parameters. We assume that the plasma is an ideal gas from the gasdynamic and thermodynamic viewpoints. Throughout the measurements, we assume that the parameters of the channel plasma (pressure p_1, density ρ_1, and temperature T_1) and the parameters of the jet plasma (density p_2, pressure ρ_2, and temperature T_2) are constant or slowly varying quantities. These assumptions allow us to use the following well-known thermodynamic relations[4]

$$p_i=\rho_i R T_i, \quad i=1, 2; \tag{1}$$

$$p_2/p_1=(\rho_2/\rho_1)^{\gamma}, \tag{2}$$

where R is the gas constant and γ is the effective adiabatic exponent of the plasma. Assuming that the flow of plasma through the aperture into the evacuated chamber is steady-state, we use the following well-known gasdynamic relation[4]

$$\frac{p_2}{p_1}=\left(1-\frac{\gamma-1}{2\gamma}\frac{\rho_1}{p_1}u^2\right)^{\frac{\gamma}{\gamma-1}}, \tag{3}$$

where u is the axial rate of plasma flow from the aperture on the chamber side.

Assuming that the temperature of the plasma jet T_2 and the rate of plasma flow u through the aperture are known, we use expressions (1)–(3) to derive the required relations between the parameters of the channel plasma and the jet plasma

$$\frac{p_1}{p_2}=\left(1+\frac{\gamma-1}{2\gamma}\frac{u^2}{RT_2}\right)^{\frac{\gamma}{\gamma-1}}, \tag{4}$$

$$\frac{T_1}{T_2}=\left(1+\frac{\gamma-1}{2\gamma}\frac{u^2}{RT_2}\right)^{-1}. \tag{5}$$

It was shown in Refs. 1 and 2 that the temperature of the jet plasma may be directly measured experimentally. We find the plasma flow rate as follows from the condition that the plasma flow rate through the aperture is equal to the change in plasma mass in the volume of the jet, assuming constant density

$$u\simeq\frac{1}{f}\frac{dV}{dt}, \tag{6}$$

where f is the area of the aperture ($f=\pi y_0^2$), y_0 is the aperture radius, and V is the volume of the plasma jet. Considering the jet to be a solid of revolution with the generatrix $y(x)$, we obtain the volume of the jet as the integral

$$V=2\pi\int_0^l y^2(x)dx, \tag{7}$$

where l is the instantaneous length of the jet and x is the axial coordinate.

We use the following specific expression for the function $y(x)$

$$y(x)=a\left(1-\frac{x}{l}\right)^{1/2}-b\left(1-\frac{x}{l}\right), \tag{8}$$

where a and b are constants determined from the conditions:

$$y|_{x=0}=y_0, \quad \left.\frac{dy}{dx}\right|_{x=0}=y_0'. \tag{9}$$

Using the conditions (9), formula (8) then yields

$$a=2y_0'l+2y_0, \quad b=2y_0'l+y_0. \tag{10}$$

 1063-7850/97/050367-02$10.00

Substituting the expression for the generatrix (8) into expression (7), using formula (10), we obtain

$$V=\frac{22}{15}\left(1+\frac{8}{11}\beta+\frac{2}{11}\beta^2\right)l, \tag{11}$$

where $\beta=y_0'l/y_0$. Now, in accordance with formula (6) and using Eq. (11), we obtain the following expression for the plasma flow rate

$$u=1.46(1+1.46\beta+0.546\beta^2)\frac{dl}{dt}. \tag{12}$$

For a highly elongated jet ($\beta\to D$), expression (12) yields the estimated flow rate

$$u\simeq 1.46\cdot\frac{dl}{dt}. \tag{13}$$

For critical plasma flow, the flow rate becomes equal to the velocity of sound[4]

$$u=c=\left(\frac{2\gamma}{\gamma+1}RT_2\right)^{1/2}. \tag{14}$$

The relations for the parameters of the channel plasma and the jet plasma (4) can then be simplified to give

$$\frac{p_1}{p_2}=\left(\frac{\gamma+1}{2}\right)^{\frac{\gamma}{\gamma-1}},\quad \frac{T_1}{T_2}=\left(\frac{\gamma+1}{2}\right). \tag{15}$$

For $\gamma=1.25$ we obtain the following quantitative values from the relations (15): $T_2/T_1=0.89$, and $p_2/p_1=0.56$.

To sum up, the proposed mathematical model of plasma flow through an aperture into an evacuated chamber can be used to determine the plasma pressure and temperature in the axial region of the discharge channel, using the measured jet temperature and geometric characteristics in the general case and using only the measured temperature for critical flow. These analytic relations are simple and convenient for practical application.

The results presented here emphasize the difference between the plasma temperature in the axial region of the channel and the plasma in the surface layer, for which values were quoted in Refs. 1 and 2.

[1] L. L. Pasechnik, P. L. Starchik, O. A. Fedorovich, and L. Yu. Popov, *The Electric Discharge and Its Application in Industry* [in Russian], Naukova Dumka, Kiev (1980), pp. 12–13.

[2] V. M. Adamyan, G. A. Gulyĭ, N. L. Pushek, P. D. Starchik, I. M. Tkachenko, and I. S. Shvets, Teplofiz. Vys. Temp. **18**, 230 (1980).

[3] V. A. Pozdeev, *Theoretical Principles of Hydrodynamics in the Experimental Diagnostics of Plasma Pressure in a High-Voltage Electric Discharge Channel in a Liquid* [in Russian], Educational Equipment, Institute of Pulse Processes and Technologies, National Academy of Sciences of Ukraine, Nikolaev (1996).

[4] I. P. Ginzburg, *Aerodynamics* [in Russian], Vysshaya Shkola, Moscow (1966).

Translated by R. M. Durham

Carrier transport in a diode base with locally nonuniform recombination properties

A. M. Ivanov, N. B. Strokan, and V. B. Shuman

A. F. Ioffe Physicotechnical Institute, Russian Academy of Sciences, St. Petersburg
(Submitted February 5, 1997)
Pis'ma Zh. Tekh. Fiz. **23**, 79–86 (May 12, 1997)

Nonuniformity of the recombination properties in the form of a layer of radiation defects is created in the base of a p^+-n diode. The change in the effective hole lifetime, measured by an injection-extraction method, is investigated and attributed to recombination in this layer.
 [S1063-7850(97)01505-X]

We consider a reverse-biased p^+-n diode, where transport of the charge of nonequilibrium holes, injected by various methods, is observed in the diode base. These injection methods include preliminary passage of a forward current or pulsed ionization by nuclear particles. We investigate how the charge flows across the plane of the p^+-n junction when the uniformity of the recombination properties is locally impaired. In our experiments, the nonuniformity is represented geometrically by a layer of a certain thickness δ.

1. The process of forward-to-reverse switching of this type of diode has been investigated in detail in the literature (see, for example, Ref. 1). A description of the reverse current profile with a characteristic ''shoulder'' (see the inset in Fig. 1) was obtained, and the duration T of this shoulder was related to the lifetime τ by

$$\mathrm{erf}(T/\tau)^{1/2}=I_{\mathrm{for}}/(I_{\mathrm{for}}+I_{\mathrm{rev}}), \tag{1}$$

where I_{for} and I_{rev} are the forward and reverse currents, respectively. The relation (1) obtained back in the 1960s forms the basis of the now classical method of determining the lifetime τ in p^+-n structures.

Since the value of $T(\tau)$ determines the response time for recovery of the resistance of the reverse branch of the diode, measures were taken to reduce the lifetime τ. Fundamental research in this direction[2,3] involved uniformly reducing the lifetime τ in the diode base by introducing deep levels, particularly with penetrating β- and γ-radiation. An alternative to uniformly reducing τ involves irradiation by short-range particles — protons and α-particles. For example, for ≈ 5 MeV natural-decay α particles, all the primary defects may be considered to be concentrated in a narrow layer at the end of the particle range. This result is obtained by mathematical modeling of the stopping of an α-particle for primary vacancies and interstitial atoms.[4,5]

During the subsequent migration of defects and the formation of complexes with impurities, the initial distribution changes negligibly. This was established by direct determination of the defect profile by deep level transient spectroscopy (DLTS).[5,6] Accordingly, when the diodes are irradiated by a collimated beam, the introduced recombination centers are distributed in a narrow layer δ, comparable with the particle range, i.e., they have an extremely nonuniform distribution over the volume of the base.

In our experiments we used 5.25 MeV α particles with the range $R=25.7$ μm. The irradiated diodes were made of Si, having a 350 μm thick n-base with a phosphorus concentration of 1.2×10^{14} cm^{-3}, and a 1.7 μm thick diffused p^+-layer, with a boron surface concentration of $\cong 10^{20}$ cm^{-3}. The initial lifetime in the diodes was $\tau_0\cong 20$ μs. All the experiments were carried out at room temperature. The diodes were exposed to low-dose irradiation, the dose being monitored by the p^+-n structure itself, for which the diode was used in detector mode. The behavior of the lifetime τ measured by this method (see formula (1)) was observed. Forward current densities of $\cong 300$ mA/cm^2 were used for the measurements.

As is the normal procedure in this type of experiment, the value $1/\tau=1/\tau_{\mathrm{meas}}-1/\tau_0$ is analyzed, where τ_{meas} and τ_0 are the measured and initial lifetimes, respectively. Under electron and γ-irradiation, $1/\tau$ is proportional to the dose Φ. However, the observed behavior exhibited strong nonlinearity and then reached saturation (Fig. 1). An analysis of the $1/\tau$ measurements indicates that for α-particle doses in the range $\Phi=(5\times10^8-10^{10}$ cm^{-2}, the behavior of $1/\tau(\Phi)$ is nearly quadratic.

To explain this behavior of $1/\tau$, it is logical to make the following assumption. Under conditions of nonuniform defect injection, the effective lifetime rather than the actual value of τ in the base is determined from the duration of the shoulder in the reverse current section. Note that formula (1) corresponds to the case of a base much longer than the diffusion length $L_D=(D\tau)^{1/2}$, where the hole diffusion coefficient in silicon is $D=11.6$ cm^2/s. For initial values of $\tau_0\cong 20$ μs, we have $L_D\approx 150$ μm and so formula (1) is valid. As defects are injected in the base to a depth $\cong 25$ μm, a layer with reduced τ begins to be formed. Each α particle creates a damage zone in the form of a cone which expands toward the end of the range. Its base area is of the order of 10^{-8} cm^2, so that defects induced by separate particles begin to overlap at doses $\geqslant 10^8$ cm^{-2}. It may be assumed that in our dose range $\Phi\geqslant 2\times10^9$ cm^{-2}, the defects form a layer with the average density $M=k\Phi/\delta$, where k is the number of Frenkel pairs per α-particle which have not recombined in the track and have formed a deep center in the layer, and δ is the width of the layer. Assuming $k=2$ (Ref. 7) and $\delta=5$ μm (Ref. 5), we have $M=1\times10^{13}$ cm^{-3} for a dose of 2.5×10^9 cm^{-2}.

A layer with these characteristics does not satisfy the conditions of the initial model because a sink for holes is created near the p^+-n junction, at a distance $W\gg L_D$. In the limit, the δ layer may be considered to be a plane with a surface recombination velocity $S\to\infty$. This reduces the situ-

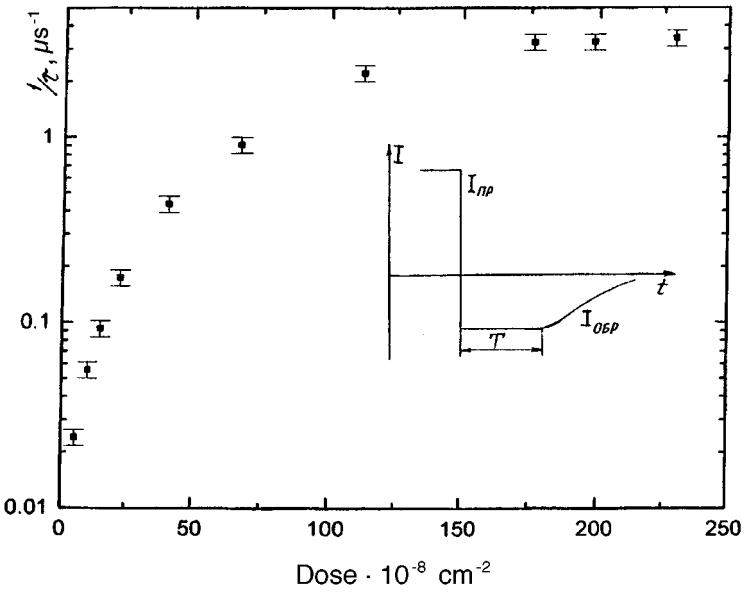

FIG. 1. Reciprocal hole lifetime in diode base versus α-particle irradiation dose. The measurements were made by the injection-extraction method (see formula (1)). The forward current density is 0.3 A/cm^2. Inset— typical current profile in diode circuit when switching from forward (I_{for}) to reverse (I_{rev}) bias.

ation to the case of a ''thin'' diode with a recombination type of rear contact. A solution of this problem may be found in Ref. 8. An approximate formula relating the shoulder duration and the layer depth W was put forward in Ref. 1:

$$T \cong \ln[0.8(1+I_{\text{for}}/I_{\text{rev}})]W^2/(2.5\ D). \qquad (2)$$

For our measurements, this implies that $1/\tau = f(\Phi)$ should reach saturation. This will correspond to the time taken for τ to decrease to the level, described formally as $S=\infty$ in the δ layer.

Saturation was in fact clearly observed in the dose range $\Phi \approx 2\times10^{10}$ cm^{-2} (Fig. 1). For this case, the lifetime τ in the layer may be estimated as $\tau=(V_{\text{th}}\sigma M)^{-1}$. Assuming that the thermal velocity is $V_{\text{th}}=3\times10^7$ cm/s and the trapping cross section is $\sigma=3\times10^{-15}$ cm^2, we obtain $\tau\approx1.4\times10^{-7}$ s. This difference of two orders of magnitude from the initial value (which remains unchanged in the main, undamaged, part of the base) is sufficient for an intense hole sink in the damaged layer. This is confirmed by a quantitative estimate. Substituting the shoulder duration $T=0.2$ μs into expression (2), we obtain $W=22.3$ μm, which agrees well with the position of the layer center $R-\delta/2=25.7-2.5=23.2$ μm.

2. We needed to determine whether the strong dependence $1/\tau(\Phi)$ was related to the characteristics of the defect spectrum, such as the concentration and capture cross section of the formed centers. For this purpose, we made DLTS measurements, and Fig. 2 shows the DLTS spectrum of a sample irradiated with an α-particle dose of 1.4×10^9 cm^{-2}. In the upper half of the band gap we can identify four levels from the general complexity. First, we can identify an E1-A-center ($E_c-0.18$ eV, $\sigma_n=2\times10^{-14}$ cm^2). This is followed by the E2 level ($E_c-0.22$ eV, $\sigma_n=2\times10^{-16}$ cm^2), which is assigned to a doubly negatively charged divacancy state. Then we can identify the E3 peak ($E_c-0.29$ eV, $\sigma_n=2\times10^{-17}$ cm^2), assigned to an interstitial carbon-phosphorus pair, and finally, the E4 peak ($E_c-0.4$ eV, $\sigma_n=2\times10^{-16}$ cm^2), for which at least two centers are responsible: an E-center (vacancy-phosphorus) and a divacancy (singly negative charged state). In the lower half of the band gap, studied in the hole injection regime, we can only clearly identify an interstitial-carbon–interstitial-oxygen, C_i–O_i, center (H2$=E_v+0.4$ eV, $\sigma_p=3\times10^{-14}$ cm^2).

The observed levels are typical of n-Si. Note the negligible presence of the H1 center ($E_v+0.33$ eV, $\sigma_p=9\times10^{-14}$ cm^2 (Ref. 9)), which is assigned to single interstitial carbon and is characteristic of pure Si. This behavior may be attributed to binding of C_i and O_i during

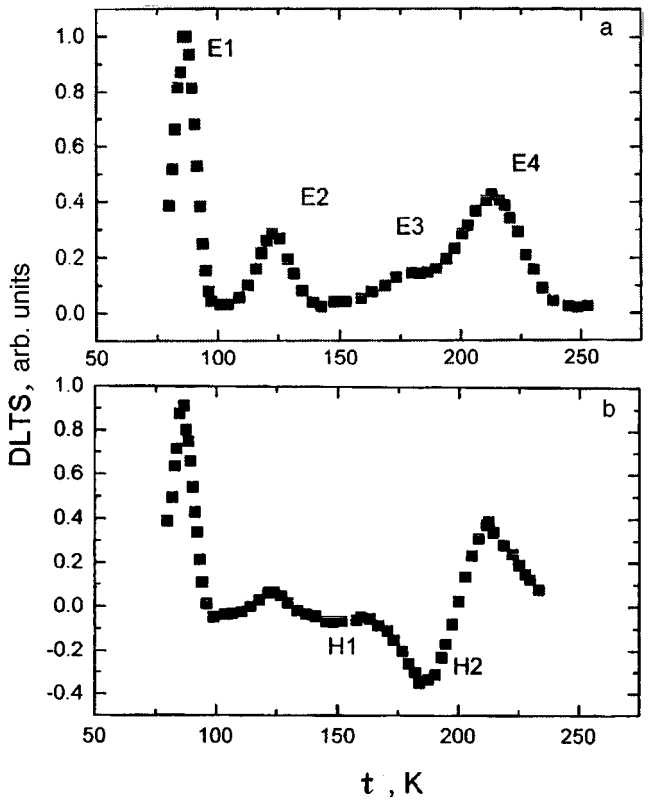

FIG. 2. DLTS spectra of a sample exposed to an α-particle dose $\Phi=1.4\times10^9$: a — without injection, b — with injection of minority carriers.

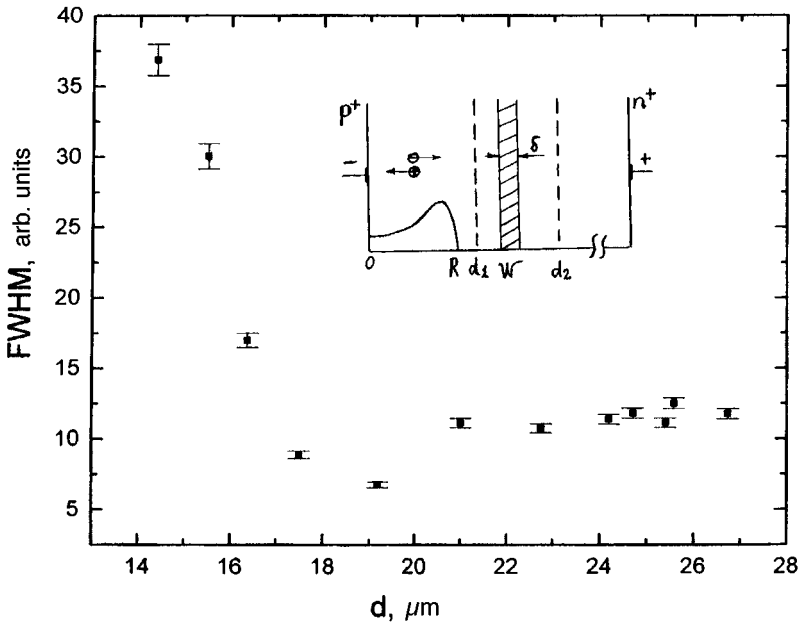

FIG. 3. Full width at half-maximum of the spectral line of a p^+–n diode versus length of field region. The diode was irradiated with an α particle dose of 1.7×10^{10} cm^{-2} and was used as a detector for single 4.5 MeV α particles (range $R=21$ μm). Inset — experimental geometry: W — position of defect layer. The cases $d_1<W$ and $d_2>W$ are explained in the text.

room-temperature irradiation, when C_i migrates rapidly. A second factor may be the high concentration of oxygen in the sample.[10]

On the whole, the system of defect levels may be described as similar to that observed previously when n-Si was irradiated by α particles.[9,11] The recovery behavior of the lifetime under isochronous annealing (for 1 h) showed that the greatest increase in the lifetime occurred at 350 °C, which, according to Refs. 9 and 12, corresponds to the predominant annealing of defects forming the damaged layer.

3. We have already noted that a defect configuration in the form of a layer is obtained from modeling the kinematics of the α-particle stopping and from DLTS experiments to study the profile of the forming centers.[5,6] We confirm this defect configuration independently for our samples by means of an experiment to study charge transfer from single α-particles. In this case, the p^+–n structure is used as a detector, i.e., it is reverse-biased. By varying the bias, it is possible to control the magnitude of the field region of the p^+–n diode — the ''working zone'' of the detector.

The monochromatic particles inject a pulse of charge-calibrated electron-hole pairs, which is recorded by a standard apparatus for nuclear spectrometry. The final characteristic is the spectral profile of the detector signal amplitudes.

We select the energy of the α particles so that their range R is inside the layer with a short lifetime (position W, see inset in Fig. 3). We select two different relations between the working zone d and W. In the first case, the field region does not reach W, i.e., $d_1<W$. In the second case, the damaged layer contains the working zone, and $d_2>W$.

When $d<W$, the electrons entering the base from the field region are majority carriers. Thus, an equal number of electrons will be injected into the n^+-contact on account of Maxwellian relaxation. Ultimately, the defects in the δ layer do not influence the signal.

When $d>W$, electrons from the α-particle track must drift across the δ layer as a packet of nonequilibrium carriers. These electrons will undergo trapping, which should be manifested mainly as spectral line broadening. Its width is extremely sensitive to incomplete charge transfer because it is determined by the product of the trapping and its volume inhomogeneity factor.[13]

Figure 3 gives the full width at half maximum (FWHM) as a function of the length of the field region. The track length of the α particles was $R=21$ μm. As long as the track is only partially within the field region, the line is broad, because of the contribution of diffusion transport for the part of the track extending into the base. With increasing d, the line becomes narrower and the lowest values are observed for $d\cong R$. Then, when the δ layer moves into the working zone, the line width is approximately doubled.

These results indicate that nonuniformity of the recombination properties in the layer geometry substantially influences both diffusion and drift transport of carriers. In this case, when the carrier lifetime is determined by the injection-extraction procedure, the incorporation of even a small quantity of defects compared with the dopant reduces the accuracy of the basic formula.

The authors would like to thank participants at the Laboratory Seminar on ''Nonequilibrium Processes in Semiconductors'' at the A. F. Ioffe Physicotechnical Institute for useful discussions.

[1] Yu. N. Nosov, *Physical Principles of the Pulsed Semiconductor Diode* [in Russian], Nauka, Moscow (1968), p. 263.
[2] V. S. Vavilov, B. M. Gorin, N. S. Danilin, A. E. Kiv, Yu. L. Nurov, and V. I. Shakhovtsov, *Radiation Methods in Solid-State Electronics* [in Russian], Radio i Svyaz', Moscow (1990), p. 263.
[3] V. V. Emtsev and T. V. Mashovets, *Impurities and Point Defects in Semiconductors* [in Russian], Radio i Svyaz', Moscow (1981), p. 248.
[4] *Ion Implantation Science and Technology*, edited by J. F. Ziegler (Academic Press, New York, 1984).
[5] L. S. Berman, A. M. Ivanov, and N. B. Strokan, Pis'ma Zh. Tekh. Fiz. **19**(20), 24 (1993) [Tech. Phys. Lett. **19**, 647 (1993)].

[6] L. S. Berman, A. M. Malyarenko, A. D. Remenyuk, V. L. Sukhanov, and M. G. Tolstobrov, Fiz. Tekh. Poluprovodn. **22**, 844 (1988) [Sov. Phys. Semicond. **22**, 532 (1988)].
[7] A. M. Ivanov, I. N. Il'yashenko, N. B. Strokan, and B. Schmidt, Fiz. Tekh. Poluprovodn. **29**, 543 (1995) [Semiconductors **29**, 281 (1995)].
[8] M. Byczkowski and J. R. Madigan, J. Appl. Phys. **28**, 878 (1957).
[9] E. M. Verbitskaya, V. K. Eremin, A. M. Ivanov, and N. B. Strokan, Fiz. Tekh. Poluprovodn. **27**, 205 (1993) [Semiconductors **27**, 115 (1993)].
[10] B. Schmidt, V. Eremin, A. Ivanov, N. Strokan, E. Verbitskaya, and Z. Li, J. Appl. Phys. **76**, 4072 (1994).
[11] N. V. Kuznetsov, V. N. Filatov, and V. F. Vinogradova, Fiz. Tekh. Poluprovodn. **21**, 609 (1987) [Sov. Phys. Semicond. **21**, 374 (1987)].
[12] V. S. Vavilov, V. F. Kiselev, and B. N. Mukashev, *Bulk and Surface Defects in Silicon* [in Russian], Nauka, Moscow (1990), p. 212.
[13] L. L. Makovsky, N. B. Strokan, and N. I. Tisnek, IEEE Trans. Nucl. Sci. **NS-15**, 304 (1968).

Translated by R. M. Durham

Polarization switching time for semiconductor laser radiation

G. S. Sokolovskiĭ, A. G. Deryagin, and V. I. Kuchinskiĭ

A. F. Ioffe Physicotechnical Institute, Russian Academy of Sciences, St. Petersburg
(Submitted December 11, 1996)
Pis'ma Zh. Tekh. Fiz. **23**, 87–95 (May 12, 1997)

Expressions are derived for the polarization switching time for semiconductor laser radiation. These expressions can be used to assess the influence of the laser diode parameters on the polarization switching time of the output radiation. The results of an analysis of these expressions show that the main parameters influencing the polarization switching of the output radiation from a semiconductor laser are the nonlinear gains. © *1997 American Institute of Physics.* [S1063-7850(97)01605-4]

Switching, coexistence, and bistability of the TM/TE polarizations in the radiation from strained-layer semiconductor lasers have been observed in Refs. 1–3 and 5–7. In Ref. 3, particular emphasis was placed in the selective role of the cavity. Later, a quantum-mechanical model was proposed in Ref. 4 to describe intraband transitions in strained semiconductor layers, and it was shown[5] that the polarization of the laser radiation depends on the position of the lasing line on the gain profile. A phenomenological model was developed in Refs. 6 and 7 to explain polarization switching and polarization bistability.

Semiconductor lasers with polarization switching and bistability may be extremely useful for optical processing and data transfer systems, for example, in systems with polarization multiplexing[8] This poses the question as to how rapidly the polarization can be reversed. Unfortunately, so far, this problem clearly has not received sufficient attention in the literature.

We have set out to obtain explicit expressions for the polarization switching time of semiconductor laser radiation and to assess the influence of the laser diode parameters on this switching time.

The Lyapunov method[9] — analysis of the stability of solutions of systems of differential equations — was applied to a system of rate equations to obtain an analytic expression for the polarization switching time of semiconductor laser radiation. According to Lyapunov, the state of a system is stable (unstable) if a small deviation from this state at time $t=0$, remains small (increases) over time $0<t<\infty$. Since this deviation is small, the system of differential equations may be linearized. The time dependence of a small deviation from the equilibrium position may be expressed as follows:

$$\delta(t)=\sum_i A_i V_i e^{P_i t}, \tag{1}$$

where P_i are the eigenvalues and V_i are the eigenvectors of the linearized system. The equilibrium position of the system is stable (unstable) if the real parts of all — one or more — of the eigenvalues P_i are negative (positive). It is important to note that the eigenvalues P_i are the characteristic times for transition of the system from one equilibrium position to another.

The system of rate equations has the form

$$\begin{cases} \dfrac{dN}{dt}=\dfrac{1}{qV}-g_{\mathrm{TE}}(N-N_{\mathrm{TE}})(1-\varepsilon_{\mathrm{EE}}S_{\mathrm{TE}}-\varepsilon_{\mathrm{EM}}S_{\mathrm{TM}})S_{\mathrm{TE}} \\ \qquad -g_{\mathrm{TM}}(N-N_{\mathrm{TM}})(1-\varepsilon_{\mathrm{ME}}S_{\mathrm{TE}}-\varepsilon_{\mathrm{MM}}S_{\mathrm{TM}})S_{\mathrm{TM}}-\dfrac{N}{\tau}, \\ \dfrac{dS_{\mathrm{TE}}}{dt}=g_{\mathrm{TE}}(N-N_{\mathrm{TE}})(1-\varepsilon_{\mathrm{EE}}S_{\mathrm{TE}}-\varepsilon_{\mathrm{EM}}S_{\mathrm{TM}})S_{\mathrm{TE}} \\ \qquad +\beta\dfrac{N}{\tau}-\dfrac{S_{\mathrm{TE}}}{\tau_{\mathrm{TE}}}, \\ \dfrac{dS_{\mathrm{TM}}}{dt}=g_{\mathrm{TM}}(N-N_{\mathrm{TM}})(1-\varepsilon_{\mathrm{ME}}S_{\mathrm{TE}}-\varepsilon_{\mathrm{MM}}S_{\mathrm{TM}})S_{\mathrm{TM}} \\ \qquad +\beta\dfrac{N}{\tau}-\dfrac{S_{\mathrm{TM}}}{\tau_{\mathrm{TM}}}, \end{cases} \tag{2}$$

where N is the carrier concentration, $s_{\mathrm{TE/TM}}$ is the density of TE/TM-polarized photons, $g_{\mathrm{TE/TM}}$ is the linear gain for TE/TM-polarized light, $\tau_{\mathrm{TE/TM}}$ is the lifetime of TE/TM-polarized photons, $N_{\mathrm{TE/TM}}$ is the transparency concentration for TE/TM-polarized light, τ is the carrier lifetime, ε_{ij} are the nonlinear gains, β is the coefficient of spontaneous emission, q is the elementary charge, and V is the volume of the active medium. The stability of system (2) was analyzed using the constant carrier approximation $dN/dt=0$. This condition allows us to perform the very convenient transformation

$$\begin{cases} \dfrac{dS_{\mathrm{TE}}}{dt}=g_{\mathrm{TE}}\tau\left(\dfrac{I}{qV}-\dfrac{S_{\mathrm{TE}}}{\tau_{\mathrm{TE}}}-\dfrac{S_{\mathrm{TM}}}{\tau_{\mathrm{TM}}}-\dfrac{N_{\mathrm{TE}}}{\tau}\right) \\ \qquad \times(1-\varepsilon_{\mathrm{EE}}S_{\mathrm{TE}}-\varepsilon_{\mathrm{EM}}S_{\mathrm{TM}})S_{\mathrm{TE}}-\dfrac{S_{TE}}{\tau_{\mathrm{TE}}}, \\ \dfrac{dS_{\mathrm{TM}}}{dt}=g_{\mathrm{TM}}\tau\left(\dfrac{1}{qV}-\dfrac{S_{\mathrm{TE}}}{\tau_{\mathrm{TE}}}-\dfrac{S_{\mathrm{TM}}}{\tau_{\mathrm{TM}}}-\dfrac{N_{\mathrm{TM}}}{\tau}\right) \\ \qquad \times(1-\varepsilon_{\mathrm{ME}}S_{\mathrm{TE}}-\varepsilon_{\mathrm{MM}}S_{\mathrm{TM}})S_{\mathrm{TM}}-\dfrac{S_{TM}}{\tau_{\mathrm{TM}}}. \end{cases} \tag{3}$$

The ''trivial'' solutions $S_{\mathrm{TE}}=0$, $S_{\mathrm{TM}}\neq 0$ (TM-polarized radiation) and $S_{\mathrm{TE}}\neq 0$, $S_{\mathrm{TM}}=0$ (TE-polarized radiation) are of particular interest for investigation purposes. Having linearized the modified system of rate equations (3), we obtain

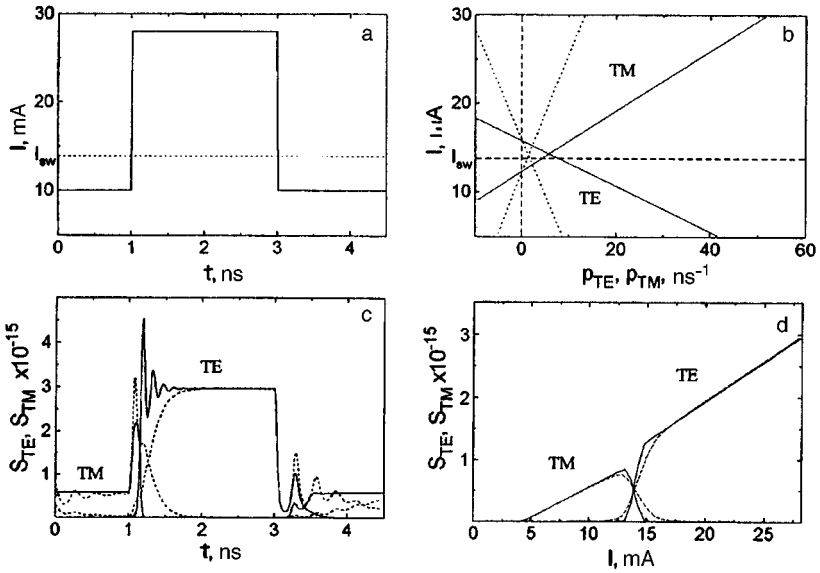

FIG. 1. a — Time dependence of pump current, b — stability coefficients p_{TE} and p_{TM} versus pump current, c — results of numerical modeling of polarization switching process, and d — calculated power-current characteristic. The dashed curves refer to a laser with the parameters $\varepsilon_{\mathrm{ME}}=1.5\times10^{-17}$ cm^3, $\varepsilon_{\mathrm{MM}}=2.0\times10^{-17}$ cm^3, and $\tau_{\mathrm{TM}}=1.55$ ps, and the solid curves refer to a laser with the parameters $\varepsilon_{\mathrm{ME}}=4.5\times10^{-17}$ cm^3, $\varepsilon_{\mathrm{MM}}=6.0\times10^{-17}$ cm^3, and $\tau_{\mathrm{TM}}=1.61$ ps. The other laser parameters are the same: $g_{\mathrm{TE}}=1.45\times10^{-6}$ cm^3/s, $g_{\mathrm{TM}}=1.40\times10^{-6}$ cm^3/s, $\tau_{\mathrm{TE}}=2.0$ ps, $N_{\mathrm{TE}}=4.5\times10^{17}$ cm^{-3}, $N_{\mathrm{TM}}=3.29\times10^{17}$ cm^{-3}, $\tau=3$ ns, $\varepsilon_{\mathrm{EM}}=2.0\times10^{-17}$ cm^3, and $\varepsilon_{\mathrm{EE}}=1.0\times10^{-17}$ cm^3.

its eigenvalues, which, in accordance with formula (1), are also called coefficients of stability (instability):

$$P_{\mathrm{TE/TM}}=g_{\mathrm{TE/TM}}\left(\frac{1}{qV}-\frac{S_{\mathrm{TM/TE}}}{\tau_{\mathrm{TM/TE}}}-\frac{N_{\mathrm{TE/TM}}}{\tau}\right)\times(1-\varepsilon_{\mathrm{EM/ME}}s_{\mathrm{TM/TE}})-\frac{1}{\tau_{\mathrm{TE/TM}}},\tag{4}$$

where $s_{\mathrm{TE/TM}}$ is the density of TE/TM-polarized photons in the absence of the other polarization:

$$S_{\mathrm{TE/TM}}=\frac{1}{2}\left(\frac{1}{\varepsilon_{\mathrm{EE/MM}}}+\tau_{\mathrm{TE/TM}}\left(\frac{1}{qV}-\frac{N_{\mathrm{TE/TM}}}{\tau}\right)\right)-\sqrt{\frac{1}{4}\left(\frac{1}{\varepsilon_{\mathrm{EE/MM}}}+\tau_{\mathrm{TE/TM}}\left(\frac{1}{qV}-\frac{N_{\mathrm{TE/TM}}}{\tau}\right)\right)^2-\frac{\tau_{\mathrm{TE/TM}}}{\varepsilon_{\mathrm{EE/MM}}}\left(\frac{I}{qV}-\frac{N_{\mathrm{TE/TM}}}{\tau}-\frac{1}{g_{\mathrm{TE/TM}}\tau\tau_{\mathrm{TE/TM}}}\right)}.\tag{5}$$

It can be seen from Eq. (4) that three combinations of stability coefficients $P_{\mathrm{TE/TM}}$ are possible: both coefficients are positive — the ''trivial'' solutions are unstable, i.e., TE and TM modes coexist; both coefficients are negative — bistable state, and lastly, the stability coefficients have different signs — in this case, the laser emits radiation of that polarization for which the eigenvalue is negative. We shall examine these three cases in greater detail.

When one of the stability coefficients is negative and the other positive, the latter is inversely proportional to the polarization reversal time of the laser output radiation. For example, switching the laser pump current from the value I_1, corresponding to TM-polarized output radiation, to I_2 corresponding to the TE polarization (Fig. 1a), results in switching of the output radiation with the characteristic time $1/P_{\mathrm{TM}}(I_2)$ (Fig. 1b). Figure 1c shows the results of a numerical simulation of the polarization switching process of the output radiation from two InGaAsP/InP ($\lambda=1.55\mu$m) lasers, whose parameters are given in the caption. It can be seen that at low pump currents, TM-polarized radiation predominates for both lasers, whereas when the current is increased above a certain level I_{sw}, the TE polarization predominates (Fig. 1d). Here, I_{sw} is the polarization switching current, i.e., the pump current corresponding to unpolarized laser output radiation. Its exact value can be calculated if we assume in formula (3) that $S_{\mathrm{TE}}=S_{\mathrm{TM}}=S_{\mathrm{sw}}$ and $dS_{\mathrm{TE}}/dt=dS_{\mathrm{TM}}/dt=0$:

$$I_{\mathrm{sw}}=\frac{1}{g_{\mathrm{TE}}\tau\tau_{\mathrm{TE}}(1-\varepsilon_{\mathrm{E}}S_{\mathrm{sw}})}+\left(\frac{1}{\tau\mathrm{TE}}+\frac{1}{\tau_{\mathrm{TM}}}\right)S_{\mathrm{sw}}+\frac{N_{\mathrm{TE}}}{\tau},$$

$$S_{\mathrm{sw}}=B-\sqrt{B^2-C},\tag{6}$$

$$B=\frac{1}{2}\left(\frac{1}{\varepsilon_{\mathrm{E}}}+\frac{1}{\varepsilon_{\mathrm{M}}}+\frac{1}{g_{\mathrm{TE}}\tau_{\mathrm{TE}}\varepsilon_{\mathrm{E}}\Delta N}-\frac{1}{g_{\mathrm{TM}}\tau_{\mathrm{TM}}\varepsilon_{\mathrm{M}}\Delta N}\right),$$

$$C=\frac{1}{\varepsilon_{\mathrm{E}}\varepsilon_{\mathrm{M}}}\left(1+\left(\frac{1}{g_{\mathrm{TE}}\tau_{\mathrm{TE}}}-\frac{1}{g_{\mathrm{TM}}\tau_{\mathrm{TM}}}\right)\Delta N\right),$$

$$\varepsilon_{\mathrm{E}}=\varepsilon_{\mathrm{EE}}+\varepsilon_{\mathrm{EM}},\quad \varepsilon_{\mathrm{M}}=\varepsilon_{\mathrm{MM}}+\varepsilon_{\mathrm{ME}},$$

$$\Delta N=N_{\mathrm{TE}}-N_{\mathrm{TM}}.$$

The time taken for a change in the pump current to induce polarization reversal (switching) of the laser output radiation is defined as the reciprocal of the stability coefficient (4) of the system, calculated for the ''new'' pump current. In other words, in this particular case polarization switching takes place in a time, the reciprocal of the system eigenvalue (stability coefficient), which is positive for the new pump current (Figs. 1b and 1c). The parameters of the lasers *1* (dashed curves) and *2* (solid curves) are selected so that the polarization switching times are the same. It can be seen from Figs. 1b and 1c that under the same conditions, the polarization switching for laser *1*, whose stability coefficients are ≈5 times greater than those of laser *2*, is approximately five times faster. Thus, the results of the numerical modeling (Fig. 1c) show good agreement with those obtained from the analytic expressions (Fig. 1b).

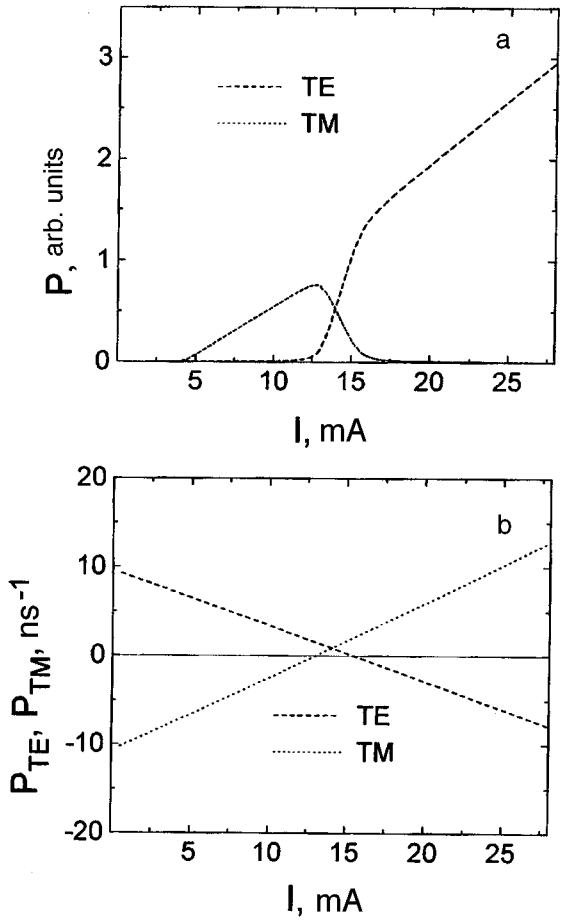

FIG. 2. a — Densities of TE- and TM-polarized photons versus pump current for a laser with the parameters: $g_{TE}=1.45\times10^{-6}$ cm^3/s, $g_{TM}=1.40\times10^{-6}$ cm/s, $\tau_{TE}=2.0$ ps, $\tau_{TM}=1.55$ ps, $N_{TE}=4.5\times10^{17}$ cm^{-3}, $N_{TM}=3.29\times10^{17}$ cm^{-3}, $\tau=3$ ns, $\varepsilon_{EE}=1.0\times10^{-17}$ cm^3, $\varepsilon_{ME}=1.5\times10^{-17}$ cm^3, $\varepsilon_{MM}=2.0\times10^{-17}$ cm^3, and $\varepsilon_{EM}=2.0\times10^{-17}$ cm^3; b — Coefficients of stability of TE- and TM-polarized modes versus pump current.

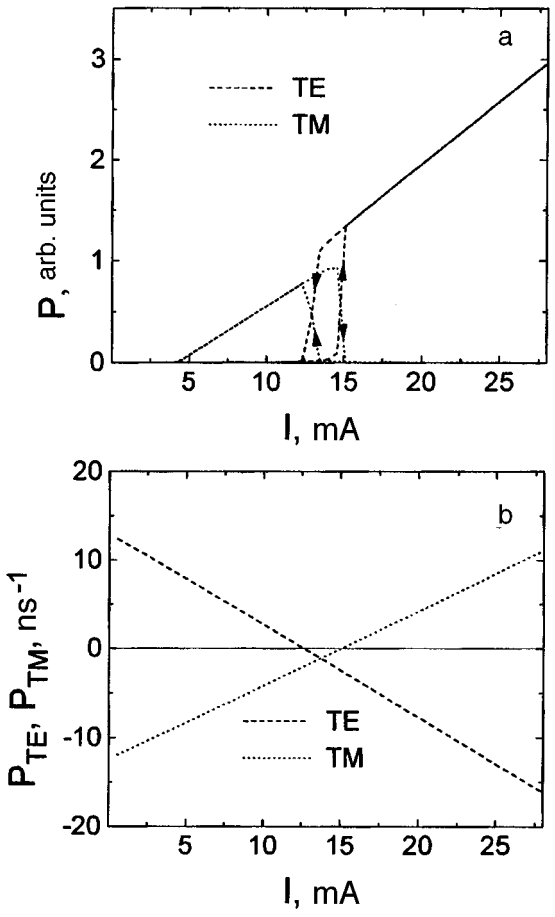

FIG. 3. a — Densities of TE- and TM-polarized photons versus pump current for a laser with the parameters: $g_{TE}=1.45\times10^{-6}$ cm^3/s, $g_{TM}=1.40\times10^{-6}$ cm^3/s, $\tau_{TE}=2.0$ ps, $\tau_{TM}=1.55$ ps, $N_{TE}=4.5\times10^{17}$ cm^{-3}, $N_{TM}=3.29\times10^{17}$ cm^{-3}, $\tau=3$ ns, $\varepsilon_{EE}=1.0\times10^{-17}$ cm^3, $\varepsilon_{ME}=1.0\times10^{-17}$ cm^3, $\varepsilon_{MM}=2.0\times10^{-17}$ cm^3, and $\varepsilon_{EM}=2.0\times10^{-17}$ cm^3; b — stability of TE- and TM-polarized modes versus pump current.

The results of our analysis of expressions (4) and (5) indicate that when the polarization switching current (6) is constant, the polarization switching time only depends on the nonlinear gains ε_{ij} and does not depend on the linear parameters of the laser diode.

We shall now examine cases where the stability coefficients have the same sign. When both the eigenvalues are positive, the trivial states are unstable, modes of both polarizations coexist, and the concentrations of TE- and TM-polarized photons cease to be described by the expressions (5). As the pump current of the laser diode varies smoothly (Fig. 2a) in this range (Fig. 2b), we observe smooth polarization switching of the laser output radiation (Fig. 2a).

In the range of laser diode parameters where both stability coefficients are negative, a minor contradiction can be identified: both trivial states are stable, although the existence of one precludes the existence of the other (see above). This is the region of bistability, where the polarization of the laser output radiation is determined by the state of the system before its entry into this region. As the pump current of the laser diode varies smoothly (Fig. 3a) in a certain range where both stability coefficients are negative (Fig. 3b) there exist two values of the pump current for which laser output radiation undergoes polarization switching (Fig. 3a), and the switching is observed when the laser ''leaves'' the bistable state. The power-current characteristic of the laser in this range exhibits hysteresis whose width can be determined from the expressions (4).

To sum up, we have proposed expressions for the polarization switching time for semiconductor laser radiation. These expressions have been used to assess the influence of the laser diode parameters on the polarization switching time of the output radiation. The results of an analysis of these expressions have demonstrated that the main parameters influencing the polarization switching process of semiconductor laser output radiation are the nonlinear gains.

The authors would like to thank E. L. Portnoĭ for his continuous attention and interest in this work.

The work was supported financially by the Russian Fund for Fundamental Research (Project Code 96-02-17864a).

[1] D. Akhmedov, N. P. Bezhan, N. A. Bert, S. G. Konnikov, V. I. Kuchinskiĭ, V. A. Mishurnyĭ, and E. L. Portnoĭ, Pis'ma Zh. Tekh. Fiz. **6**, 705 (1980) [Sov. Tech. Phys. Lett. **6**, 304 (1980)].

[2] V. A. Elyukhin, V. R. Kocharyan, E. L. Portnoĭ, and B. S. Ryvkin, Pis'ma Zh. Éksp. Teor. Fiz. **6**, 708 (1980) [Sov. Tech. Phys. Lett. **6**, 305(1980)].
[3] K. G. Kalandarishvili, S. Yu. Karpov, V. I. Kuchinskiĭ, M. N. Mizerov, E. L. Portnoĭ, and V. B. Smirnitskiĭ, Zh. Tekh. Fiz. **53**, 1560 (1983) [Sov. Phys. Tech. Phys. **28**, 959 (1983)].
[4] E. A. Avrutin, M. A. Alekseev, V. I. Kuchinskiĭ, and A. S. Lazutka, Fiz. Tekh. Poluprovodn. **23**, 1207 (1989) [Sov. Phys. Semicond. **23**, 755 (1989)].
[5] A. G. Deryagin, D. V. Kuksenkov, V. I. Kuchinskii, E. L. Portnoi, and V. B. Smirnitskii, IEE Proc.-Optoelectron. **142**, 51 (1995).
[6] Y. C. Chen and J. M. Liu, Opt. Quantum Electron. **19**, S93 (1987).
[7] G. Ropars, A. Le Floch, G. Jézéquel, R. Le Naour, Y. C. Chen, and J.-M. Liu, IEEE J. Quantum Electron. **QE-23**, 1027 (1987).
[8] P. M. Hill, R. Olshansky, and W. K. Burns, IEEE Photon. Tech. Lett. **4**, 500 (1992).
[9] A. M. Lyapunov, *The General Problem of the Stability of Motion* [in Russian], Gostekhizdat, Moscow (1950).

Translated by R. M. Durham

Photopleochroism of oxide–*p*-InSe diode structures

V. N. Katerinchuk and M. Z. Kovalyuk

Branch of the Institute of Problems in Materials Science, Ukrainian National Academy of Sciences, Chernovtsy

(Submitted November 26, 1996)
Pis'ma Zh. Tekh. Fiz. **23**, 1–3 (May 26, 1997)

A layered InSe crystal is used to fabricate a polarimetric photodetector. The heterostructure is formed in the plane perpendicular to the cleavage plane of the layers by thermal oxidation of the crystal substrate. The coefficient of photopleochroism of the oxide–*p*-InSe photodiode for 0.6328 nm light is 90%. © *1997 American Institute of Physics.* [S1063-7850(97)01705-9]

The development of high-efficiency polarimetric photodetectors involves searching for new anisotropic semiconductors, and the possibility of using these to fabricate high-quality barrier structures.[1] In this context, the use of III-VI semiconductors with a layered crystal structure deserves attention.[2] In particular, a high coefficient of photopleochroism, 93%, was achieved in Ref. 2 for an n^+-In_2O_3–*p*-GaSe heterostructure.

With the aim of developing a similar polarimetric detector exhibiting spectral sensitivity, we investigated another III-VI layered compound — indium monoselenide — a semiconductor with a band gap of 1.2 eV and well-defined anisotropic mechanical and electrophysical properties.[3] However, this soft material is not amenable to conventional mechanical treatment. Thus, the surface plane of the sample required to fabricate the detector was prepared by detaching blocks of specially grown block single crystals. Because of the random arrangement of the blocks, the samples can be cleaved along the cleavage planes of the layers with a natural, almost perpendicular, end plane, which then serves as the base for forming the barrier.

The oxide–*p*-InSe heterostructure was prepared by the method described in Ref. 4. The photosensitive area of the diodes measured 8–10 mm^2, the current–voltage characteristics showed rectifying characteristics, and the saturation photovoltage was 0.2 V.

The experimental geometry and the angular dependence of the photocurrent for polarized light incident on the end surface of the crystal are given in Fig. 1. Here, φ is the angle between the cleavage planes of the InSe layers and the electric field vector of the light wave. Besides the experimental curve (open circles), Fig. 1 also gives the theoretical curve (dashed curve) calculated with the expression[1]

$$i_\varphi = i_b \cos^2 \varphi + i_a \sin^2 \varphi, \tag{1}$$

where i_a and i_b are the photocurrents for two mutually perpendicular orientations of the electric field vector of the light wave relative to the crystallographic *c* axis of indium selenide. It can be seen that the photoheterostructure possesses well-defined sensitivity to the polarization of the incident radiation. The ratio i_b/i_a was of the order of 20 and the

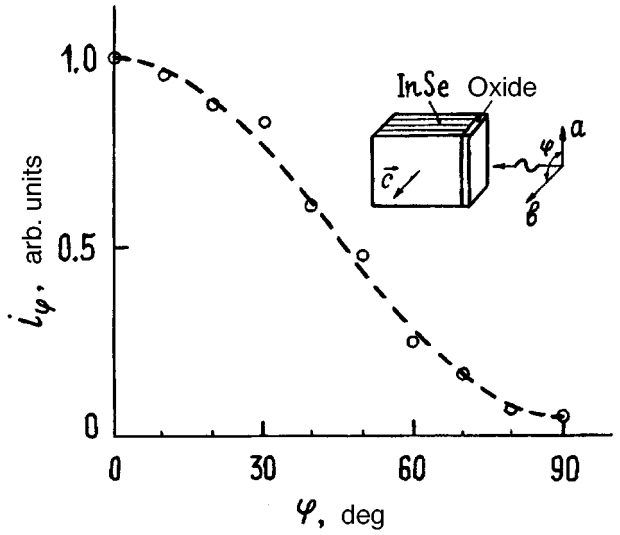

FIG. 1. Experimental geometry and angular dependence of the photocurrent of oxide–*p*–InSe heterostructures exposed to polarized radiation: *a* — $E \perp c$, *b* — $E \| c$ (E is the electric field vector of the light wave). Open circles — experiment, dashed curve — calculations.

coefficient of photopleochroism at 632.8 nm (helium–neon laser radiation), determined according to the formula[1]

$$P = (i_b - i_a)/(i_b + i_a) \tag{2}$$

was 90%.

To conclude, we have shown that indium selenide may be used as the basis for fabricating photodetectors for polarized radiation.

[1] Yu. V. Rud', Ivz. Vyssh. Uchebn. Zaved. Radiofiz. **29**, 68 (1986).
[2] V. A. Manasson, Z. D. Kovalyuk, S. I. Drapak, and V. N. Katerinchuk, Electron. Lett. **26**, 664 (1990).
[3] A. V. Novoselova, V. B. Lazarev, Z. S. Medvedeva *et al.*, *Handbook of Physicochemical Properties of Semiconductors* [in Russian], Nauka, Moscow (1973).
[4] V. N. Katerinchuk and M. Z. Kovalyuk, Pis'ma Zh. Tekh. Fiz. **18**(12), 70 (1992) [Sov. Tech. Phys. Lett. **18**, 394(1992)].

Translated by R. M. Durham

Influence of laser radiation on the electrodiffusion of molecular ions in a porous glass rod

I. K. Meshkovskiĭ and O. V. Klim

St. Petersburg State Institute of Precision Mechanics and Optics (Technical University)
(Submitted January 24, 1997)
Pis'ma Zh. Tekh. Fiz. **23**, 4–8 (May 26, 1997)

The influence of laser radiation on the electrodiffusion of dye ions in porous glass has been investigated. It is shown that when the molecular ions are exposed to intense photoexcitation, the rate of electrodiffusion in the porous glass is reduced substantially. The influence of temperature on the electrodiffusion process is studied. © *1997 American Institute of Physics.* [S1063-7850(97)01805-3]

The first studies of the influence of laser radiation on the diffusion of molecules through a porous glass membrane[1,2] showed that photoexcitation of the electronic and vibrational subsystems of gas-phase molecules reduced the mobility of those molecules in porous membranes.

In view of the considerable potential for using these methods in the photoseparation of elements and substances in solutions,[3] our aim in the present study was to examine the influence of laser radiation on the electrodiffusion flux of molecular ions of various laser dyes dissolved in ethanol, as they migrate electrically through a porous glass rod.

EXPERIMENT

For the experiments we prepared $4\times4\times15$ mm parallelepipeds of DV-1M porous glass,[4] which are used as the bases of solid-state active elements for tunable dye lasers.[5–7]

The experiments were carried out on a batch of twelve samples. Ethanol solutions of rhodamine G and thionine at a concentration of 2×10^{-4} mol/liter were used as the dye solution.

The apparatus is shown schematically in Fig. 1. A porous parallelepiped *1* was preheated at 150 °C to remove any moisture and then soaked in pure ethanol. One end was then attached to a lid with a holder *2*, to which a cathode was connected, and was placed in a cell *3* so that the other end was in contact with the dye solution. The anode was inserted directly into the solution. An image of the parallelepiped was formed on a screen *6* by means of a projection system *4* and *5*.

When an electric potential is applied, the molecular ions are attracted by the field and move from the anode toward the cathode. This is observed as propagation of a coloration front on a millimeter scale on the screen. Facilities were provided for irradiation of the porous glass rod by LG-106M-1 argon laser radiation perpendicular to the axis of the projection system. The laser beam was defocused by a lens *8* so that the entire zone of propagation of the dye was irradiated.

Figure 2a shows the motion of the coloration front as a function of time for a rhodamine G solution when the temperature is the porous rod is 20 °C (curve *1*) and 60 °C (curve *2*) with no laser irradiation of the sample.

Figure 2b shows the motion of the coloration front as a function of time for a rhodamine G solution at 20 °C with no laser irradiation (curve *1*) and with laser irradiation at a power density of ~5 W/cm^2 (curve *2*).

DISCUSSION OF RESULTS

It can be seen from the data plotted in Fig. 1a that the rate of electromigration increases with temperature. The results plotted in Fig. 2b show that laser irradiation of the molecules substantially reduces the rate of electrodiffusion. For comparison, Fig. 2c gives results of similar experiments for thionine molecular ions. The absorption band of a rhodamine G solution in ethanol (λ_{max}=530 nm) coincides with the emission spectrum of an argon laser. Thionine has an absorption band maximum around 590 nm and is not very efficiently excited by argon laser radiation. These data indicate that laser radiation only influences electromigration when the molecules undergo intense photexcitation.

These results demonstrate that when molecules are exposed to exciting radiation, their mobility in a porous matrix is reduced. This effect may be utilized for separation of isotopes, atoms, and molecules, and electromigration may be used to enhance the efficiency of the separation process by several orders of magnitude.

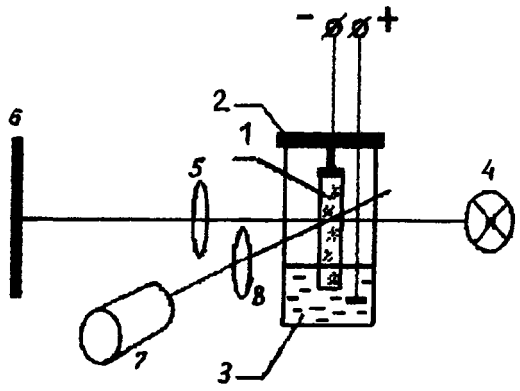

FIG. 1. Schematic diagram of apparatus: *1* — porous rod, *2* — lid and holder, *3* — cell containing dye solution, *4* — light source, *5* — projection lens, *6* — screen, *7* — argon laser, and *8* — defocusing lens.

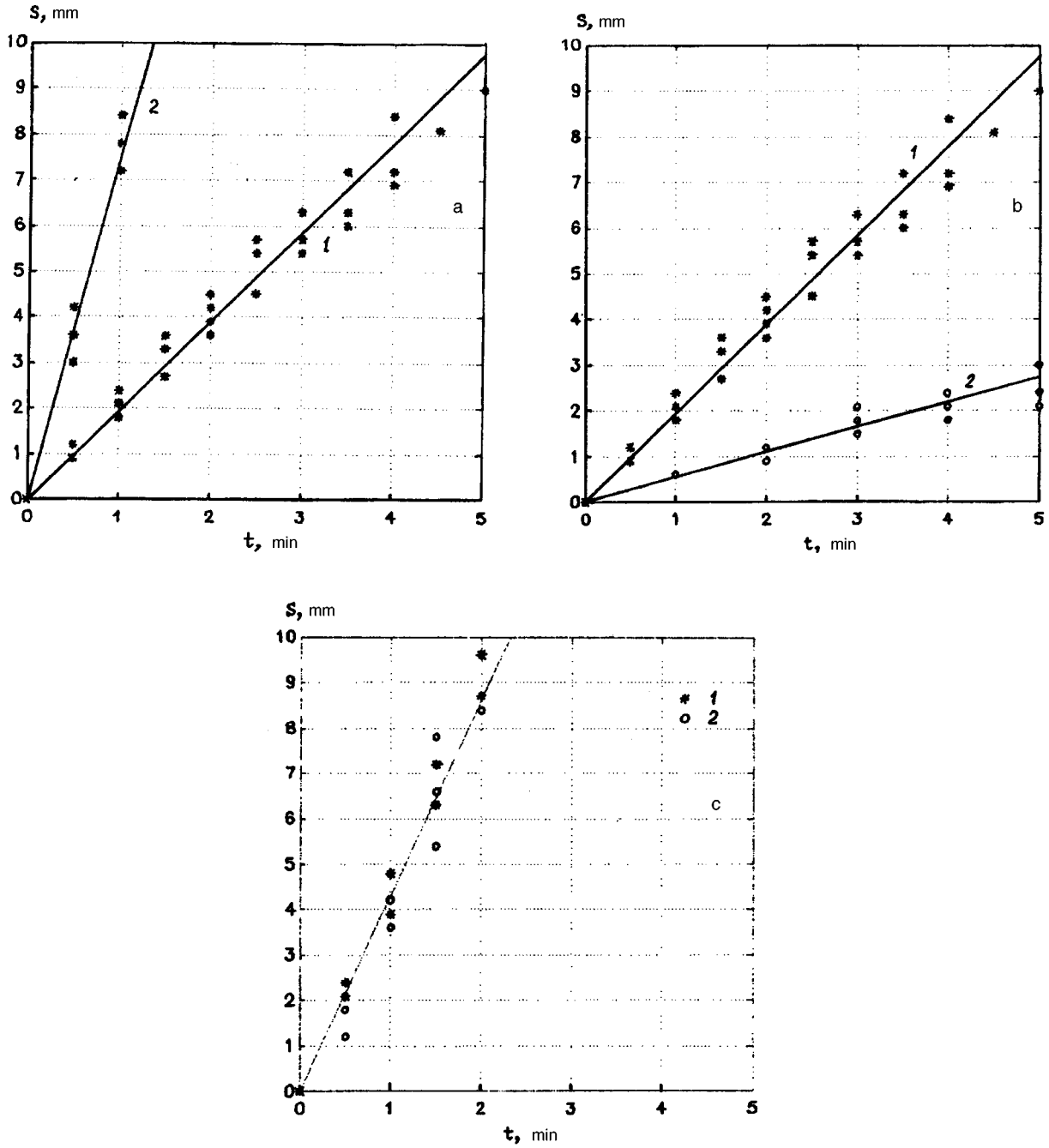

FIG. 2. Displacement of coloration front versus time caused by electromigration of the dye with a voltage of 300 V applied to the electrodes: a — for an ethanol solution of rhodamine G without laser irradiation: *1* — at 20 °C and *2* — at 60 °C; b — for an ethanol solution of rhodamine G at 20°: *1* — without laser irradiation, *2* — with laser irradiation; c — for an ethanol solution of thionine at 20 °C: *1* — without laser irradiation and *2* — with laser irradiation.

[1] N. V. Karlov, I. K. Meshkovskiĭ, R. P. Petrov, Yu. N. Petrov, and A. M. Prokhorov, JETP Lett. **30**, 42 (1979).
[2] V. A. Kravchenko, É. N. Lotkova, I. K. Meshkovskiĭ, and Yu. N. Petrov, Pis'ma Zh. Tekh. Fiz. **7**, 1197 (1981) [Sov. Tech. Phys. Lett. **7**, 512 (1981)].
[3] *Laser Applications in Spectroscopy and Photochemistry* [in Russian], Mir, Moscow, 1983.
[4] I. K. Meshkovskiĭ, G. M. Belotserkovskiĭ, T. G. Plachenov, and O. S. Molchanova, Zh. Prikl. Khim. No. 7, 1452 (1968).
[5] I. K. Meshkovskiĭ, *A Dye Laser Active Element*, Inventor's Certificate No. 725536 (1979) [Russian].
[6] G. N. Dul'nev, V. I. Zemskiĭ, B. B. Krynetskiĭ, I. K. Meshkovskiĭ, A. M. Prokhorov, and O. M. Stel'makh, Izv. Akad. Nauk SSSR Ser. Fiz. **43**, 237 (1979).
[7] G. V. Al'tshuler, E. G. Dul'neva, and A. V. Erofeev, Zh. Tekh. Fiz. **55**, 1622 (1985) [Sov. Phys. Tech. Phys. **30**, 941 (1985)].

Translated by R. M. Durham

Conversion of phase modulation of light into intensity modulation by means of an external fiber-optic interferometer

O. I. Kotov, L. B. Liokumovich, V. M. Nikolaev, V. Yu. Petrun'kin, and Zekhraui Buabid

St. Petersburg State Technical University
(Submitted January 24, 1997)
Pis'ma Zh. Tekh. Fiz. **23**, 9–16 (May 26, 1997)

A new method of detecting phase modulation, based on using an ''external'' optical waveguide interferometer, is considered. This ''detection'' is weakly dependent on the length, position, and external conditions of the propagation channel for the phase-modulated light and, in many cases may prove more efficient than conventional methods of constructing phase-modulated fiber-optic systems. © *1997 American Institute of Physics.* [S1063-7850(97)01905-8]

In optical systems with phase modulation, the phase modulation of the light must be converted into intensity modulation for the information signal to be recorded by a photodetector. This problem arises in data acquisition and transmission systems, measuring systems, and so forth.[1–3] Phase modulation is converted into intensity modulation by means of Fabry–Perot, Mach–Zehnder, or other interference systems.[4,5] The optical (fiber-optic) channel in which the phase-modulated light undergoes modulation and propagates is usually incorporated directly in the interference system. The action of an external medium on the signal propagation channel causes the optical length to drift. This is the well-known problem of compensating for the slow temperature drift of the interferometer operating point in interferometric detectors and phase-modulated data acquisition and transmission lines.[5–7] When the channel is fairly long, it becomes difficult to compensate for the drift of the operating point of the interference system during recording and processing of the output signal. Special optical detection techniques which reduce the signal ''fading'' are complex and not very effective.[8–10]

In many cases, the action on the fiber-optic sensing element is narrow-band and quasiharmonic. Under these conditions, an interferometer external to the propagation channel of the phase-modulated light may be used to convert the phase modulation into intensity modulation in extended fiber systems. Characteristic features of this type of detection are considered in the present paper.

An external interferometer may be used to convert frequency and phase modulation into intensity modulation, since frequency and phase modulation belong to the same type of angular modulation and are connected by an integrodifferential relation. The first of these conversions is widely used, for instance, in laser frequency stabilization systems.[11] The conversion of phase modulation into intensity modulation by an external interferometer has been less well studied, and is not used because of its poor efficiency with ordinary mirror interferometers. As shown below, a fiber-optic interferometer with a large difference between the beam paths can be used for efficient conversion of phase modulation into intensity modulation and for recording information in phase-modulated optical systems. This method of constructing extended measuring and transmitting phase systems can overcome many of the shortcomings inherent in other known methods, and especially can dramatically reduce the influence of the external conditions of the propagation channel on the detection of the useful signal.

We consider a fiber-optic system containing a source of coherent optical radiation, an optical waveguide with an attached phase modulator (or another phase-modulating device), a fiber interferometer, and a photodetector (Fig. 1). When a harmonic signal is fed to the modulator, we obtain optical radiation with harmonic modulation of the phase ψ at the fiber exit:

$$\psi = \psi_0 + \delta\psi \sin(\Omega t). \tag{1}$$

For simplicity, we shall assume that single-mode lossless isotropic fibers are used and that the interferometer is a two-beam type. This last condition is satisfied for double-arm interferometers or low-Q multipass interferometers. Assuming these conditions, one can show that when radiation with the phase (1) is fed into the interferometer, the variable intensity component at the exit will be

$$I_-(t) = I_0 A \cdot \cos[2\,\delta\psi \cdot \sin(\Omega L n/2c) \times \cos(\Omega\{t-\tau\} + \beta L], \tag{2}$$

where A is a coefficient determined by the interference contrast, $A=(1/2)(I_{\max}-I_{\min})/(I_{\max}+I_{\min})$, I_0 is the intensity at the channel exit, $L=|l_1-l_2|$ is the path difference of the rays in the interferometer (l_1 and l_2 are the ray paths in the interferometer), $\tau=(l_1+l_2)n/2c$, and β is the light propagation constant in the fiber.

Formula (2) expresses the conversion of the phase modulation into intensity modulation in this fiber-optic system. Physically, the phase shift associated with τ may be attributed to a general delay of the signal as it propagates through the interferometer.

Introducing the notation

$$\varphi_0 = \beta L,$$
$$\delta\varphi = 2\,\delta\psi \sin(\Omega L n/2c), \tag{3}$$
$$\varphi = \Omega\tau,$$

expression (2) may be written as

$$I_- = I_0 A \cdot \cos[\varphi_0 + \delta\varphi \cdot \cos(\Omega t - \varphi)]. \tag{4}$$

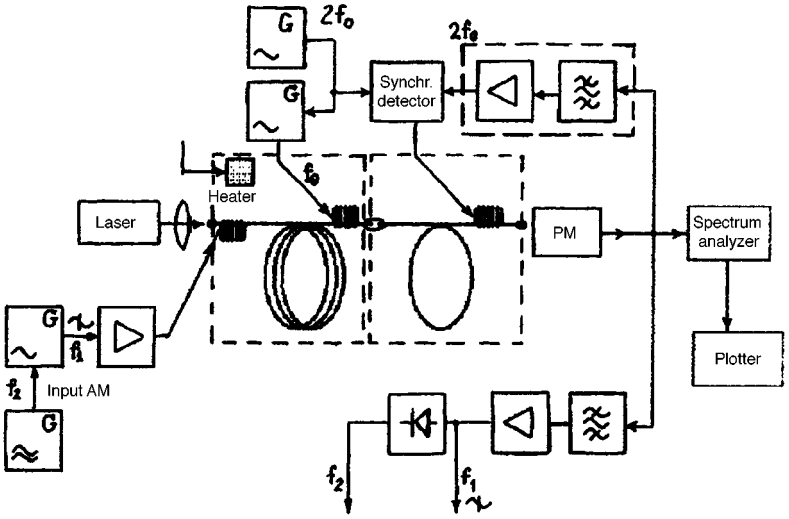

FIG. 1.

According to formula (3), the maximum efficiency for conversion of phase modulation into intensity modulation ($\delta\varphi=2\,\delta\psi$) is achieved at frequencies for which $(\Omega Ln/c)=k\pi$, where k is odd. If $(\Omega Ln/c)=k\pi$, for even k we find $\delta\varphi=0$, no information is recorded, and in particular, the interferometer signal is not influenced by phase fluctuations in the transmitting fiber at frequencies close to zero.

The structure of the signal (4) is similar to that of the signals obtained in ordinary interferometer systems, where the fiber propagation channel for the phase-modulated light is incorporated in the interference system converting the phase modulation into intensity modulation. However, with an external interferometer some differences are observed compared with conventional systems, for instance:

No influence of slow thermal drift of the light phase is observed in the transmission channel;

An ''external'' interferometer used to convert phase modulation into intensity modulation, can always be compact and isolated from perturbations;

The parameters of an ''external'' system for detection of the useful signal do not depend on the length or configuration of the propagation channel for the phase-modulated optical signal.

The modulating signal (1) can be discriminated by any method of processing the signal (4) used in fiber interferometry.[3,5–7] For example, the interferometer operating point can be stabilized at the center of the linear section, as in the experiments described subsequently. Then $\varphi_0=\pi/2$, and for $\delta\varphi\ll\pi$ we obtain at the exit

$$I_-=I_0A\cdot\cos[\varphi_0+\delta\varphi\cdot\cos(\Omega t-\varphi)]$$
$$\approx I_0A\cdot\delta\varphi\cdot\cos(\Omega t-\varphi)], \qquad (5)$$

and the photodetector directly records the information signal.

When a complicated nonharmonic information signal is fed to the modulator, it will be discriminated at the exit through the frequency characteristic $(\delta\varphi/\delta\psi)=2\sin(\Omega Ln/2c)$, as can be seen from expressions (2) and (3). If the interferometer parameters are selected so that the useful signal spectrum is concentrated near the extremum of this frequency characteristic, the signal will be recorded almost without distortion.

The apparatus used to demonstrate this method of detecting the phase modulation of optical signals is shown schematically in Fig. 1. The light source is an LGN-208B He–Ne laser ($\lambda=0.63\ \mu$m). An optical fiber having the core diameter $d=10\ \mu$m and length 100 m was used as the transmission channel for the signal phase modulation. To simplify the optical system we used a single-fiber Fabry–Perot receiving interferometer ($d=50\ \mu$m) 10 m long, with dielectric mirrors (intensity reflection coefficient $R=60\%$) deposited on the ends. This Q factor ensured enhanced interference contrast,

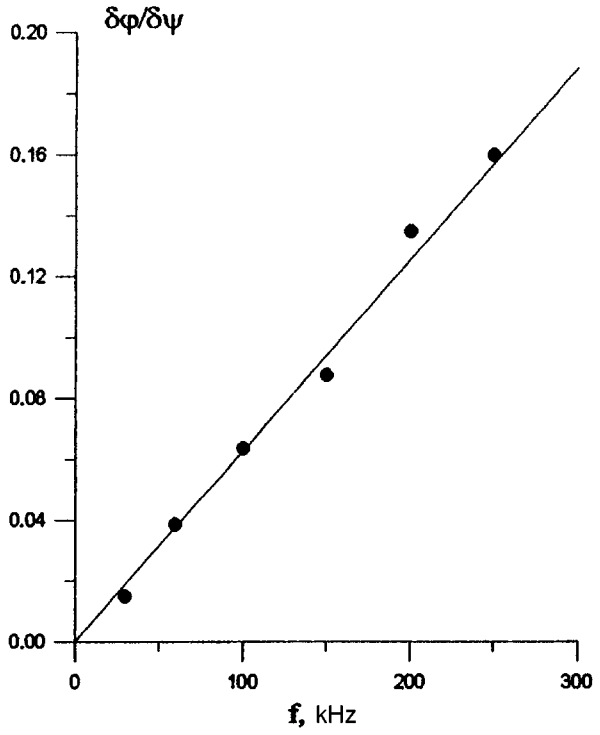

FIG. 2.

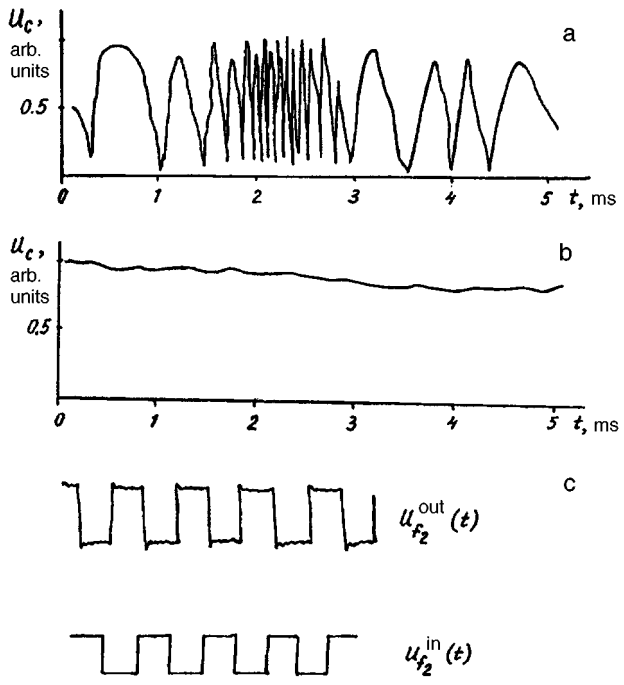

FIG. 3.

but at the same time the interferometer was similar to a two-beam type. Piezoceramic cylindrical fiber phase modulators at the transmitting fiber and the interferometer were used to modulate the phase of the optical radiation (and for compensation). This configuration could only be used to investigate the range where $(\Omega Ln/2c) \ll \pi$, i.e., the linear range of the frequency characteristic (2), and thus to detect the derivative of the modulating signal.

Figure 2 gives the experimental frequency dependence of $(\delta\varphi/\delta\psi)$. The theoretical curve for a low-Q Fabry–Perot interferometer with $L=20$ m (Fig. 2, solid curve) has the form

$$\frac{\delta\varphi}{\delta\psi} = 2 \cdot \sin(2\pi f \cdot Ln/2c) \approx 2\pi \cdot 10^{-7} \cdot f \qquad (6)$$

and shows good agreement with the experimental curve.

This apparatus was used to implement a simple interferometer stabilization system to demonstrate the transmission of signals by phase modulation and detection with an external interferometer. This stabilization was provided by additional modulation of the interferometer signal and minimizing the second harmonic of this signal at the exit by means of a feedback loop with amplification. The results presented below were obtained for an auxiliary signal frequency $f_0=30$ kHz and an information signal $f_1=500$ kHz.

Figure 3a shows the typical time drift of a 500 kHz output signal (with the interferometer stabilizing loop open). The fading of the signal is mainly caused by fluctuations of the interferometer temperature. Figure 3b shows the behavior of the 500 kHz signal after closing the stabilizing loop. Figure 3c gives oscilloscope traces demonstrating the transmission of the low-frequency signal $f_2=1$ kHz on a 500 kHz subcarrier (by amplitude modulation of the subcarrier).

To conclude, it should be noted that the proposed method of constructing extended phase-modulated measuring and transmission systems has the following advantages:

It eliminates fading of the useful signal induced by drift of the external conditions of the propagation channel for the phase modulation (inherent in other methods of constructing these systems);

No optical power is lost to stopping down (which is required in multimode systems with mode interference);

The length and configuration of the signal propagation channel does not influence the requirements for coherence of the light source, the interferometer parameters, or the methods of recording the useful signal.

[1] Yu. V. Gulyaev, M. Ya. Mesh, and V. V. Proklov, *Modulation Effects in Fiber-Optic Waveguides and Their Applications* [in Russian], Radio i Svyaz', Moscow (1991).
[2] D. E. N. Davies and S. A. Kingsley, Electron. Lett. **10**, 21 (1974).
[3] N. N. Evtikheev, É. A. Zasovin, and D. I. Mirovitskiĭ, Itogi Nauki i Tekhn. Ser. Svyaz' **8**, 24 (1991).
[4] M. Born and E. Wolf, *Principles of Optics*, 4th ed (Pergamon Press, Oxford, 1969) [Russ. transl., Nauka, Moscow, 1973].
[5] M. M. Butusov, S. L. Galkin *et al.*, *Fiber Optics and Instrument Manufacture* [in Russian], Mashinostroenie, Leningrad (1987).
[6] S. K. Sheem, T. G. Giallorenzi, and K. Koo, Appl. Opt. **21**, 689 (1982).
[7] J. Dakin and B. Kalsho, *Fiber-Optic Sensors: Principles and Components* [Russ. transl., Mir, Moscow, 1992].
[8] P. R. Ball and B. Culshaw, Electron. Lett. **16**, 259 (1980).
[9] B. Culshaw, P. R. Ball, J. C. Pond, and A. A. Sadler, Electron. Power **11**, 148 (1981).
[10] P. R. Ball, B. Culshaw, and S. A. Kinglsey, Proc. SPIE **232**, 216 (1980).
[11] V. A. Ivanov and V. E. Privalov, *Applications of Lasers to High-Precision Mechanical Devices* [in Russian], Politekhnika, St. Petersburg (1993).

Translated by R. M. Durham

Alternation of nonequilibrium and sequences of structural transitions

G. E. Skvortsov

St. Petersburg State University
(Submitted January 20, 1997)
Pis'ma Zh. Tekh. Fiz. **23**, 17–21 (May 26, 1997)

An analysis is made of the law of alternating nonequilibrium, dictating an oscillatory change in the degree of nonequilibrium for a wide range of influence. With increasing influence, intervals of decreasing degree of nonequilibrium at their onset correspond to structural transitions and accompanying anomalous states. This law can be used to identify a wide variety of new nonequilibrium effects. © *1997 American Institute of Physics.* [S1063-7850(97)02005-3]

Alternation of nonequilibrium together with structural conditionality, the qualitative boundary, and abnormality,[1–3] form a set of fundamental relations that can be used to describe the qualitative behavior of a wide range of systems exposed to different types of influences. Sequences of structural transitions and in particular, energy conversion and conversion cycles, as well as an abundance of accompanying nonequilibrium effects, are directly associated with this relationship.

1. The law of alternating nonequilibrium may be expressed as follows: when a system is exposed to a uniformly increasing influence, the measured deviation from equilibrium varies in an alternating fashion, a natural increase being replaced by a decrease, a decrease giving way to an increase, and so on, until the system is destroyed.

Moreover, the points (or intervals) of variation in the behavior of the degree of nonequilibrium correspond to structural transitions and thus with increasing influence a sequence of structural transitions takes place, with regimes of considerably lower nonequilibrium between them.

For fairly extended, highly nonequilibrium systems, spatial and temporal sequences of structural transitions are observed, with intervals of weak nonequilibrium between them.

Any system consists of a hierarchy of subsystems, and since the degree of nonequilibrium has different values for the system and its subsystems, the law of alternating nonequilibrium may be considered as a repeated ''exchange of nonequilibrium'' between the system and its subsystems.

We shall demonstrate these three hypostases of alternating nonequilibrium using examples of typical sequences of structural transitions.

The most numerous quasiequilibrium sequence of structural transitions induced by uniform heating comprise quantum-type transitions for $T<\theta_D$ (Ref. 4), domain–diffusion transitions, melting, liquid-structural transitions, evaporation, dissociation, and plasma formation. A more detailed analysis of first-order transitions, such as melting and evaporation, reveals that they are three-stage processes, and also reveals the existence of a nonuniform, nonsteady-state, transient structure (fluctons). These pre-transition, transition, and post-transition stages may each be considered to be second-order transitions. Then, in these second-order structural transitions, three stages can be isolated by corner points,[5] and these should be assigned to third-order structural transitions.

The three hypostases of alternating nonequilibrium are manifested even more clearly for a sequence of structural transitions of nonequilibrium origin. Examples include: a sequence of structural transitions $(l/\Delta T_+)$ caused by an increase in the temperature difference at the interfaces of liquids: Bénard regimes, three boiling crises (Ref. 6, p. 158); a sequence of structural transitions (F_+): formation of striations and Gunn domains, and the sequence (g/V_+): subsonic to supersonic transition, anomalous relaxation regimes in gases.[7,1,8] In this last case, alternation of nonequilibrium is observed particularly clearly for CO_2.

2. The degree of nonequilibrium is defined by the set of quantities[2]

$$GS{:}V=\left|\frac{u}{V_{\mathrm{T}}}\right|,\quad E_i=\left|\frac{e}{\mathrm{E}_i}\right|,\quad J_n=\left|\frac{j_n-j_{ne}}{j_{ns}}\right|,\ldots,$$

$$F_i=\left|\frac{\tau_i f}{m v_{\mathrm{T}}}\right|,\ldots$$

$$W_{ni}=\tau_i|\partial_t \ln a_n|,\quad H_{ni}=\lambda_i|\partial_x \ln a_n|,\ldots \tag{1}$$

using the notation from Ref. 2.

According to the law of alternating nonequilibrium, the values of GS decrease in the supercritical neighborhood of the structural transitions, and then increase as far as the structural transition regime, and so on.

The first quantity — the local Mach number for $v_{\mathrm{T}}=v_s$ (where v_s is the velocity of sound) — indicates a subsonic to supersonic transition, which varies discontinuously from $M>1$ ahead of the shock wave to $M<1$ in the perturbed gas. The jump and the inverse transition $M<1\rightarrow M>1$ demonstrate the relation for steady-state flow in a planar channel with variable width $l(x)$ in the form of a nozzle:

$$H_u\equiv\frac{l}{u}\frac{du}{dl}=\frac{1}{M^2-1},\quad M=M(l). \tag{2}$$

The second, energy-related quantity (1.2) may be analyzed for a gas–liquid transition using the van der Waals equation of state, as in Ref. 9. In this case, a decrease in $(pdv/\mathrm{E}_{\mathrm{evap}})$ is observed in the metastable region and it is also possible for a rarefaction wave to propagate.[6]

The flux quantity (1.3) may be analyzed using experimental data on the heat flux $q(\Delta T)$ for boiling crises (Ref. 6, p. 158).

 1063-7850/97/050383-02$10.00

In general, as in the examples, the dependence of the determining quantity $J(g)$ on the action factor g has a typical N-shaped form, where the corner points (really rounded) correspond to structural transitions, the first and second ascending sections correspond to regimes with slowly varying structures S_1 and S_2, and the descending section corresponds to an anomalous regime with a transient metastable structure. A general sequence of structural transitions is schematically composed of N-shaped elements by means of a continuation of the first element.

A suitable characteristic describing the properties and state of a system is the set of susceptibilities $K_{nm}=\partial J_n/\partial g_m$: constant positive values correspond to weakly nonequilibrium regimes, jumps correspond to structural transitions, and zero and negative values correspond to metastable states. In the last case, the system clearly absorbs a considerable fraction of the ''supply of g'' for rearrangement of the structure from s_1 to s_2.

3. A fairly general schematic model of the law of alternating equilibrium may be given by the ''barrier resonance'' model, which is based on the following natural assumptions.

The system under study possesses a hierarchical dynamic structure and is described by a sequence of sets of five quantities:

$$\{\lambda_s,\tau_s,\varepsilon_s,m_s,n_s\},\quad \lambda_s>\lambda_{s+1},\quad \tau_s>\tau_{s+1},$$
$$\varepsilon_s<\varepsilon_{s+1},\quad m_s>m_{s+1},\quad n_s<n_{s+1}(s=0,1,2,\ldots), \tag{3}$$

denoting, respectively, the characteristic dimension, time, interaction (coupling) energy, mass, and number density of the structure-kinetic elements of the s-level ($s=0$ refers to the entire system).

The initial structure model used[1,2] had two levels.

The hierarchy of the structure is observed under a uniformly increasing external influence as a systematic overcoming of energy barriers — coupling of substructures as far as level s in accordance with the criterion $e=\varepsilon_1+\ldots+\varepsilon_s$, where e is the energy acting on the main structure-kinetic element. Quasiequilibrium phase transitions take place as a barrier process.

When an external influence (ω,k) is periodic in space and time, a corresponding structural transition takes place resonantly when the equalities $\omega\tau_s,k\lambda_s=2\pi$ are satisfied for fairly large amplitude. An example may be the transition of a molecular gas to a liquid near the triple point when exposed to radiation at a frequency in resonance with the first electronic excitation energy and, with increasing radiation intensity, the transition of the liquid to the solid state (with special properties).

4. The law of alternating equilibrium, formulated with the condition of increasing influence, may be supplemented by including the conditions of decrease (with natural refinements). Of course, the combined formulation does not imply that the sequences of $(+)$ and $(-)$ structural transitions are similar. Moreover, it may be stated that the ''direct'' $(+)$ structural transitions do not usually coincide with the ''reverse'' $(-)$ transitions when these take place at nonzero rates. Their differences and the scope for controlling the corresponding regimes make it possible to obtain energy conversion cycles considerably more efficient than the quasiequilibrium (Carnot) cycles. The plasma–ion electrolysis of water is one such process.[10]

5. We indicate some applications of the law of alternating nonequilibrium and the barrier-resonance model of structural transitions.

5.1. The existence of intervals of weak nonequilibrium under a strong influence allows quasiclassical theory to be applied and thereby substantially enlarges its range of validity. This circumstance has initiated the development of efficient technologies utilizing ''quasiequilibrium windows,'' as has been achieved for a dye laser.[11]

5.2. The generality of the barrier mechanism means that under suitable conditions the sequence of structural transitions for one material and one specific influence may be used as the basis to predict the existence and form of the sequence of structural transitions for other materials and other influences. For instance, the quasiquantum sequence of structural transitions (T_+) (Ref. 4) can be related to a sequence of structural transitions (σ_+) of abrupt deformations.[12] The barrier criterion[1,3] is used as the basis to predict anomalous relaxation regimes for numerous monatomic, diatomic, and triatomic gases.

5.3. The resonance mechanism of structural transitions indicates that resonance pulse technologies may be used. In particular, this mechanism was used as the basis to achieve laser cutting of biopolymers without carbonization.

[1] G. E. Skvortsov, Pis'ma Zh. Tekh. Fiz. **16**(17), 15 (1990) [Sov. Tech. Phys. Lett. **16**, 1647 (1990)].
[2] G. E. Skvortsov, Pis'ma Zh. Tekh. Fiz. **23**(6), 85 (1997) [Tech. Phys. Lett. **23**, 647 (1997)].
[3] G. E. Skvortsov, Pis'ma Zh. Tekh. Fiz. **23**(7), 23 (1997) [Tech. Phys. Lett. **23**, 246 (1997)].
[4] *Systems of Singular Temperature Points of Solids* [in Russian], Nauka, Moscow (1986).
[5] A. P. Smirnov, *ibid*, pp. 210–239.
[6] S. S. Kutateladze, *Analysis of Similarity and Physical Models* [in Russian], Nauka, Leningrad (1986).
[7] G. E. Skvortsov, Pis'ma Zh. Tekh. Fiz. **9**, 744 (1983) [Sov. Tech. Phys. Lett. **9**, 320 (1983)].
[8] G. I. Mishin, A. P. Bedin, N. I. Yushchenkova, G. E. Skvortsov, and A. P. Ryazin, Zh. Tekh. Fiz. **51**, 2315 (1981) [Sov. Phys. Tech. Phys. **26**, 1363 (1981)].
[9] Ya. B. Zel'dovich, Zh. Éksp. Teor. Fiz. **16**, 363 (1946).
[10] Yu. A. Beklemegiev, *Abstracts of Papers presented at the International Conference on New Ideas in Natural Science*, St. Petersburg, 1996 [in Russian], p. 3.
[11] G. A. Vestnicheva and A. Yu. Ivanov, Zh. Tekh. Fiz. **64**(1), 201 (1994) [Tech. Phys. **39**, 114 (1994)].
[12] L. N. Zagoruĭko, A. N. Osetskiĭ, and V. P. Soldatov, Fiz. Met. Metalloved **43**, 1079 (1977).

Translated by R. M. Durham

p-GaSe–n-Ga_2S_3 heterojunctions

M. Z. Kovalyuk, V. I. Vitkovskaya, and M. V. Tovarnitskiĭ

Branch of the Institute of Problems in Materials Science, National Academy of Sciences of Ukraine, Chernovtsy

(Submitted December 2, 1996)
Pis'ma Zh. Tekh. Fiz. **23**, 22–24 (May 26, 1997)

Epitaxial layers of n-Ga_2S_3 have been grown on p-GaSe single crystals annealed in sulfur vapor. The possibility of fabricating p-GaSe–n-Ga_2S_3 heterojunctions is demonstrated. © *1997 American Institute of Physics.* [S1063-7850(97)02105-8]

Photosensitive structures have been fabricated using III–VI layered single crystals (GaSe, InSe, and GaTe).[1–3] In the present paper we develop a new method[4] of fabricating these structures using GaSe single crystals grown by the Bridgman method. The crystals exhibited good lamination and a specular surface and did not require additional treatment. The majority carrier concentration was $p \cong 10^{15}$ cm^{-3} and the mobility was $\mu_p \cong 40$ $cm^2/V \cdot s$ at room temperature. Samples of GaSe of specific dimensions were placed in a quartz ampoule containing sulfur and were evacuated to 10^{-6} Torr. The samples were annealed in the sulfur vapor at temperatures of 400–500 °C for 10 h. After this procedure, the base regions of the GaSe were a dark yellow color.

The samples were then subjected to x-ray diffraction analysis using an IRIS-0 system with Cr K_α radiation, which revealed that a single-crystal Ga_2S_3 film with lattice parameters $a = 6.22 \pm 0.03$ Å and $c = 17.74 \pm 0.05$ Å had formed on the surface of the GaSe crystals.

The x-ray diffraction patterns of the GaSe single crystals annealed in sulfur vapor differ depending on the treatment conditions. As the annealing temperature is increased from 400 to 500 °C, the x-ray diffraction patterns reveal additional reflections in the form of Debye rings, as well as the main reflections of the GaSe phase. Figure 1 shows an x-ray diffraction pattern from a GaSe⟨S⟩ sample annealed at 500° for 10 h. Intense Debye rings of the Ga_2S_3 phase can be clearly identified together with the single-crystal reflections of the main GaSe phase. The Ga_2S_3 crystal lattice is oriented relative to the substrate like $\{001\}$ $Ga_2S_3 \| \{001\}$GaSe.

Annealing of gallium selenide single crystals in sulfur vapor is accompanied by heterovalent substitution of selenium by sulfur.

It has been established that the thickness of the Ga_2S_3 film may vary fairly widely and that the rate of formation of the film is 0.35 μm/h. The Ga_2S_3 layers were invariably n-type, the majority carrier concentration was $n = 5 \times 10^{16}$ cm^{-3} and their mobility was $\mu_n = 25$ $cm^2/V \cdot s$ at room temperature.

This Ga_2S_3 film obtained on a single-crystal GaSe semiconductor can be used to fabricate a p-GaSe–n-Ga_2S_3 heterostructure. According to Ref. 5, the band gap of Ga_2S_3 is $E_g = 2.7$ eV, so that Ga_2S_3 can be used as the ''window'' of a p-GaSe–n-Ga_2S_3 heterostructure.

An investigation of the current-voltage characteristics showed that the forward currents are 10^2 times greater than the reverse currents.

Figure 2 shows the spectral characteristic of this structure. The low-energy photoresponse threshold is attributed to the absorption edge of GaSe while the short-wavelength cutoff corresponds to the band gap of Ga_2S_3.

[1] M. Di Giulio, G. Micocci, A. Rizzo, and A. Tepore, J. Appl. Phys. **54**, 5839 (1983).
[2] V. L. Bakumenko and V. F. Chishko, Fiz. Tekh. Poluprovodn. **11**, 2000 (1977) [Sov. Phys. Semicond. **11**, 1171 (1977)].
[3] V. N. Katerinchuk and M. Z. Kovalyuk, Pis'ma Zh. Tekh. Fiz. **18**(12), 70 (1992) [Sov. Tech. Phys. Lett. **18**, 394 (1992)].
[4] M. V. Tovarinitskiĭ, V. K. Luk'yanyuk, Z. D. Kovalyuk, V. I. Vitkovskaya, and S. Ya. Golub, Pis'ma Zh. Tekh. Fiz. **14**, 2104 (1988) [Sov. Tech. Phys. Lett. **14**, 914 (1988)].
[5] V. I. Gavrilenko, A. M. Grekhov, D. V. Korbutyak, and G. G. Litovchenko, *Optical Properties of Semiconductors* [in Russian], Naukova Dumka, Kiev (1987).

Translated by R. M. Durham

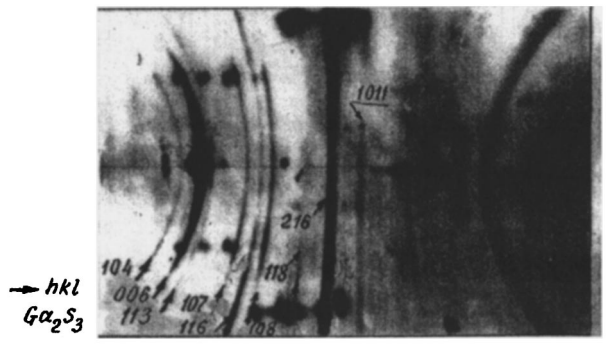

FIG. 1. Oscillating-crystal x-ray photograph of a GaSe⟨S⟩ sample; annealing temperature 500 °C and annealing time 100 h.

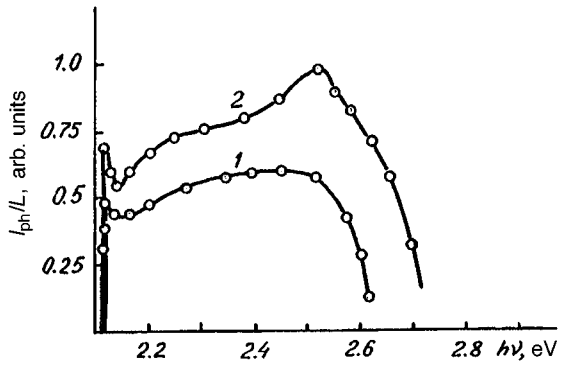

FIG. 2. Spectral characteristic of the quantum efficiency of a n-Ga_2S_3–p-GaSe heterostructure (*1* — 295 K and *2* — 80 K).

 1063-7850/97/050385-01$10.00

Mechanism of electrode erosion in pulsed discharges in water with a pulse energy of ~1 J

V. L. Goryachev, A. A. Ufimtsev, and A. M. Khodakovskiĭ

Institute of Problems in Electrophysics, Russian Academy of Sciences, St. Petersburg
(Submitted July 18, 1996)
Pis'ma Zh. Tekh. Fiz. **23**, 25–29 (May 26, 1997)

It has been shown that electrode erosion in pulsed discharges in water is governed by a thermal cavitation effect. Blowing gas through the water modifies the cavitation effect, simplifies breakdown, and allows solid electrodes to be used.
[S1063-7850(97)02205-2]

An electric discharge in liquids is widely used in various types of technologies involving pulsed mechanical treatment. Recently, the properties of an electric discharge in water have been used to purify it.[1] The commercial application of this property is largely hindered by the lack of an electric-discharge chamber design with a long electrode operating life. The operating life of the electrodes is limited by erosion, and this particularly applies to a point electrode (anode) initiating a discharge in a point–plane configuration.

In the present paper we report results of an investigation into the mechanism of electrode erosion in pulse-periodic discharges in water at low pulse energies ($\leqslant 1$ J). The apparatus and method of measuring the main discharge parameters were described in Ref. 1. The discharge pulse length varied between 20 and 200 μs and the pulse repetition frequency was ~50–100. The peak current was ~25–30 A and the voltage drop across the discharge gap was ~1000 V. Two types of electrodes were used: 1 mm diameter wire electrodes, projecting into the water to a distance of 1.5–2 mm from the insulating wall, and 10 mm diameter rod electrodes, projecting to 10 mm.

It is well known[2,3] that a point anode considerably facilitates the pulsed breakdown of a liquid by reducing the breakdown voltage. This is because current is concentrated near the electrode, causing local overheating of the liquid near the anode surface, which leads to the formation of an initial breakdown stage in the form of a gas microbubble. When solid rod electrodes are used, this process is initiated by blowing gas through a 1.3 mm diameter hole.

The degree of erosion of the wire electrodes was determined from the reduction in the height of the protruding part of the electrode with time, while that of the solid rods was determined by weighing. To improve the accuracy of the measurements, the electrode operating time was at least 100 h. The materials used for the point electrodes were copper, steel, brass, molybdenum, and tungsten, and for the solid rod electrodes, copper, steel, and alloys containing tungsten and molybdenum. The surface state of the electrodes after operation was examined under an electron microscope. The surface was photographed at magnifications of 15, 200, 350, and 500. Qualitative conclusions on the nature of the damage to the electrode surface could be drawn from these photographs.

The main results were as follows:

1. For the same materials and with the same pulse length and repetition frequency, the erosion of the point (wire) electrodes was an order of magnitude greater. For example, the specific erosion (α) of the copper electrodes was $\sim 4\times 10^{-7}$ kg/s for a point electrode and $\sim 2.5\times 10^{-8}$ kg/s for a solid electrode. For steel the specific erosion was $\sim 1.5\times 10^{-7}$ kg/s for a point electrode and $\sim 3.6\times 10^{-8}$ for a solid electrode.

2. An increase in the pulse length (τ) increases the specific erosion, the dependence being almost linear (see Table I).

3. For point electrodes, the erosion depends on the mechanical properties of the material, whereas for solid electrodes, it is almost independent of these properties.

We now discuss these results.

Erosion of the electrode surface in a pulsed discharge in water, as in arc spots on cold electrodes, is mainly caused by current heating. The average spot diameter is determined experimentally by a signature method (erosion tracks). A characteristic feature of a discharge in water, as compared with a gas discharge, is the formation of a microbubble at the surface of a point electrode, which then cavitates. There is a specific probability that this process may take place at the electrode surface. When bubbles are created artificially, breakdown may be initiated by these bubbles[3] and cavitation then has a negligible influence on the erosion. In qualitative terms, this explains why, under the same conditions (current and voltage, size of arc spots), the erosion of point electrodes is an order of magnitude greater than that of solid electrodes with gas blowing. This conclusion is also supported by photographs of the electrode surface. The craters on the surface of the point electrodes are deeper and traces of liquid metal spraying can also be identified. This is not observed for the solid electrodes.

Two mathematical models were analyzed to obtain quantitative estimates of the observed behavior.

The first model describes thermal erosion from the surface of an arc spot.[4] The erosion from the surface of the spot was determined by numerically solving the nonsteady-state heat conduction equation, with allowance for phase transitions for a given energy flux density. The energy flux density was inferred from experimental oscilloscope traces of the voltage and current. The spot radius was determined by the signature method. The erosion was calculated as the integral

TABLE I.

Material	α, kg/s	τ, μs
Copper	4×10^{-7}	20
	1.4×10^{-6}	200
Steel	1.5×10^{-7}	20
	1×10^{-6}	200

TABLE II. Erosion per pulse.

Material	Erosion, kg, experiment	Erosion, kg, calculated
Copper	1×10^{-11}	5.5×10^{-12}
Steel	2×10^{-11}	5×10^{-12}
Tungsten	2×10^{-11}	9.4×10^{-12}

of the flux density of the vaporizing atoms over the time of action of the pulse. The flux density of the vaporizing atoms is given by:

$$I=P_0\sqrt{m/(2\pi kT)}kTQ^{-1}(1-\exp(-Q/(kT))),$$

where P_0 is the saturation vapor pressure, m is the mass of a metal atoms, and Q is the heat of evaporation per atom. This formula is similar to that given in Ref. 5.

The main results may be summarized as follows:

— During the action of the pulse, the region $\sim(\lambda\tau/(\rho C_p))^{1/2}$ is heated over its depth, where λ is the thermal conductivity of the material, ρ is the density of the material, C_p is the specific heat, and τ is the pulse duration;

— During the same time, the surface temperature for all the materials (copper, steel, and tungsten) reaches the boiling point. For copper and steel this time is ≈3 μs, and for tungsten it is ≈10 μs;

— After the boiling point has been reached, the erosion increases linearly with time.

Some results of calculations of the erosion are presented in Table II.

Considering that the results of the calculations depend in many respects on defining the spot dimensions and the near-electrode breakdown voltage, the agreement with the experiment may be regarded as satisfactory — this particularly applies to the comparative erosion characteristic of copper and tungsten.

The influence of gas bubbles on the electric field distribution in the liquid was considered using the following model. A spherical cavity (gas bubble) is located in an infinite, poorly conducting medium (water). The external electric field is uniform. The dielectric and conducting properties of the medium and the bubble generally differ. It follows from the calculations that at the prebreakdown stage, where the electrical conductivity inside the bubble is almost zero, the field outside the bubble is attenuated while that inside the bubble is intensified: $E=3E_0\varepsilon/(1+2\varepsilon)\approx1.5E_0$, where $\varepsilon=\varepsilon_w/\varepsilon_g$, and ε_w and ε_g are the relative permittivities of water and the gas in the bubble, respectively, and E_0 is the external field strength.

Thus when bubbles are present in the water, there is a high probability of breakdown and streamer generation in the gas bubble. This implies that there is almost no cavitation effect on the electrode surface, and the erosion for a solid electrode with gas blowing is substantially less than that for a point electrode without gas blowing.

To sum up, the main conclusions are as follows:

1. Erosion of electrodes in pulsed discharges in water is determined by two effects: thermal and cavitation.

2. The cavitation effect may be suppressed substantially by blowing gas through an aperture in the electrode.

3. Gas blowing allows solid electrodes to be used, since breakdown is initiated by the gas bubbles at the same or even lower breakdown voltages.

[1] V. L. Goryachev, F. G. Rutberg, and V. N. Fedyukovich, Teplofiz. Vys. Temp. No. 5 (1995), *in press*.

[2] V. V. Krivitskiĭ, *Dynamics of Electrical Explosions in Liquids* [in Russian], Naukova Dumka, Kiev (1986).

[3] S. M. Korobeĭnikov and É. V. Yanshin, *Bubble Model of Discharge Ignition in a Liquid with Pulsed Voltage. Electrical Discharge in Liquids and Its Industrial Application*, Part I [in Russian], Nikolaev (1988).

[4] V. L. Goryachev and A. N. Khodakovskiĭ, ''Model of electrode erosion in a plasmotron,'' *Proceedings of the Conference on the Physics of Low-Temperature Plasmas*, Petrozavodsk, 1995, Part 2 [in Russian], p. 186–188.

[5] V. M. Smirnov, Usp. Fiz. Nauk. **164**, 665 (1994).

Translated by R. M. Durham

Characteristics of the formation of a resistive zone in spatially bounded multiple-wire superconducting current-carrying elements

A. N. Balev and V. R. Romanovskiĭ

''Kurchatov Institute'' Russian Science Center, Moscow
(Submitted December 26, 1996)
Pis'ma Zh. Tekh. Fiz. Pis'ma Zh. Tekh. Fiz. **23**, 30–36 (May 26, 1997

An analysis is made of possible mechanisms for the propagation of a normally conducting zone in a superconducting multiple-wire current-carrying element spatially bounded in one direction. It is shown that irreversible growth of the resistive zone is characterized by the formation of a flattened front propagating in the spatially unbounded direction. © *1997 American Institute of Physics.* [S1063-7850(97)02305-7]

The formation of a local region of normal conduction in a superconducting magnet system may lead to an irreversible transition to the normal state. The accompanying electrical voltage developed inside the winding and the temperature rise may be very substantial, and may even destroy the magnet. Thus, protective measures to ensure accident-free operating conditions are required to eliminate unfavorable effects in a superconducting magnet system.

The model of a continuous medium, specifically the model of an expanding ellipsoid, is widely used for theoretical analyses of transient processes in a superconducting magnet system.[1–3] According to this model, the axes of the ellipsoid are formed by the velocity vectors of the normal zone propagating from turn to turn and from layer to layer. This approach can be applied without modification to the case where the growth of the heat-generating zone is limited in some spatial dimension because of the finite dimensions of a real winding.[3] However, these approximations neglect the influence of edge effects on the formation of the resistive zone once this reaches the external boundary. In the present paper we therefore analyze possible mechanisms for the propagation of a normally conducting zone in a superconducting multiple-wire current-carrying element having bounded spatial dimensions in one particular direction.

We shall determine the change in temperature T_k in a rectilinear uncooled composite of N thin superconducting wires in contact along a given perimeter, by solving a system of quasiconjugate equations

$$C_k\frac{\partial T_k}{\partial t}=\frac{\partial}{\partial x}\left(\lambda_k\frac{\partial T_k}{\partial x}\right)+\frac{I^2}{S_k^2}\rho(T_k)-\begin{cases}\dfrac{p_1}{S_1R_1}(T_1-T_2), & k=1\\ \dfrac{p_{k-1}}{S_kR_{k-1}}(T_k-T_{k-1})+\dfrac{p_k}{S_kR_k}(T_k-T_{k+1}), & k=\overline{2,\,N-1}\\ \dfrac{p_N}{S_NR_N}(T_N-T_{N-1}), & k=N\end{cases}$$

with the initial/boundary conditions

$$T_k(x,0)=\begin{cases}T_1, & 0<x<x_0, \quad k=k_i, \quad i=1,2,\ldots\\ T_0, & x_0\leqslant x\leqslant l, \quad k=k_i\\ T_0, & 0\leqslant x\leqslant l, \quad k\neq k_i\end{cases}$$

$$\frac{\partial T_k}{\partial x}(0,t)=0, \quad T_k(l,t)=T_0.$$

Here $k=1,\ldots,N$ is the wire number in the composite, C_k is the volume specific heat of the kth element, λ_k is its thermal conductivity in the longitudinal direction, S_k is the cross-sectional area, p_k is the contact perimeter between two adjacent wires, R_k is the thermal contact resistance, I is the transport current in each wire, T_0 is the coolant temperature, T_1 is the temperature of a thermal perturbation with the initial extent x_0, $\rho(T_k)$ is the effective electrical resistivity of the composite, assuming a region of current division between sections in the superconducting and normal states in the kth wire[2,3]

$$\rho(T_k)=\rho_0(T_k)\times\begin{cases}1, & T_k>T_{CB}\\ \dfrac{T_k-T_C}{T_{CB}-T_C}, & T_C\leqslant T_k\leqslant T_{CB}\\ 0, & T_k<T_C=T_{CB}-(T_{CB}-T_0)\dfrac{I}{I_C}\end{cases},$$

where ρ_0 is the electrical resistivity of the matrix, and I_C, T_C, and T_{CB} are the critical parameters of the superconductor.

The problem as formulated describes the symmetric propagation of heat relative to the origin in a multiple-wire current-carrying element consisting of superconducting composite wires. Heat propagates as a result of a fairly powerful thermal perturbation ($T_1>T_C$), inducing the instantaneous transition of a local section of the current-carrying element to the normal state. Then the thermal interaction between the wires is described by a model assuming a steady-state linear temperature distribution in the contact zone, which is correct for thin insulation.[4] This system of equations was solved by a finite-difference method.[5] For the calculations the initial parameters were assumed to be[6]

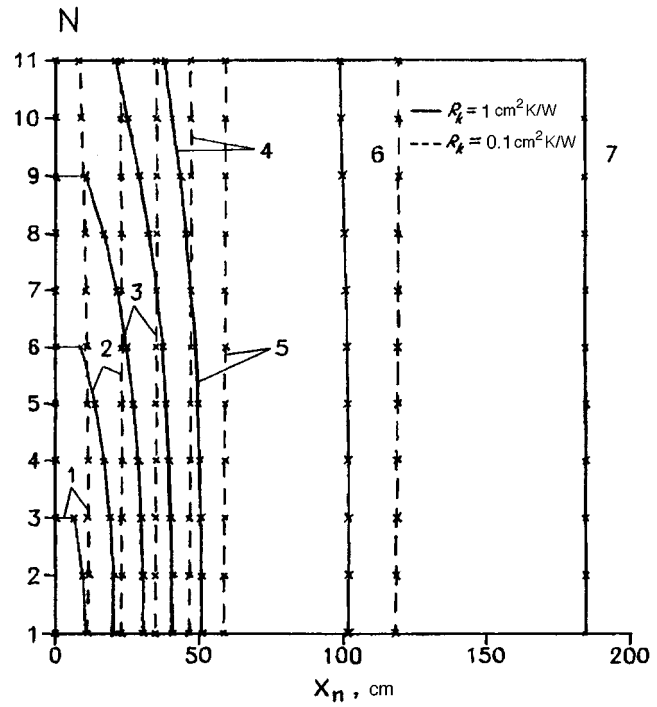

FIG. 1. Boundary of the resistive zone as a function of time $T_k(x_n,t)=T_{CB}$ for a current-carrying element bounded in the transverse direction: *1* — $t=0.01$ s, *2* — $t=0.02$ s, *3* — $t=0.03$ s, *4* — $t=0.04$ s, *5* — $t=0.05$ s, *6* — $t=0.1$ s, and *7* — $t=0.18$ s.

$$C_k(T)\left[\frac{\mathrm{J}}{\mathrm{cm^3K}}\right]$$

$$=10^{-6}\begin{cases}104T^{2.5}-197T, & 4.2\,\mathrm{K}\leqslant T<10\,\mathrm{K}\\ 366T^{2}+180T, & 10\,\mathrm{K}\leqslant T<40\,\mathrm{K}\\ 25.5T^{4.02-0.35\ln T}, & 40\,\mathrm{K}\leqslant T<300\,\mathrm{K}\end{cases}$$

$$\rho_0(T)[\Omega\cdot\mathrm{cm}]=2.93\times10^{-8}$$

$$\times\begin{cases}0.968+0.0076T, & 4.2\,\mathrm{K}\leqslant T<20\,\mathrm{K}\\ 1.71\times10^{9}T^{2.35\ln T-14.1}, & 20\,\mathrm{K}\leqslant T<35\,\mathrm{K}\\ 8.8\times10^{-4}T^{2.2}+0.12, & 35\,\mathrm{K}\leqslant T\leqslant100\,\mathrm{K}\\ 0.37T-14.8, & T>100\,\mathrm{K}\end{cases}$$

$$\lambda_k(T)=2.45\times10^{-8}\frac{T}{\rho(T)},\ \left[\frac{\mathrm{W}}{\mathrm{cm\cdot K}}\right]$$

$I=500$ A, $x_0=1$ cm, $k_i=1$, $p_k=0.01$ cm,

$S_k=1.13\times10^{-2}$ cm^2,

$T_0=4.2$ K, $T_1=10$ K, $T_{CB}=9.5$ K, $T_C=6.2317$ K.

These parameters describe the thermophysical and electrophysical properties of a current-carrying element made up of niobium titanium superconductors in a copper matrix.

Figures 1 and 2 give the results of numerical analyses simulating the formation and propagation of a heat-generating zone in multiple-wire current-carrying elements bounded either in the transverse (Fig. 1) or in the longitudinal (Fig. 2) directions, assuming that the normal zone is initiated in an outer wire of the composite. In the first case, we analyzed a ''long'' current-carrying element with relatively few wires ($l=400$ cm , $N=11$) while in the second case, we considered a ''short'' current-carrying element with a relatively large number of wires ($l=50$ cm, $N=51$). This eliminated any influence of the transverse edge effect on the formation of normal sections in the current-carrying element. The thermal resistance between the wires was varied.

These results clearly demonstrate the qualitative features of the edge effects in the formation of the boundary separating the superconducting and normal zones of the current-carrying element. Their distinguishing feature is that, after the boundary has reached the corresponding edge section of the current-carrying element, it flattens out and begins to propagate in the unbounded direction. When the heat-generating zone is bounded by a small number of wires, the boundary flattens out faster, the better the conditions of heat exchange between the wires. If the longitudinal dimension of the current-carrying element is bounded, as in the turns of a superconducting magnet system, a corresponding change in the formation and propagation of the resistive sections will be particularly noticeable in a current-carrying element with elevated thermal resistance between the elements.

These characteristics should be taken into account when calculating the total resistance of the resistive zone, on whose value depends the accurate determination of the current decay in a circuit consisting of resistive-inductive sections of current-carrying element. In the first case, after a common heat-generating zone has been formed over the entire cross section of the current-carrying element, the longitudinal growth can be accurately approximated by a model of

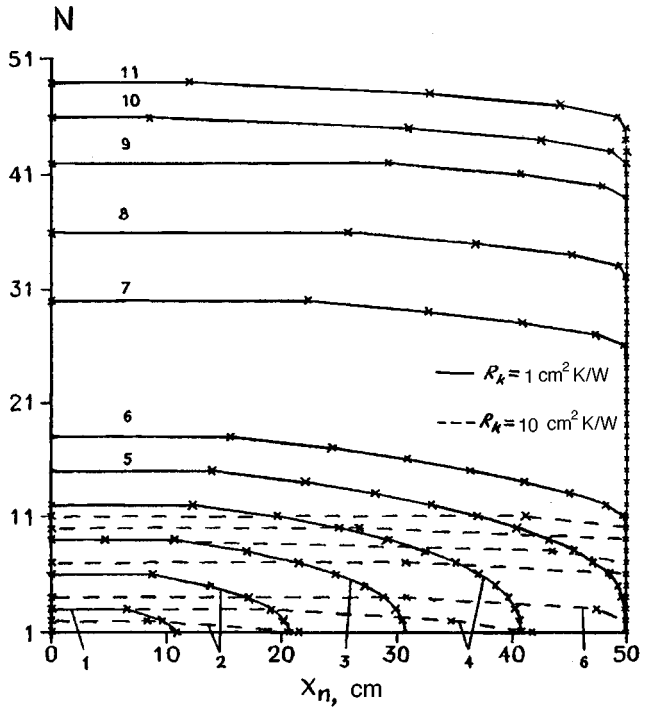

FIG. 2. Influence of longitudinal spatial limitation on the formation of the resistive zone: *1* — $t=0.01$ s, *2* — $t=0.02$ s, *3* — $t=0.03$ s, *4* — $t=0.04$ s, *5* — $t=0.05$ s, *6* — $t=0.06$ s, *7* — $t=0.1$ s, *8* — $t=0.12$ s, *9* — $t=0.14$ s, *10* — $t=0.15$ s, and *11* — $t=0.16$ s.

a heat-generating rod with a continuously growing resistive zone. It should be borne in mind that, as can be seen from Fig. 1, the propagation velocity of this zone depends not only on the conditions of heat exchange between the wires but may even increase with decreasing thermal resistance. This factor is neglected in the model of a propagating ellipsoid since this is based *a priori* on the velocity of irreversible propagation of the normal zone, calculated for a single wire.[3]

For longitudinally bounded current-carrying elements, the growth of the resistive zone after it has reached the end section will depend on two characteristic times: the time t_x for propagation of the normal zone in the longitudinal direction and the time t_k taken to heat the wire to above-critical temperature. Taking as the simplest estimates $t_x \sim l/v_x$ and $t_k \sim C_k S_k R_k / p_k$, where $v_x = (\lambda_k \rho_0 I_C^2 / C_k^2 S_k^2 (T_{CB} - T_0))^{1/2}$ is the characteristic propagation velocity of the normal zone along a single filament,[7] for $t_x \ll t_k$ the heat-generating zone will obviously also have a planar front. In real superconducting windings, this estimate will correspond by a large margin to the given mechanism for formation of the resistive zone, since the temperatures of the end sections of the turns, assumed to be equal to the coolant temperature in this model, will not only exceed this value but will also increase steadily because of the continuous multiturn nature of the current-carrying elements. As a result, continuously forming sections of normal conductivity will merge together to form a continuous nucleus.

To conclude, this investigation has shown that irreversible growth of the resistive zone in a multiple-wire superconducting current-carrying element, bounded in any one spatial dimension, is characterized by the formation of a flattened front propagating in the unbounded direction.

This work was supported by the Russian Fund for Fundamental Research (Project No. 96-02-16122a).

[1] Z. J. J. Stekly, Adv. Cryogen. Eng. **8**, 585 (1963).
[2] V. A. Al'tov, V. B. Zenkevich, M. G. Kremlev, and V. V. Sychev, *Stabilization of Superconducting Magnet Systems* [in Russian], Énergoatomizdat, Moscow (1984).
[3] M. N. Wilson, *Superconducting Magnets* (Oxford University Press, London, 1983) [Russ. transl. Mir, Moscow, 1985].
[4] V. S. Zarubin, *Engineering Methods of Solving Heat Conduction Problems* [in Russian], Énergoatomizdat, Moscow (1983).
[5] V. M. Paskonov, V. I. Polezhaev, and L. A. Chudov, *Numerical Simulation of Heat and Mass Exchange* [in Russian], Nauka, Moscow (1984).
[6] I. G. Kozhevnikov and L. A. Novitskiĭ, *Thermophysical Properties of Materials at Low Temperatures* [in Russian], Mashinostroenie, Moscow (1982).
[7] V. R. Romanovskiĭ, Izv. Akad. Nauk. SSSR Ser Énerg. Transport, No. 1, 104 (1986).

Translated by R. M. Durham

Evolution of rf instability in a steady-state plasma accelerator

V. I. Brukhtiĭ and K. P. Kirdyashev

Institute of Radio Engineering and Electronics, Russian Academy of Sciences, Fryazino
(Submitted September 5, 1996)
Pis'ma Zh. Tekh. Fiz. **23**, 37–41 (May 26, 1997)

For the first time experimental data are obtained which indicate a stable relation between the microwave radiation intensity of a steady-state plasma accelerator and the rate of bulk erosion of the accelerating channel walls. The frequency range of the electromagnetic radiation corresponds to the excitation of a specific beam instability of the plasma flux at the edge of the accelerating channel, caused, in the opinion of the authors, by electron emission from the eroded part of the dielectric walls.
[S1063-7850(97)02405-1]

The requirement for prolonged operation of plasma accelerators under bench test conditions and for experiments in space has focused particular attention on the stability of their electrophysical parameters and on the permissible levels of fluctuations and electromagnetic fields, which restrict the operating reliability of these accelerators and their electromagnetic compatibility with spacecraft systems. Recording the characteristics of wave processes is also of interest in its own right for diagnostic purposes and for optimizing operating conditions. The results of tests[1,2] indicate that non-steady-state wave processes occur in plasma accelerators, caused, in our opinion, by changes in the emission properties of the eroded surface of the accelerating channel walls. The proposed mechanism for these non-steady-state wave processes is based on the results of prolonged testing and on a connection between the parameters of the fields of the excited plasma beam instability and the rate of erosion.

We report results of 2000-h tests on a steady-state plasma accelerator operated under conditions of constant discharge current and voltage, magnetic field, and pressure in the vacuum chamber of the test rig. The tests were carried out on an experimental prototype of the T-100 plasma engine[3] in the nominal 1.35 kW regime. Measurements were made of the intensities of the spectral components of the fields in the 1.05–7.15 GHz and 13.3 GHz frequency ranges using a radio receiver installation and a procedure developed in Ref. 4. The envelope of the rf signal at the exit from the measuring detectors and the oscillations in the discharge circuit and in the cathode–compensator plasma were also recorded in the 10 kHz–1 MHz frequency range. Periods of continuous testing for 100–300 h were alternated with calibration measurements made with a standard radiation source, which allowed us to take into account the influence of sputtering of the structural material of the plasma accelerator on the radio receiving antennas mounted in the vacuum chamber. Observations were made of changes in the structure of the exit section of the accelerating channel, caused by erosion of the dielectric walls, and the erosion rate was estimated for various stages of the testing. The erosion rate was characterized by the values of $\Delta V_{\rm er}/\Delta\tau_{\rm st}$, determined from the change in volume $\Delta V_{\rm er}$ of the eroded part of the walls for a test period of duration $\Delta\tau_{\rm st}$ (allowing for the cross-sectional configuration and the depth of this region in the radial and longitudinal directions at the external and internal walls of the channel). The parameter $\Delta V_{er}/\Delta\tau_{st}$ describes the integrated effects of the change in structure and damage to the walls, so that this value can be compared with the spectral density of the electromagnetic radiation from the region of plasma flux adjacent to the external wall, with evolving electron instability.[5]

The results of the measurements were used to determine the spectral and energy parameters of the excited electromagnetic fields and the characteristics of the radiation envelope for time intervals of 1–5 ms, during which their statistical properties are revealed. Electromagnetic radiation pulses of random intensity and repetition period are observed depending on the test duration and the state of the accelerating channel walls (Fig. 1). The characteristic instability time scales, determined from the correlation functions of the electromagnetic radiation envelopes at various frequencies, are 80–100 μs, regardless of the test duration and the frequency of the excited fields. A pulsed instability component is typically observed at a specific stage in the tests corresponding to a transition from ion sputtering of the dielectric walls to anomalous erosion.[6] At the initial stage of the tests the excitation of electromagnetic noise is a quasiequilibrium process. A pulsed component is then observed with an intensity maximum at frequencies of 1.0–1.5 GHz, corresponding to electron plasma oscillations of the outer region of the plasma flux. When the walls exhibit an advanced erosion structure, the spectrum of excited oscillations is increased to 2–3 GHz and instability propagates inside the accelerating channel. In this case, the flux density of the radiation pulses increases at given time intervals, and may overlap in time, leading to an increase in the total intensity of the excited electromagnetic field.

Significantly, a stable relation is obtained between the electromagnetic radiation intensity in the 1–2 GHz frequency range and the rate of bulk erosion of the walls of the accelerating channel (Fig. 2). The maximum radiation intensity is observed after test times of 700–1200 h, when the walls have a clearly defined erosion structure. It follows from the wear behavior established in Ref. 7 for an insulator, that for the walls of the accelerator channel the change in the depth of the erosion region is described by: $h(t)=\alpha\beta t/(1+\beta t)$, where $\alpha=13$–15 mm/h and

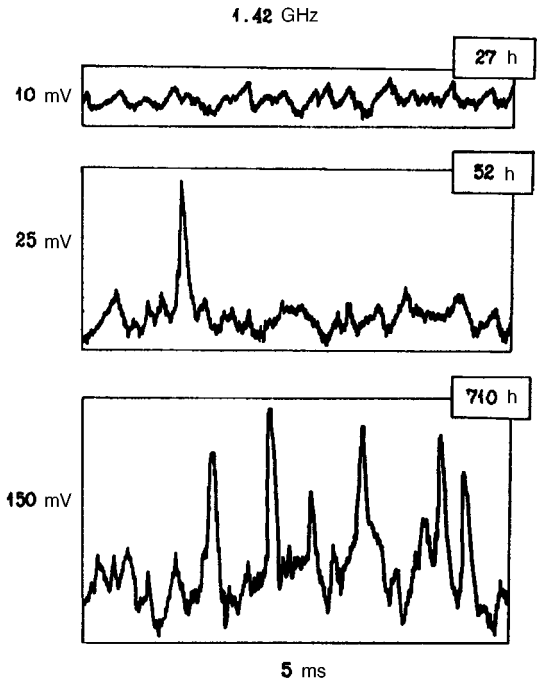

FIG. 1. Examples of the rf signal envelope at the output of the measuring detectors at the maximum of the electromagnetic radiation spectrum at various stages of testing.

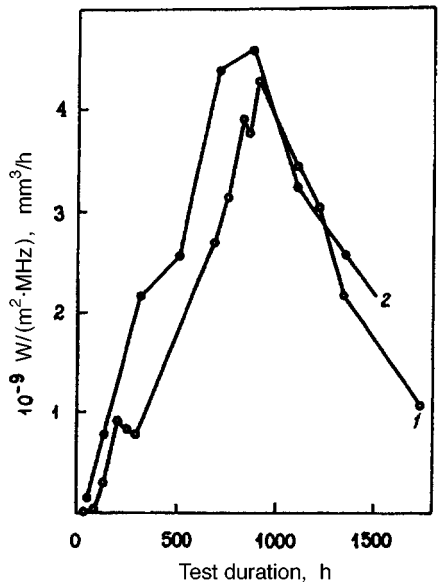

FIG. 2. Time dependences of the electromagnetic radiation intensity of the plasma accelerator (*1* — W/cm^2·MHz) and rate of bulk erosion of the accelerating channel walls (*2* — mm^3/h).

$\alpha = 1.02–1.06\ \text{h}^{-1}$ are the experimentally determined parameters of the wear model. On examining the bulk effects, it can be shown that the parameter $\Delta V_{er}/\Delta \tau_{st}$ has the highest values for test periods with the maximum radiation intensity.

On the basis of these results, the mechanism of the plasma-surface interaction can be considered to be a sequence of damage events on the walls of the accelerating channel, accompanied by the emission of electrons, and by the generation of local sources of fluctuations in the plasma flux and the formation of an electromagnetic radiation field. The duration of the emission process caused by the anomalous erosion is determined by the relaxation of nonequilibrium excited states at newly formed cleavages and cracks in the erosion structure and, according to the experimental results, does not exceed 1 ms. The electric fields required for the evolution of beam instability are determined by the negative sections of the charge mosaic of the dielectric walls, where the electrons are accelerated to 300–1000 eV (Ref. 8).

We note that the spectral and energy characteristics of the wave processes in the wall region of the plasma flux may be used to estimate the rate of erosion of the accelerating channel walls and to predict the operating life of plasma accelerators.

The authors would like to thank Yu. I. Balkareĭ for useful discussions of the results, and also M. V. Yasinskiĭ, V. L. Zarembo, and O. É. Svetlitskaya for assisting in the experiments and in the analysis of the results.

[1] V. I. Brukhtiĭ, K. P. Kirdyashev, V. L. Zarembo, and O. É. Svetlitskaya, Zh. Tekh. Fiz. **66**(2), 68 (1996) [Tech. Phys. **41**, 149 (1996)].
[2] V. I. Brukhty, K. P. Kirdyashev, and O. E. Svetlitskaya, *Summaries of Abstracts of Papers presented at 24th International Conference on Electric Propulsion*, Moscow, 1995, pp. 116–117.
[3] V. I. Baranov, A. I. Vasin, Yu. S. Nazarenko, V. A. Petrosov *et al.*, Pis'ma Zh. Tekh. Fiz. **20**(5), 72 (1994) [Tech. Phys. Lett. **20**, 210 (1994)].
[4] K. P. Kirdyashev, *Radio-Frequency Wave Processes in Plasma-Dynamic Systems* [in Russian], Énergoatomizdat, Moscow (1982), p. 142.
[5] J. P. Bugeat, Yu. A. Ermakov, V. L. Zarembo, and K. P. Kirdyashev, *Abstracts of Papers presented at the Second German-Russian Conference on Electric Propulsion Engines and Their Technical Applications*, Moscow, 1993, p. 38.
[6] B. A. Arkhipov, R. Yu. Gnizdor, N. A. Maslennikov, and A. I. Morozov, Fiz. Plazmy **18**, 1241 (1992) [Sov. J. Plasma Phys. **18**, 641 (1992)].
[7] V. I. Baranov, A. I. Vasin, and V. A. Petrosov, in *Space Rocket Engineering* [in Russian], publ. by Scientific Research Institute of Thermal Processes, Moscow No. 3(131) (1991), pp. 54–70.
[8] M. I. Molotskiĭ, *Abstracts of Papers presented at First All-Union Scientific Conference on Exoelectronic Emission and Its Applications*, Sverdlovsk, 1979 [in Russian], pp. 125–128.

Translated by R. M. Durham

Formation of dense electron beams in a gun with a plasma anode based on a reflecting discharge

G. E. Ozur, D. I. Proskurovskiĭ, D. S. Nazarov, and K. V. Karlik

Institute of High-Current Electronics, Siberian Branch of the Russian Academy of Sciences, Tomsk
(Submitted July 23, 1996)
Pis'ma Zh. Tekh. Fiz. **23**, 42–46 (May 26, 1997)

A method of obtaining low-energy, high-current electron beams in a gun with a plasma anode based on a reflecting discharge is proposed and implemented for the first time. © *1997 American Institute of Physics.* [S1063-7850(97)02505-6]

Sources of low-energy (10–40 keV), high-current (>10 kA) electron beams developed so far[1,2] have been actively used to modify surface layers of materials.[3–5] The electron gun in these sources incorporates an explosive-emission cathode and a plasma anode consisting of parallel arc sources, distributed in a circle around an opening in the anode. The arc is excited by high-voltage pulse breakdown over the surface of a dielectric. The anode plasma generated by the arc sources usually fills the accelerating gap (diode) and the beam drift space in a few microseconds. An accelerating voltage pulse of up to 40 kV is then applied to the cathode, exciting explosive electron emission with the formation of a dense cathode plasma. The accelerating voltage is concentrated in the double layer between the cathode and anode plasmas, in which the electron beam is formed. The beam passes through the opening in the anode and is transported in the plasma to a collector. Prefilling the diode and the drift space with plasma rapidly increases the electric field strength at the cathode (prior to the excitation of explosive emission) and the electron beam perveance compared with a vacuum diode.[1,2] The system is placed in a guiding magnetic field to prevent pinching of the beam. Beams with currents up to 40 kA, durations up to 5 μs, and diameters up to 8 cm have been obtained with these sources.

However, the use of a vacuum-arc erosion plasma has various shortcomings. The erosion products (vapor, plasma, microparticles) may contaminate the surface layer of the material being treated and microparticles may even cause spallation. The stability of the parameters of an erosion plasma is inferior to that of a gas-discharge plasma because of the transient nature of the electrode erosion in the arc. In addition, since the arc is initiated over the surface of a dielectric, the stability of the resultant plasma parameters depends strongly on the state of the surface (for example, on the quantity and composition of material deposited on the surface as a result of electron-beam erosion of the collector). As a result, the instability of the beam energy density at the collector may be as high as 30%. If a long plasma channel is required, additional plasma sources must be provided in the drift space, which lowers the reliability and makes the design of the electron gun more complex. Finally, the energy used in generating the anode plasma is fairly high, since the total current in the arc sources is usually comparable to the current in the diode,[2] although only the ion component of the current from the anode plasma is used to form the beam.

We have developed an electron gun in which the anode plasma is formed by means of a pulsed negative (Penning) discharge, reminiscent of a glow discharge. The electron gun is shown schematically in Fig. 1. The beam collector and the explosive-emission cathode of the electron gun form the cathodes of the Penning discharge. The anode is a hollow cylinder having an inner diameter of 9.4 cm and a length of 11 cm. Gas (N_2 and Ar) was admitted continuously by means of an SNA-2 leak valve and the gas pressure was monitored with a PMI-2 ion gauge. The discharge was supplied by a 0.5μF capacitor, charged to 4–5 kV, via a controllable air spark gap. The discharge current was limited by a ballast resistor ($R_3 \simeq 96$–$330\ \Omega$) and was monitored by the use of a shunt ($\sim 1.5\Omega$). The discharge voltage was recorded by a resistive divider. The accelerating voltage pulse was formed, as in Refs. 1 and 2, by discharging a storage capacitor ($C=3\mu$F) across a controllable spark gap to the diode. The diode and beam currents were recorded with Rogowski loops and the voltage across the diode was measured with a resistive divider R_1, R_2. The beam energy was measured with a calorimeter consisting of a copper absorber and a KMT-8 thermistor. The external magnetic field was ~ 0.24 T.

We first studied some of the discharge characteristics. Figure 2 shows typical oscilloscope traces of the discharge current and the voltage across the discharge gap (a) and also gives the delay time before ignition of the discharge as a function of the gas pressure (b). These curves were then used to synchronize the time of application of the accelerating voltage to the cathode with the discharge burning. The statistical spread of the delay times before ignition of the discharge did not exceed $\pm 5\%$ for pressures of $>4\times10^{-2}$ Pa. Assuming that the degree of ionization of the gas in the discharge is $\sim 50\%$ (Ref. 6), we find that at a pressure of 8×10^{-2} Pa the plasma concentration reaches 10^{13} cm^{-3}.

The results of calculations[7] were used to estimate the electric field strength at the cathode E_c before the excitation of explosive emission. At an accelerating voltage of 10 kV, the field E_c is ~ 80 kV/cm. Nevertheless, despite this quite moderate value of E_c, the emission properties of cathodes made of graphite or a bundle of copper wires proved satisfactory, judging by the signatures on stainless steel foil.

Figure 3 shows typical oscilloscope traces of the voltage across the diode, the current in the diode, and the beam current at the collector. It can be seen that the current at the collector is considerably smaller than that in the diode. We attribute this to current leakage caused by ignition of a parasitic volume discharge near the cathode holder and break-

 1063-7850/97/050393-02$10.00

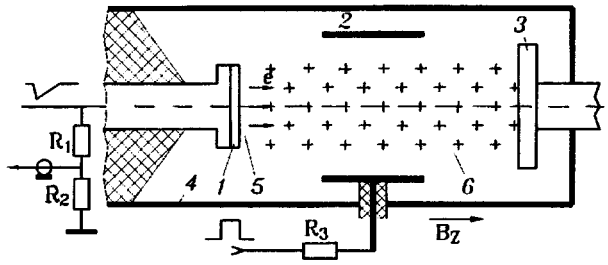

FIG. 1. Diagram of electron gun: *1* — cathode, *2* — anode, *3* — collector, *4* — chamber, *5* — cathode plasma, *6* — anode plasma, R_1, R_2 — voltage divider, and R_3 — ballast resistor.

down over the diode insulator. This shortcoming may be eliminated by changing to a pulsed method of gas supply. For a stored energy of ~1.3 kJ, a beam energy of ~200 J has now been achieved, which is ~15% of the stored energy. The track left by the beam on stainless steel foil was a uniformly molten surface, with a diameter of 8 cm.

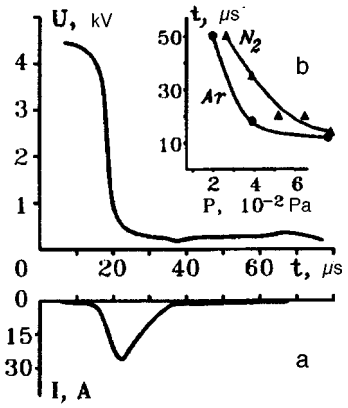

FIG. 2. a— Oscilloscope traces of voltage across discharge gap and discharge current. b— Discharge ignition time versus pressure in discharge gap for nitrogen (R_3=330 Ω) and argon (R_3=96 Ω).

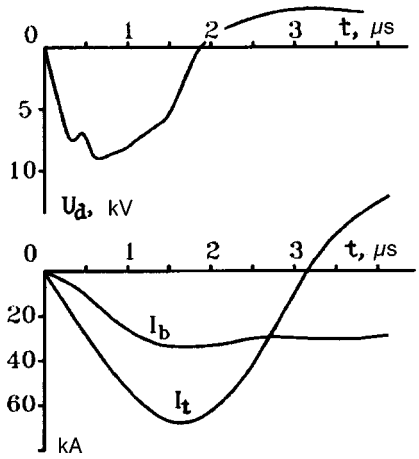

FIG. 3. Oscilloscope traces of voltage across diode U_d, beam current I_b, and total current I_t. Working gas — argon, pressure ~8×10^{-2} Pa, and capacitor charging voltage — 30 kV.

To sum up, we have proposed and implemented a method of obtaining low-energy, high-current electron beams in a gun with a plasma anode based on a reflecting discharge. The use of argon as the working gas can improve the purity of the surface treatment of materials.

[1] G. E. Ozur and D. I. Proskurovskiĭ, Pis'ma Zh. Tekh. Fiz. **14**, 413 (1988) [Sov. Tech. Phys. Lett. **14**, 184 (1988)].
[2] D. S. Nazarov, G. E. Ozur and D. I. Proskurovskiĭ, Izv. Vyssh. Uchebn. Zaved Fiz. No. 3, 100 (1994).
[3] V. I. Itin, I. S. Kashinskaya, S. V. Lykov *et al.*, Pis'ma Zh. Tekh. Fiz. **17**(5), 89 (1991) [Sov. Tech. Phys. Lett. **17**, 192 (1991)].
[4] Yu. F. Ivanov, V. I. Itin, S. V. Lykov *et al.*, Fiz. Met. Metalloved. **75**, No. 95, 103 (1993).
[5] A. V. Batrakov, A. B. Markov, G. E. Ozur *et al.*, IEEE Trans. Diel. Electr. Insul. No. 2, 237 (1995).
[6] Yu. N. Abrashitov, V. S. Koĭdan, V. V. Konyukhov *et al.*, Zh. Éksp. Teor. Fiz. **66**, 1324 (1974) [Sov. Phys. JETP. **39**, 647 (1974)].
[7] M. Yu. Kreĭndel', E. A. Litvinov, G. E. Ozur, and D. I. Proskurovskiĭ, Fiz. Plazmy **17**, 1425 (1991) [Sov. J. Plasma Phys. **17**, 825 (1991)].

Translated by R. M. Durham

Near-wall electron instability of a plasma flux

K. P. Kirdyashev

Institute of Radio Engineering and Electronics, Russian Academy of Sciences, Fryazino
(Submitted August 16, 1996)
Pis'ma Zh. Tekh. Fiz. **23**, 47–52 (May 26, 1997)

Experimental data are obtained which indicate some characteristic features of the plasma-surface interaction leading to the emission of electrons from the walls of the accelerating channel and the evolution of a specific beam instability of the plasma flux. © *1997 American Institute of Physics.* [S1063-7850(97)02605-0]

Studies of the stability of the electron-component dynamics in plasma systems with closed electron drift are of particular importance for assessing the contribution of the excited oscillations to the plasma transverse conductivity, and the efficiency of the electron interaction with the walls of the accelerating channel.[1,2] The observed excitation of rf oscillations[3–5] indicates the buildup of plasma electron instability in a range of frequencies and perturbation scales where the drift approximation cannot be applied to describe the dynamics of the plasma electron component. The instability spectrum corresponds to the excitation of electron plasma oscillations, which cannot be explained in terms of existing concepts of the processes taking place in the accelerating region of the plasma flux.

The present paper discusses the results of experimental investigations of rf wave processes in bench tests of the SPD-70 stationary plasma engine[5] and an interpretation is advanced based on scenarios for interaction between the plasma flux and the dielectric walls of the accelerating channel. The fields of the plasma waves were recorded by a probe technique, whereby inductive coupling was incorporated in a two-way rf probe such that the recording part of the probe was dc-decoupled from the measuring device. The use of a floating-potential probe minimized the distortion of the recorded fields in the plasma and eliminated electrical breakdowns via the measuring circuits in the region of the plasma flux with a distributed electric field. The spatial resolution of measuring the plasma wave fields was set by the dimensions of the recording part of the probe ($\sim$1 mm), appropriate to the possible perturbation scales of the rf electric field in the plasma. The frequency characteristic of the probe was highly nonuniform because of the inductive coupling in the rf measuring channel and the influence of shunting capacitors, which cause the probe to exhibit resonance properties in the 3–5 GHz frequency range. In order to eliminate the influence of the frequency properties of the probe on the spectra of the recorded fields in the plasma flux, the spectral measurements of the intensity of the plasma wave fields were made in a standard source — a gas-discharge plasma with a thermal noise level determined by the relation for the spectral energy density:[3]

$$W_0 = kT_e/(12\pi^2 d_e^3 \Delta f),$$

where T_e is the electron temperature, d_e is the electron Debye length, and Δf is the spectral width of the plasma oscillations, which is approximately determined by the effective frequency of electron collisions. For a standard noise source, electron collisions with neutral particles predominate, and for a given gas pressure and electron temperature in the source the value of Δf is $\sim$1–2 GHz. This measuring technique is based on comparing the intensities of the signals recorded during calibration and the measurements and allowing for the nonuniform frequency characteristic of the rf part of the measuring system.

The rf instability spectrum of the plasma flux is concentrated at frequencies of 1–5 GHz, which corresponds to the excitation of electron oscillations in the outer, near-wall region of the accelerating channel with an electron concentration of 10^{10}–2×10^{11} cm^{-3} (according to the probe measurements, the electron density in the central part of the annular cross section of the flux is $\sim10^{12}$ cm^{-3} at a temperature of 10–12 eV). The frequency dependence of the energy flux intensity of the plasma waves, plotted in Fig. 1, was compared with the thermal level

$$S_0 = W_0 v_{Te}\varepsilon^{1/2}/(1-\varepsilon) \approx 4\times10^{-7} f^3 [\mathrm{W/(m^2\cdot MHz)}],$$

where $\varepsilon = 1-\omega_{pe}^2/\omega^2$, ω_{pe} is the plasma electron frequency, and v_{Te} is the thermal velocity of the plasma electrons. This comparison revealed that the spectrum of rf fields in a plasma flux of nonuniform cross section and length contained a region of excitation of oscillations of epithermal electrons, caused by the buildup of instability.

The intensity distribution of the plasma wave fields at different frequencies in the plasma flux cross section indicates that the instability is predominantly localized near the outer wall of the accelerating channel (Fig. 2), whose surface exhibited the greatest anomalous erosion of the dielectric.[6] Less defined plasma instability is observed near the inner wall of the channel. The lengthwise intensity distribution from the edge of the accelerating channel shows a drop in intensity to values corresponding to the thermal level. This behavior may be explained by a mechanism of collisional damping of the plasma waves leaving the region of localized instability.

Experiments involving prolonged testing of a steady-state plasma engine[4] have demonstrated that the plasma electron instability is excited at a specific operating stage of the plasma facility, where the dielectric walls of the accelerating channel have acquired an advanced eroded structure.[6] The instability is of a transient nature, with the spikes in the envelope of rf oscillations having durations of 100–200 μs, substantially longer than the characteristic times of the

 1063-7850/97/050395-02$10.00

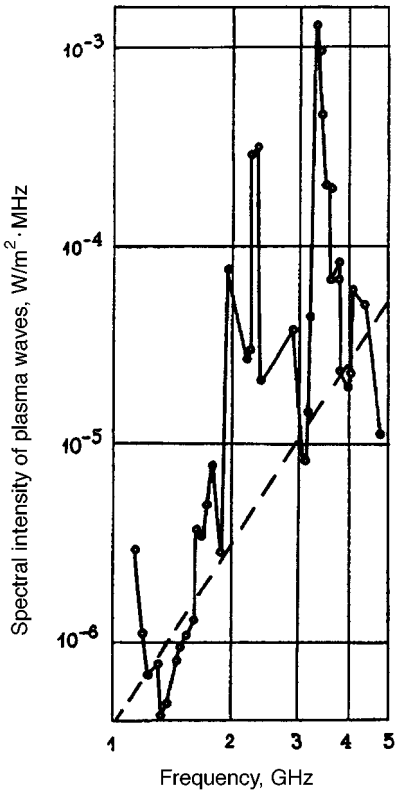

FIG. 1. Spectrum of rf field intensity in the outer near-wall region of the plasma flux (the dashed line gives the frequency dependence of the thermal level of the plasma oscillation intensity at an electron temperature of 10 eV).

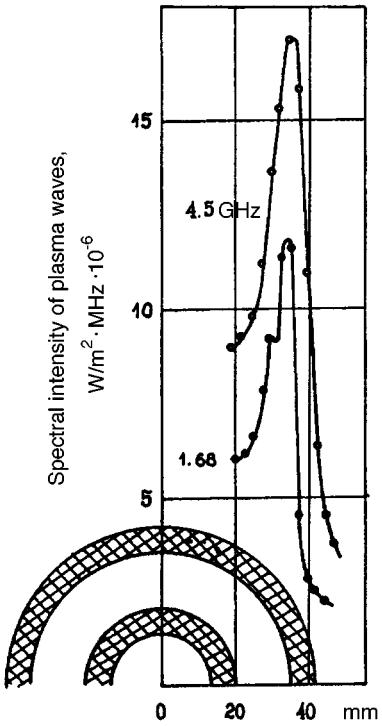

FIG. 2. Intensity distribution of rf fields at various frequencies over the plasma cross section beyond the accelerator edge (showing the configuration of the outer and inner dielectric walls of the accelerating channel).

wave perturbations such as ionization waves, contour and drift oscillations, excited in the accelerating channel. A negligible correlation coefficient is observed for the emission spikes at different frequencies, which may be explained if the electromagnetic field is formed by independent radiation sources from plasma regions of different electron concentration.

These experimental results suggest that emission of electrons from the walls of the accelerating channel plays a key role in the evolution of this specific plasma beam instability. The mechanism of electron emission and acceleration important for this instability is consistent with the concept of the flicker and mosaic property of the Debye potential jump, under conditions where magnetized electrons interact with the walls of the accelerating channel.[1,2] The connection between the observed beam instability and anomalous erosion regimes of the accelerating-channel walls suggests that a mechanism of nonequilibrium electron emission may be involved, caused by damage to the surface and recombination of defects in the structure of the dielectric. The duration of the electron emission is determined by the surface relaxation of the local cleavages and cracks formed during the anomalous erosion of the channel walls. The intensity variation of the rf oscillation spikes is consistent with the time behavior of the emission current from a nonequilibrium excited dielectric surface $j_e(t) \propto t^{-1/2}$ (Ref. 7).

To conclude, these results have extended our understanding of the mechanisms of plasma–surface interaction[2,8] under conditions of plasma acceleration in a channel with dielectric walls. They have also opened up the prospect of diagnostics of erosive processes by means of remote measurements, which will allow us to predict the operating life of facilities and to select structural materials that are stable under prolonged exposure to plasmas.

The author would like to thank A. I. Bugrova and A. I. Morozov for taking part in discussions of the results, and also Yu. A. Ermakov and V. L. Zarembo for assistance with the experiments.

[1] A. I. Bugrova, A. I. Morozov, and V. K. Kharchevnikov, Fiz. Plazmy **16**, 1469 (1990) [Sov. J. Plasma Phys. **16**, 849 (1990)].
[2] A. I. Morozov, *Physical Principles of Space Electric-Propulsion Engines* [in Russian], Atomizdat, Moscow (1997), p. 328.
[3] K. P. Kirdyashev, *Radio-Frequency Wave Processes in Plasma-Dynamic Systems* [in Russian], Energoatomizdat, Moscow (1982), p. 142.
[4] V. I. Brukhtiĭ, K. P. Kirdyashev, V. L. Zarembo, and O. E. Svetlitskaya, Zh. Tekh. Fiz. **66**(2), 68 (1996) [Tech. Phys. **41**, 149 (1996)].
[5] J. P. Bugeat, Yu. A. Ermakov, V. L. Zarembo, and K. P. Kirdyashev, *Abstracts of Papers presented at Second German-Russian Conference on Electric Propulsion Engines and Their Technical Applications*, Moscow, 1993, p. 38.
[6] B. A. Arkhipov, R. Yu. Gnizdor, N. A. Maslennikov, and A. I. Morozov, Fiz. Plazmy **18**, 1241 (1992) [Sov. J. Plasma Phys. **18**, 641 (1992)].
[7] M. I. Molotskiĭ, *Abstracts of Papers presented at First All-Union Scientific Conference on Exoelectronic Emission and Its Applications*, Sverdlovsk, 1979 [in Russian], pp. 125–128.
[8] V. S. Voĭtsenya, S. K. Guzhova, and V. I. Titov, *Action of Low-Temperature Plasma and Electromagnetic Radiation on Materials* [in Russian], Energoatomizdat, Moscow (1991), p. 224.

Translated by R. M. Durham

Negative displacement of bounded flexural wave beams in thin plates

N. S. Shevyakhov

Institute of Radio Engineering and Electronics, Russian Academy of Sciences, Ul'yanovsk Branch
(Submitted November 19, 1996)
Pis'ma Zh. Tekh. Fiz. **23**, 53–56 (May 26, 1997)

The example of flexural waves in a thin plate is used to show that under certain conditions a beam may undergo negative displacement in purely mechanical systems. © *1997 American Institute of Physics.* [S1063-7850(97)02705-5]

An anomalous — negative — displacement of a beam of shear waves reflected by the free boundary of a piezoelectric crystal was predicted in Ref. 1. A similar effect was analyzed theoretically, first in Ref. 2 and then in Ref. 3, for the reflection of a bounded beam of shear waves by a magnetized iron-garnet–vacuum interface. For the case considered in Ref. 1, it was shown in Ref. 4 that during reflection the beam undergoes a negative displacement, i.e., in the direction opposite to the wave propagation along the longitudinal coordinate, because a negative energy flux directed along the boundary and localized near it is formed in the crystal for each monochromatic component of the beam. This energy flux consists of the fields of bulk waves superimposed on the fields of accompanying electric oscillations near the boundary. For the case of flexural waves in a thin plate, it is shown below that this negative displacement of a beam during reflection is by no means typical only of crystals having a complex range of conjugate physical properties (piezoelectric effect,[1] magnetoelastic interaction[2,3]) and is quite feasible under certain conditions in purely mechanical systems (the author cautiously predicts that negative displacement of a beam is a general wave phenomenon which may be observed, not only in acoustics, but also in other fields of physics).

From the most general viewpoint, the results of Refs. 1 and 4 suggest that it is meaningful to make a specific search for the effect of negative beam displacement in materials in which the usual bulk propagation of waves is accompanied by vibrations of some physical nature near the boundary. The second necessary (but not necessarily sufficient) condition for negative beam displacement is that the reflecting boundary should be nonrefracting or nontransparent for the bulk waves. Typical in this respect are thin plates in which, as a specific manifestation of geometric dispersion, the lowest antisymmetric mode — a flexural wave — is accompanied by so-called nonuniform (surface) flexural vibrations at the edges of the plate. These vibrations are an analog of the accompanying surface electric[1] or magnetostatic[2,3] vibrations in crystals. To satisfy the second condition we can choose between a rigidly fixed or free plate edge (nontransparent boundary) and the line of hinged support of an unbounded plate (nonrefracting boundary).

We assume that a thin plate occupies the half-plane xy, $x \leqslant 0$, in the coordinate system xyz and, neglecting shear and rotational inertia as usual,[5] we describe it by the equation

$$D\left(\frac{\partial^4 U}{\partial x^4}+2\frac{\partial^4 U}{\partial x^2 \partial y^2}+\frac{\partial^4 U}{\partial y^4}\right)+\rho h\frac{\partial^2 U}{\partial t^2}=0, \tag{1}$$

where D is the cylindrical rigidity, h is the thickness, ρ is the density, U is the deviation of the plate from the equilibrium position, and t is the time. For oblique incidence of a plane monochromatic flexural wave of amplitude U_0 and frequency ω at the edge of the plate $x=0$, the solution of Eq. (1) for $x \leqslant 0$ is given by:

$$U=U_0 \exp\left[i(k_y y-\omega t)\right] \times\left[\exp(ik_x x)+R\exp(-ik_x x)+A\exp(qx)\right]. \tag{2}$$

Here, R is the coefficient of reflection of the flexural wave, A is the amplitude coefficient of the nonuniform flexural vibrations, decaying inside the plate with the coefficient $q=\sqrt{k^2+k_y^2}$, $k_x=\sqrt{k^2-k_y^2}$, k_y is the projection of the wave vector of the flexural waves on the edge of the plate, and $k=\sqrt{\omega}(\rho h/D)^{1/4}$ is the wave number of the flexural wave.

A rigidly fixed plate edge has the boundary conditions $U|_{x=0}=0$, $\partial U/\partial x|_{x=0}=0$, which, after substituting formula (2) into them, yield the expression

$$R=\exp(i\varphi), \quad \varphi=2\arctan(q/k_x). \tag{3}$$

The longitudinal displacement Δ of a highly directional, cross-sectionally uniform, bounded beam is given by[6]

$$\Delta=-\left.\frac{d\varphi(k_y)}{dk_y}\right|_{k_y=k\sin\theta}. \tag{4}$$

Thus, expressing the phase shift φ of a flexural wave reflected by the edge of the plate as a function of k_y, in accordance with Eq. (3), and substituting it into Eq. (4), we obtain

$$\Delta=-\frac{2\tan\theta}{k\sqrt{1+\sin^2\theta}}. \tag{5}$$

As we hypothesized, the longitudinal displacement of the flexural wave beam for any angles of incidence θ of the beam, as in Ref. 1, is negative: $\Delta<0$. Formula (5) also shows that, except for a region of small angles of grazing incidence $\alpha=\pi/2-\theta$, where the geometric analysis used to derive formula (4) generally ceases to hold, the displacement Δ is still small, even though it is usually several times greater than the negative beam displacement obtained for reflection by the free metallized boundary of a piezoelectric with high electromechanical coupling.[1] However, our hopes of observing the effect are pinned on the fact that, according

to the diffraction theory of the reflection of bounded beams,[7] the displacement Δ has a maximum for grazing angles $\alpha \sim (\omega k)^{-1/2}$, $k\omega \gg 1$, where $|\Delta_{\max}| \sim (\omega/k)^{1/2}$ and ω is the beam width. Thus, if the condition $|\Delta_{\max}| > 102\pi/k$ is satisfied and there are no stringent constraints imposed on the length of the plate (unlike in crystals), the chances of successfully observing negative beam displacement are quite good.

The present case of a plate with a rigidly fixed edge is clearly the most interesting. For an unbounded plate hinged along the line of reflection $x=0$, negative beam displacement does occur but it is half that predicted by formula (5). For a free plate edge the displacement of a bounded beam of flexural waves, estimated according to formula (4), is within the zone of application of this formula (for fairly large grazing angles) and is everywhere positive: $\Delta > 0$. These observations indicate that the dynamic variables $\partial^2 U/\partial x^2$ (bending moment) and $\partial^3 U/\partial x^3$ (intersecting force) of the field of near-boundary flexural vibrations play a reduced role in forming the negative near-boundary energy flux along the line of reflection of the flexural waves in the plate, giving the latter greater kinematic freedom on the line of reflection. We add that the negative near-boundary energy flux along the line of reflection in the plate is mainly formed by the superposition of this dynamic field of near-boundary flexural vibrations on the kinematic (in the variables U, $\partial U/\partial x$) field of the incident and reflected flexural wave.

[1] L. M. Lyamshev and N. S. Shevyakhov, Akust. Zh. **21**, 951 (1975) [Sov. Phys. Acoust. **21**, 581 (1975)].
[2] I. V. Barabanshchikov, L. M. Lyamshev, and N. S. Shevyakhov, *Abstracts of Papers presented at the Ninth All-Union Conference on Acoustics*, AKIN, Moscow, 1977 [in Russian], Part B, pp. 127–130.
[3] V. V. Filippov and O. V. Yan, Dokl. Akad. Nauk BSSR **31**, 213 (1987).
[4] T. N. Marysheva and N. S. Shevyakhov, Akust. Zh. **32**, 413 (1986) [Sov. Phys. Acoust. **32**, 251 (1986)].
[5] S. P. Timoshenko and S. Woinowsky-Krieger, *Theory of Plates and Shells*, 2nd ed. (McGraw-Hill, New York, 1959) [Russ. transl., Fizmatgiz, Moscow, 1963].
[6] L. M. Brekhovskikh, *Waves in Layered Media* (Academic Press, New York, 1960) [Russ. original, USSR Academy of Sciences Press, Moscow, 1957].
[7] O. A. Godin, Zh. Tekh. Fiz. **55**, 17 (1985) [Sov. Phys. Tech. Phys. **30**, 9 (1985)].

Translated by R. M. Durham

Prospects for detection of ultrahigh-energy cosmic rays on the surface of the moon

A. D. Filonenko

East Ukrainian State University, Lugansk
(Submitted August 16, 1996)
Pis'ma Zh. Tekh. Fiz. **23**, 57–62 (May 26, 1997)

A theoretical foundation is laid for the development of a radio detector for cosmic rays with energies $E \geqslant 10^{21}$ eV. The detection system envisages a radio detector on the Earth or a system of radio antennas on artificial lunar satellites, which would record the radio emission pulse produced by a shower in the lunar soil. © *1997 American Institute of Physics.* [S1063-7850(97)02805-X]

One line of research in the physics of cosmic rays involves studying particles in the energy range $W_0 \geqslant 10^{20}$ eV. At the present time, only the existence of these particles is beyond doubt. The lack of information on this energy range is attributable to the lack of detectors, for reasons which have been discussed in greater detail, as in Ref. 1, for instance.

The EAS-1000 and EAS-5000 superprojects (with working areas of 10^3 and 5×10^3 km^2, respectively) are designed to detect particles in the energy range 10^{20}–10^{21} eV. Areas approximately 3–4 orders of magnitude greater are required for the neighboring range of 10^{21}–10^{22} eV, and especially for the 10^{22}–10^{23} eV range. If we are to attempt to solve this problem using the method of radio detection described in Ref. 1, the number of receiving antennas in this detector must be increased by several orders of magnitude, making the installation considerably more complex. The problem is that if the number of antennas is inadequate for such enormous areas ($>10^7$ km^2) there will be no direct line-of-sight between the radiation source (extensive air shower) and the receiving point because of the finite curvature of the Earth's surface. The intensity of the diffracted beam may be several orders of magnitude lower.

Since the working wavelength under atmospheric conditions for highly oblique showers (so that the extensive air shower passes through all its phases of evolution without being absorbed in the soil) will be greater than 10 km, according to Refs. 2 and 3, the detector is affected by strong atmospheric noise from the equatorial thunderstorm belt. This factor (as already discussed in Ref. 1) is another important disadvantage of the method.

These circumstances, combined with various others, have motivated a search for unconventional methods of detecting ultrahigh-energy cosmic rays. The idea of using the surface of the moon as the working area of a ultrahigh-energy particle detector was first proposed in Ref. 4 and then developed in more detail in Ref. 5. According to this concept, the excess negative charge of an electron-photon shower in the lunar soil should stimulate coherent Čerenkov radiation in the radio frequency range, as in the Earth's atmosphere.[6] However, various obstacles seriously impede the implementation of these ideas. One of these obstacles (see Ref. 5) is that the Čerenkov radiation is always directed forward, i.e., in the direction of the particle motion, so that the Čerenkov radiation is only directed toward the Earth for the small fraction of these particles which are incident at grazing angles on a narrow annular zone on the visible side of the moon. This factor reduces the working area of the lunar surface by at least one or two orders of magnitude.

However, this is clearly not the most important factor. A more serious obstacle for the implementation of this project is the multiple scattering of electrons in the shower. It was shown in Ref. 7 that this scattering reduces the intensity of the Čerenkov radiation in a broad atmospheric shower by two or three orders of magnitude. The electrons in an electron-photon avalanche in a condensed medium undergo even greater scattering (approximately a radian per t-unit), so that it is impossible to talk of directional radiation,[5] which is one of the main distinguishing properties of Čerenkov radiation. In addition, the condition of coherent detection changes radically. As a result of scattering, the Čerenkov radiation front will be severely smeared, which will reduce the cutoff frequency of the coherent detection range by several orders of magnitude and thus cause a drop in the radiation intensity.[7]

The minor role of Čerenkov radiation in the general mechanism of emission of extensive air showers is confirmed by the results of almost twenty years of experimental research on this radiation mechanism. This research is reviewed in Ref. 8 which summarizes discussions between groups of researchers in Moscow, Haverah Park, and Bologna. In their opinion, the consensus is that the dominant mechanism for the generation of radio emission in extensive air showers in the meter wavelength range is geomagnetic charge separation.

Estimates of the electric field strength generated by the stopping of δ-electrons in a shower[2,3] show that this radiation mechanism can be successfully used to detect ultrahigh-energy cosmic rays using a radio telescope. When such a particle reaches the surface of the moon, an electron-photon shower develops in the soil. Since the soil is a good insulator, radio emission in the meter range reaches the surface from a depth of several meters with almost no absorption.

Let us estimate the strength of the electric field generated by this lunar shower on the Earth. For this case, expression (9) from Ref. 2 may be reduced to the form (as before $K_1 z_0 < 1$):

$$E(\nu) = q\omega N_0 z_0 \sin\theta/4\pi\varepsilon_0 c^2 f_0, \quad \text{V/m}\cdot\text{Hz}. \tag{1}$$

For lunar soil with a density of 2 g/cm^3, the active path length z_0 of the shower is 2.5 m. We also take

$q=1.6\times10^{-19}$ C, $R_0=0.4\times10^9$ m is the distance from the moon, and $N_0=10^{14}$ (for the initial particle energy $W_0=10^{23}$ eV). To ensure that the coherence condition $K_1z_0=(\omega/c)\ (1-\cos\theta)z_0<1$ is satisfied, we assume $\omega\leqslant0.4\times10^8$ s^{-1} or $\nu\leqslant50$ m·Hz. Then we obtain $E(\nu)=5\times10^{-12}$ V/(m·Hz) or 5 μV/(m·MHz).

Let us compare the useful signal power $P_S=E_\nu^2\Delta\nu^2\varepsilon_0cA$ at the matched load of an antenna with the effective area A to the powers of the signals induced by cosmic sources of radio emission — by a celestial sphere $P_n=kT_A\Delta\nu$ and by brighter point sources in the wavelength range, $P_A=F_\nu\Delta\nu A$, where F_ν is the spectral energy flux (for comparison, from the most powerful point source, Cassiopeia A, at $\nu=50$ m·Hz, the flux is $F_\nu=10^{-21}$ W/(m^2 Hz) (Ref. 9)), $K=1.4\times10^{-23}$ J/K, $\Delta\nu=5\times10^6$ Hz is the bandwidth of the radio receiving system, and $T_A=10^\gamma$ is the noise temperature of the antenna or, in other words, the mean equivalent temperature of the celestial sphere at $\nu=50$ m·Hz. Substituting the appropriate values into these formulas, we find that for $A=100$ m^2, $P_s=2\times10^{-10}$ W, $P_n=0.7\times10^{-12}$ W, and $P_A=0.5\times10^{-12}$ W.

This result shows that an antenna with an area A no greater than 100 m^2 can efficiently record cosmic rays with the energy $W_0=10^{23}$ eV. Since $W_0\sim N_0\sim E_\nu$, for $W_0=10^{22}$ eV we require a telescope of area $A=10^4$ m^2, which is quite commensurate with those currently available.

In this case, the ratio $P_s/P_n=n$, as before, is approximately $n=300$. For particles with $W_0=10^{23}$ eV, n will be $3\times10^\gamma$, and the signal amplitude will be increased tenfold if the mean square amplitude of the galactic noise remains constant. Quite obviously a master signal is not required for this type of detector. It is quite sufficient to have a signal analyzer (for amplitude, shape, and duration) and adequate protection from industrial noise, which can almost always be achieved.

What kind of information can be obtained with this type of radio detector? If mutually perpendicular dipoles are used in the antennas, under favorable conditions, where the electron concentration F of the ionosphere is appreciably reduced (which reduces the depolarization of the signal caused by the Earth's magnetic field), we can reasonably expect some information on the anisotropy of cosmic rays with $W_0\sim10^{23}$ eV.

Despite the prospects for achieving this being not particularly good, there is a definite possibility of determining whether particles in this energy range actually do exist. As yet, this question cannot be answered for sure. It is sufficient to recall the hypothesis of the relict cutoff of the spectrum at 10^{19}–10^{20} eV (Ref. 10). However, if the existence of such high-energy particles (i.e., 10^{22}–10^{23} eV) can be demonstrated experimentally with this type of radio detector telescope, a more detailed study of cosmic rays, not only in this, but also in lower energy ranges, will be an entirely realistic proposition with this method of radio detection. Two or three artificial lunar satellites, each accommodating three mutually perpendicular dipoles with receiving installations, may be used. It is known that this type of antenna system can not only locate uniquely the source of a signal, but also the orientation of its antenna (i.e., the direction of the shower axis in the lunar soil) from the magnitude and polarity of the received signal at each dipole.

Thus, the anisotropy of the cosmic rays can be measured for these ranges and the number of particles in the shower can be determined uniquely using the known amplitude of the signals.

It has been established that the order-of-magnitude area required for the minimum acceptable frequency of events is 10^3, 5×10^4, 10^6, and 5×10^7 km^2, for particles having energies of 10^{20}, 10^{21}, 10^{22}, and 10^{23} eV, respectively. These estimates were obtained assuming that the characteristic of the energy spectrum retains its value $\gamma=2.5$. For observations over these areas the altitude of the satellite above the surface of the moon should be approximately 10, 70, 500, and 1500 km, respectively, for these ranges. Then, the direction to the source will not exceed deviations of more than 60° from the maximum of the angular distribution of the satellite antennas. The corresponding field strengths E_ν for each of these ranges, according to Eq. (1), will be 25×10^{-12}, 40×10^{-12}, 50×10^{-12}, and 125×10^{-12} V/m·Hz, respectively. We find the ratio P_s/P_h assuming that the effective antenna area for a half-wave dipole is $A=\lambda^2/4\pi$. Even for the most unfavorable case ($E_\nu=25\times10^{-12}$ V/m·Hz), substitution gives $P_s/P_h=60$, i.e., the ratio remains fairly high. This favorable scenario is enhanced by the fact that in this method of detection (i.e., directly at the surface of the moon), radio noise of artificial origin is almost completely absent because of the very great distance from the Earth.

To sum up, these estimates have convincingly demonstrated that the radio detection method is extremely promising, but only for very high energies ($W_0>10^{21}$ eV). Although some of the parameters of the radio detector cannot compete with those of conventional methods of detection, as yet no alternatives are available for superhigh energies.

[1] P. I. Golubnichiĭ and A. D. Filonenko, Pis'ma Zh. Tekh. Fiz. **20**(23), 59 (1994) [Tech. Phys. Lett. **20**, 960 (1994)].
[2] P. I. Golubnichiĭ, A. D. Filonenko, and V. I. Yakovlev, Izv. Ross. Akad. Nauk Ser. Fiz. **58**(12), 115 (1994).
[3] P. I. Golubnichiĭ and A. D. Filonenko, Pis'ma Zh. Tekh. Fiz. **20**(12), 57 (1994) [Tech. Phys. Lett. **20**, 499 (1994)].
[4] G. A. Askar'yan, Zh. Éksp. Teor. Fiz. **41**, 616 (1961) [Sov. Phys. JETP **14**, 441 (1961)].
[5] R. D. Dagkesamanskiĭ and I. M. Zheleznykh, JETP Lett. **50**, 259 (1989).
[6] G. A. Askar'yan, Zh. Éksp. Teor. Fiz. **48**, 988 (1965) [Sov. Phys. JETP **21**, 658 (1965)].
[7] A. D. Filonenko, Izv. Ross. Akad. Nauk Ser. Fiz. (in press).
[8] V. E. Atrashkevich, O. V. Vedeneev, H. R. Allan, J. K. Jones, N. Mandolesi, G. Morigi, and G. G. C. Palumbo, Yad. Fiz. **28**, 712 (1978) [Sov. J. Nucl. Phys. **28**, 366 (1978)].
[9] *Handbook of Physical Quantities*, edited by I. K. Kikoin [in Russian], Atomizdat, Moscow (1976).
[10] G. T. Zatsepin and V. A. Kuz'min, JETP Lett. **4**, 78 (1966).

Translated by R. M. Durham

Dynamics of the anode plasma in the magnetically insulated diode of the COBRA ion accelerator by modified laser deflectometry

B. A. Knyazev, J. B. Greenly, D. A. Hammer, E. G. Krastelev, and M. E. Cuneo

Laboratory of Plasma Studies, Cornell University, Ithaca, NY; Novosibirsk State University; Sandia National Laboratories, Albuquerque, NM

(Submitted July 22, 1996)
Pis'ma Zh. Tekh. Fiz. **23**, 63–68 (May 26, 1997)

A new type of optical system for measurements of laser beam deflection has been developed and implemented experimentally. The refractive index gradient in the anode plasma of a megavolt magnetically insulated diode in a high-power ion accelerator has been measured with submicron resolution. The refractive index distribution in the layer was measured during the pulse and the average electron density in the layer was determined. © *1997 American Institute of Physics.* [S1063-7850(97)02905-4]

The characteristics of the anode plasma have a key influence on the composition and parameters of ion beams generated in megavolt magnetically insulated diodes. Nevertheless, these characteristics have not yet been sufficiently well studied because of the obvious difficulties involved in these measurements. A fairly simple method of studying the spatial distribution of the density and composition of the anode plasma involves recording the deflection (and sometimes the deformation) of a laser beam as it passes through a layer parallel to the surface of the anode,[1] although independent data are frequently required for a reliable interpretation of the results. For brevity, we shall call this method, which has been widely used to study objects of very diverse nature (see Refs. 2 and 3), ''deflector diagnostics.''

We have developed a system of deflector diagnostics (Fig. 1) with improved spatial resolution and two recording systems to study the anode sheath in the diode of the new COBRA ion accelerator.[4] The optical system must have a fairly long focus because of the need to reassemble the anode chamber after each shot and because the detectors are positioned some distance away (outside the radiation zone). In accordance with the properties of Gaussian beams,[5] under these conditions the laser radiation can only be focused to a spot of small diameter $2\omega = 2\alpha_L f_{21}/k_1$ ($2\alpha_L$ is the divergence of the laser beam) if the beam has been pre-expanded by an input telescopic system. With an angular magnification of the telescope $k_1 = 6$ and a focal length of the lens $f_{21} = 120$ cm, we obtained a spatial resolution of 0.3 mm over a working length $a = 95$ mm, taking into account the shape of the caustic (see inset to Fig. 1).

After passing through the anode layer, the beam was collimated by a lens L_{22} and split by a beam splitter. The reflected beam was passed through a third telescope, which matched the beam size to the diameter of the photodiode ($2r = 14$ mm), and was then recorded by a photodiode which measured the angle of deflection φ of the laser beam centroid ($a \ll f_{22}$) (Ref. 5):

$$\varphi = \frac{k_1 k_2 \pi \omega_{L0}}{2\sqrt{2 f_{22}}} \frac{\Delta V}{V_L}, \tag{1}$$

where ω_{L0} is the beam radius on entry to the first telescope, f_{22} is the focal length of the lens, and $\Delta V/V_L$ is the relative value of the measured signal. This system of three telescopes is extremely flexible and can easily be adapted to any experimental configurations. The location of mirrors M_1 and M_2, and the positioning of mirror M_1 and lens L_{21} on a common bench is designed so that only the position of the diode must be finely adjusted when moving (paraxially) the beam relative to the anode. To achieve 10% signal linearity, the optical system should also satisfy the condition $k_1 k_2 k_3 \leqslant 2r/((2k+\pi)\omega_{L0})$ (Ref. 5). Under our experimental conditions, the minimum detected angle (less than 0.1 mrad) was determined by the electrical noise level.

A typical oscilloscope trace of the signal from the photodiode is shown in Fig. 2. The positive peak corresponds to the deflection of the beam from the anode which should be observed when the plasma sheath expands away from the anode. The maximum deflection is observed at the end of an 80 ns voltage pulse ($\sim$800 kV) across the diode. The subsequent negative peak may be attributed to an influx of desorbed gas, although a different interpretation is also possible. A series of curves $\varphi(z;t)$ was constructed from the oscilloscope traces obtained for different distances between the beam and the anode, and by integrating these curves over z (Fig. 3), we find the refractive index distribution $\eta(z)$ near the anode:

$$\eta(z) - 1 \simeq \frac{1}{a} \int_{\infty}^{z} \varphi(z)\, dz. \tag{2}$$

It can be seen that at the maximum voltage on the anode ($t \sim 40$ ns), the thickness of the anode sheath is less than 0.5 mm and a lower estimate of the electron density averaged over the beam path at a distance of 0.35 mm from the anode may be given as 3×10^{15} cm^{-3} (here we used the expression $\eta(z) - 1 = \Sigma_j K_j n_j$, where $K_e = -17.95 \times 10^{-23}$ cm^{-3}/atom for the electrons and $K_H = +0.419 \times 10^{-23}$ cm^{-3}/atom for the protons[1]). Assuming that at time $t = 300$ ns the signal is determined only by neutral hydrogen, then at the same distance we have $n_H \sim 1 \times 10^{17}$ cm^{-3}.

The volume of recorded information is enlarged considerably by recording the transverse spatial frequency distribution of the beam after passage through the layer, which can

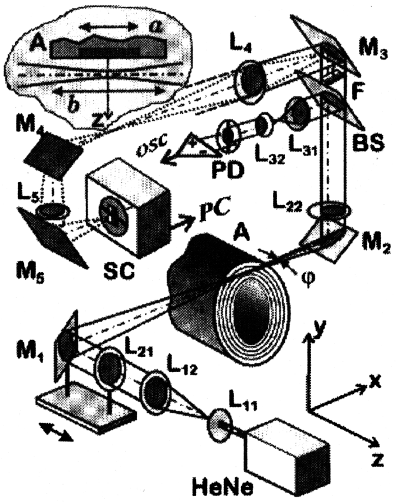

FIG. 1. Diagram of deflector diagnostics with 20 mW He–Ne laser. Telescopic lens systems: L_{11}, L_{12} ($k_1=6$); L_{21}, L_{22} (achromat) ($k_2=0.8$); L_{31}, L_{32} ($k_3=0.45$). *PD* — quadrant photodiode with differential amplifier, M_1–M_4 — mirrors, *BS* — 50% beam splitter, *F* — Fourier plane of lens L_{22}, L_4 and L_5 — achromatic lenses, *SC* — Hamamatsu C2830 streak camera, and *A* — annular aluminum anode of accelerator. Inset — propagation of laser beam along anode through working zone; the plasma generation zone (shown gray) consists of grooves filled with epoxy resin (not shown in the figure): $a=95$ mm, $b=195$ mm.

be performed in this system at the same time as measuring the deflection with the photodiode (this last method is obviously much more sensitive). In our experiments, the intensity distribution of the laser radiation in the Fourier plane (the rear focal plane of the lens L_{21}) was imaged onto the entry slit of a streak camera by lenses L_4 and L_5 and was time-swept (Fig. 2, lower diagram). It can be seen that the spatial frequency spectrum correlates well with the oscilloscope trace. The intensity distribution of the downward deflected beam is slightly asymmetric. If the expansion of the refractive index as a power series could be confined to the term of the second order of smallness, the z distribution of the intensity in the Fourier plane of the lens L_{22} would be symmetric:

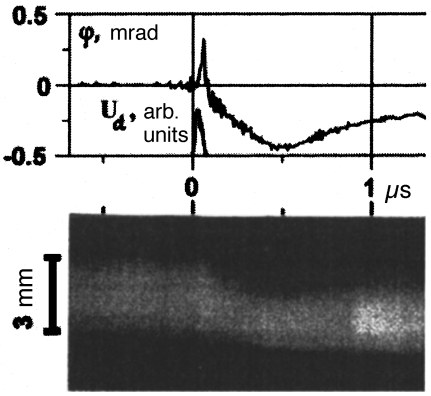

FIG. 2. Oscilloscope trace of photodiode signal and streak camera photograph of the laser radiation intensity distribution in the Fourier plane, obtained in a single shot. Distance between beam axis and anode surface — 0.45 mm, magnification of L_4, L_5 system — 0.8, and effective width of slit — 2 ns. U_d is the voltage pulse at the accelerator anode.

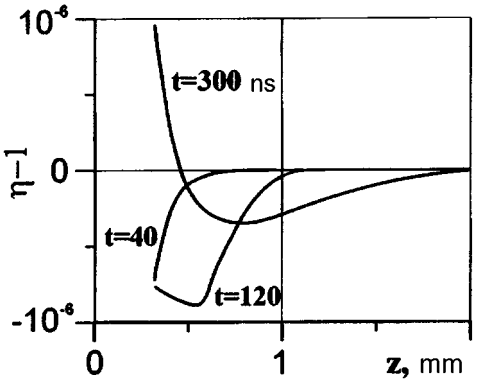

FIG. 3. Refractive index η versus z for three instants of time, reconstructed from a series of twelve oscilloscope traces obtained for different distances between the beam and the anode.

$$\frac{dP(0,z)}{dz}=\frac{2P_L\Delta_y}{\pi\omega_b^2\gamma}\exp\left\{-\frac{2(af\eta'^2-z)^2}{\omega_b^2\gamma^2}\right\}, \tag{3}$$

where P_L is the laser power, $\gamma=(1+k^2a^2\eta'^2\omega^4/4)^{1/2}$, and $\omega_b=2f/k\omega$. In other words, in such a case, the beam is deflected but remains Gaussian with the width $\omega_b\gamma$. The excess observed by us indicates that the variation of $\eta(z)$ within the beam is a higher-order function.

In principle, $\eta(z)$ can be calculated for our geometry by solving an ill-posed inverse problem. However, it is more promising to determine $\eta(z)$ in one pulse by using a broad beam (covering the entire width of the anode layer) and simultaneously recording its intensity distribution at the exit from the layer (front focal plane) and in the rear focal plane of the lens L_{22}. In this case, the phase distribution of the beam leaving the layer (and consequently $\eta(z)$) may be reconstructed, at least for some types of distribution, by some iteration procedure.[6] This requires some modification of the system to simultaneously project both these planes onto the streak camera slit.

The authors would like to thank F. Lindholm for assisting with the experiment, and A. N. Matveenko and V. S. Cherkasskiĭ for useful discussions. The work was supported by a grant from Sandia National Laboratories AF-1660. Some aspects of the diagnostics were developed on the CATRION facility with financial support from the Russian Ministry of Science (Reg. No. 06-06), a grant from the State Committee for Higher Education, No. 95-0-5.2-185, and the Russian Universities Program.

[1] M. E. Cuneo, T. R. Lockner, and G. C. Tisone, IEEE Trans. Plasma Sci. **PS-19**, 800 (1991).
[2] G. G. Dolgov-Savel'ev, B. A. Knyazev, and E. P. Fokin, Zh. Prikl. Spektrosk. **20**, 805 (1974).
[3] C. L. Enloe, R. M. Gilgenbach, and J. S. Meachum, Rev. Sci. Instrum. **58**, 1597 (1987).
[4] D. L. Smith, D. Ingverson, L. F. Bennet *et al.*, *Proceedings of the IEEE Pulsed Power Conference*, 1995 (to be published).
[5] B. A. Knyazev, J. B. Greenly, and D. A. Hammer, *''Refractive index gradient diagnostics: analysis of different optical systems and application to intense ion beam studies,''* Report No. LPSO1-96, Laboratory of Plasma Studies, Cornell University, Ithaca, NY (1996).
[6] J. R. Fienup, Appl. Opt. **21**, 2758 (1982).

Translated by R. M. Durham

Autocompensation of an ion beam in an accelerator with an anode sheath

A. A. Bizyukov, A. E. Kashaba, K. N. Sereda, A. F. Tseluĭko, and N. N. Yunakov

Kharkov State University
(Submitted November 19, 1996)
Pis'ma Zh. Tekh. Fiz. **23**, 69–73 (May 26, 1997)

Experiments to study the autocompensation of an ion beam are described. It is shown that in accelerators with an anode sheath and isolated collector, autocompensation occurs as a result of the excitation of an auxiliary non-self-sustained gas discharge. © *1997 American Institute of Physics.* [S1063-7850(97)03005-X]

At low gas pressures the efficient action of an ion beam on a dielectric surface is impeded by the surface charge generated by the beam which leads to stopping of the impinging ions. The deleterious effect of surface charge is usually eliminated by charge neutralization of the ion beam, using auxiliary sources to inject electrons or negative ions into the ion beam.[1] In the present paper we investigate the current autocompensation of an ion beam in an accelerator with an anode sheath[2] by means of an auxiliary magnetron gas discharge[2] formed at the exit slit outside the ion source, with an isolated beam collector. The auxiliary discharge was excited by means of the characteristic geometric and design features of this type of ion source, which has found widespread application in plasma process systems.

Experiments to study beam autocompensation were carried out using a standard ''Radikal'' anode-source ion source[3] with a cylindrical beam 10 cm in diameter. The dielectric surface was simulated by a dc-decoupled metal beam collector at the floating potential measured with an electrostatic voltmeter. The range of operating voltages of the source was $V_p=1$–5 kV, which corresponded to a maximum of the energy distribution function of the ion beam, $W_{i\max}=(0.3$–$0.4)eV_p$. The working pressure p in the beam transport space was maintained between 8×10^{-5} and 6×10^{-4} Torr. The experiment is described schematically in Fig. 1. A characteristic feature of ion sources with an anode sheath is the presence of an external arched magnetic field near the annular exit slit of the source, formed by the magnetically conducting cathodes $C1$ and $C2$. The topology of the magnetic field H and the spatial distribution of its transverse intensity component in the direction of beam propagation are also shown in Fig. 1. The electromagnetic electron trap, formed by the arched magnetic field and cathodes $C1$ and $C2$, is similar to the electromagnetic trap of a planar magnetron.[4] Depending on the positive potential bias of the external secondary plasma relative to ground, we can expect not only confinement of electrons in the external magnetic trap but also the generation of additional charged particles, i.e., the excitation of an auxiliary discharge, similar to the discharge in a planar gas magnetron outside the ion source.

Figure 1 also shows the spatial distribution of the secondary plasma potential in the direction of propagation of the ion beam for an isolated collector at the floating potential (curves *1* and *2*) and for a grounded collector (curve *3*). It can be seen that in the former case the plasma potential has a large positive bias relative to the cathodes (almost equal to the collector potential), which produces a strong longitudinal electric field near the external electromagnetic trap. In order to eliminate penetration of the electric field from the source, the exit slit was also covered with a grounded metal grid. The crossed longitudinal electric field and transverse magnetic field result in the excitation of an auxiliary charge, which is observed as an intense glow outside the exit slit of the source. When the beam collector is grounded, the plasma potential differs little from the ground potential (and thus that of the cathodes), so that conditions for the generation of an auxiliary discharge are not created and this is observed externally as the disappearance of the intense glow outside the source. Thus, an essential condition for the appearance of an external discharge is that the beam collector have a sufficient positive potential V_c relative to ground.

Figure 2a shows the potential V_c as a function of the discharge voltage V_d for various pressures in the ion beam transport space. At low pressures ($p<10^{-4}$ Torr, curve *1*), the collector potential increases proportionately with the accelerating voltage V_d and inversely as the pressure p ($V_c \propto 1/p$). The main drop in the potential V (Fig. 1, curve *1*) and the intense glow are localized in weak magnetic fields. This potential distribution and behavior of the parameters is typical of a high-voltage discharge with an anode sheath in crossed fields. At pressures above 3×10^{-4} Torr (Fig. 2a, curve *2*), the collector potential stabilizes at 200–300 V and

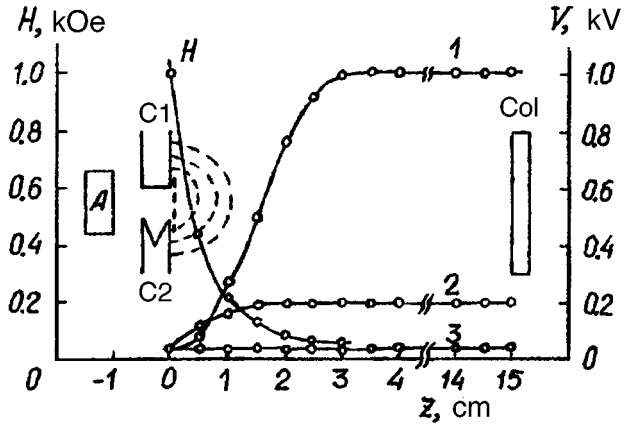

FIG. 1. Spatial distribution of the magnetic field strength H and plasma potential (*1*, *2* — isolated collector, *3* — grounded collector, $V_d=3$ kV; *1* — $p=4\times10^{-4}$ Torr, *2* — $p=4\times10^{-4}$ Torr, *3* — $p=10^{-4}$ Torr and 4×10^{-4} Torr; A — anode, $C1$, $C2$ — cathodes of ion source, G — grounded metal grid, Col — ion beam collector.

 1063-7850/97/050403-02$10.00

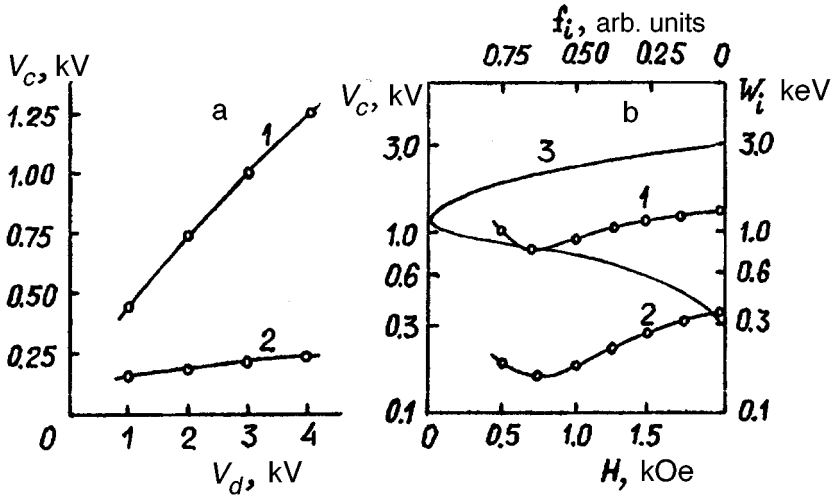

FIG. 2. a — Potential V_c of isolated collector versus ion source voltage V_d (*1* — $p=10^{-4}$ Torr, *2* — $p=4\times10^{-4}$ Torr). b — Potential V_c of isolated collector versus magnetic field H in exit slit gap of ion source (*1* — $p=10^{-4}$ Torr, *2* — $p=4\times10^{-4}$ Torr, $V_d=3$ kV) and beam ion energy distribution function (curve *3*, $V_d=3$ kV).

depends comparatively weakly on the discharge voltage and pressure. Under these conditions, the main drop in potential (Fig. 1, curve *2*) and the intense glow are concentrated in strong magnetic fields. These potential distributions and dependences of the parameters are characteristic of a magnetron gas discharge.

Figure 2b also gives the potential of the isolated ion collector as a function of the magnetic field in the slit of the source. It can be seen that for the high-voltage external discharge (low pressure range, curve *1*) and for the external magnetron discharge (pressures above 3×10^{-4} Torr, curve *2*), there exists a specific optimum magnetic field characteristic for the given type of discharge, which is determined by the design of the source.

It should be noted that the energy used in exciting the auxiliary discharge is drawn from the ion beam energy by the formation of the residual potential V_c at the collector and by the beam ion energy loss $\Delta W_i=q_iV_c$, where q_i is the ion charge. Figure 2b gives the ion energy distribution function at the exit from the ion source (curve *3*) for a grounded beam collector. It is typically found that under magnetron discharge conditions, the beam ions are only slowed comparatively slightly ($\Delta W_i\simeq$ 150–300 eV $\ll W_{i\max}$), whereas in a discharge with an anode sheath, considerable ion energy losses ($\Delta W_i\simeq$ 800–1200 eV $\simeq W_{i\max}$) are accompanied by reflection of a significant fraction of the beam ions of energy below ΔW_i from the isolated collector. The residual potential of the collector is automatically established at a level for which the corresponding type of discharge generates an electron current equal to the ion beam current.[5]

To sum up, we have shown that in accelerators with an anode sheath and an isolated collector, the ion beam undergoes autocompensation as a result of the excitation of an auxiliary non-self-sustained gas discharge outside the ion source, which provides the neutralizing electron current at the surface. At low pressures, a high-voltage discharge with an anode sheath is formed in crossed electric and magnetic fields with a relatively low rate of charged particle generation whereas at high pressure, this changes to a high-efficiency magnetron discharge, providing almost complete current compensation for the ion beam.

[1] M. D. Gabovich, *Physics and Engineering of Plasma Ion Sources* [in Russian], Atomizdat, Moscow (1972).
[2] S. D. Grishin, V. S. Erofeev, and A. V. Zharinov, in: *Plasma Accelerators*, edited by L. A. Artsimovich [in Russian], Mashinostroenie, Moscow (1973), p. 54.
[3] Yu. P. Maishev, Vak. Tekh. Tekhnol. **2**(3/4), 53 (1992).
[4] B. S. Danilin, *Application of Low-Temperature Plasmas for Deposition of Thin Films* [in Russian], Énergoatomizdat, Moscow (1989), pp. 63–120.
[5] A. I. Morozov, *Physical Principles of Space Electric-Propulsion Engines* [in Russian], Atomizdat, Moscow (1978).

Translated by R. M. Durham

Characteristics of microwave beam breakdown in nitrogen and oxygen

G. M. Batanov, I. A. Kossyĭ, N. I. Malykh, A. A. Matveev, A. V. Sapozhnikov, and V. P. Silakov

Institute of General Physics, Russian Academy of Sciences, Moscow
(Submitted December 4, 1996)
Pis'ma Zh. Tekh. Fiz. **23**, 74–80 (May 26, 1997)

The time evolution of the electron density in microwave discharges in nitrogen and oxygen has been investigated. It is shown that the kinetic processes of electron detachment from negative ions or associative ionization of electronically excited gas molecules play a significant role in the interaction between above-threshold microwave radiation and a discharge plasma.
 [S1063-7850(97)03105-4]

In recent studies of microwave discharges in molecular gases, the role of a wide range of elementary processes in the dynamics of the discharge evolution has just started to be considered. So far, the greatest attention has been focused on the role of electron detachment from negative oxygen ions during decay of the plasma.[1–3] It was shown in Ref. 1 for instance, that plasma decay in air is slowed with increasing input energy. In Ref. 2, detachment processes were used to explain an increase in electron density in a non-self-sustained discharge. In Ref. 3, detachment was attributed to reactions with atomic and excited oxygen. Associative ionization processes may also play an important role in the discharge dynamics. It was shown in Refs. 4–7 that associative ionization not only sustains a ''long-lived'' plasma, as was observed in Ref. 8, but also causes an explosive increase in the electron density in a microwave field, which changes the electrodynamics of the discharge. A rapid increase in electron density may also be brought about by attachment processes when negative ions accumulate in discharges containing oxygen or water vapor impurities.[1)] In this context, it is interesting to study the time evolution of the electron density in nitrogen and oxygen discharges in wide-aperture microwave beams. At pressures around 10–20 Torr the discharge in these gases resembles a breakdown wave (see Refs. 9 and 10) and for weakly converging beams, the role of ionization-field instabilities, leading to stratification of the plasma and a critical or above-critical increase in the electron density, is suppressed. It is therefore logical to predict that the role of elementary kinetic processes will be manifested more clearly in these discharges.

The experiments were carried out using 8 mm radiation from a 500 kW gyrotron. A slightly elliptic Gaussian beam of coherent electromagnetic waves was focused by a polystyrene lens into an evacuated chamber, and had the characteristic radius $a_F=1.8$ cm and the characteristic caustic length $l_F=ka_F^2=25$ cm in the focal plane. The working gas pressure (10–20 Torr) and the microwave pulse length were varied during the measurements.

The electron density was determined with an interferometer according to the phase shift of 2 mm diagnostic radiation passed through the plasma. The width of the diagnostic beam was 1 cm and its axis was shifted by 5 cm relative to the center of the caustic, in the direction of the lens.

Oscilloscope traces of the signals from the phase detector of the interferometer (Fig. 1) show that the evolution of the spatially averaged electron density n_e differs under the discharge conditions in nitrogen and oxygen. The nitrogen discharge typically exhibits a rapid rise in electron density at the leading edge of the microwave pulse, followed by a slower rate of increase. The function $n_e(t)$ then passes through a maximum, and decays slowly until the action of the microwave pulse on the plasma has ceased. The electron density then decays exponentially after the pulse. For an oxygen discharge the initial increase in n_e is slower than that in nitrogen, and a more pronounced fall is observed after 1–2 μs (during the action of the electromagnetic radiation). The greatest difference between the nitrogen and oxygen discharges is that the first electron density peak in oxygen is followed by a second and a third, both occurring after the microwave pulse has been switched off (Fig. 1f). For the high, above-threshold, electric field typical of these measurements ($E_0=6$ kV/cm), breakdown of the gas occurs at the leading edge of the microwave pulse. This is indicated by the peak on the leading edge of the signal from a microwave detector positioned on the beam axis at the rear wall of the chamber, characterizing the radiation intensity after passage through the discharge (Figs. 1b and 1e), and also by the steep leading edges of the signals from a photomultiplier (Figs. 1d and 1g), which was installed to record the discharge luminescence from the focal region. An increase in the electron density during breakdown over the entire length of the caustic leads to attenuation of the field in the focal region because of the absorption and refraction of the waves. This evidently has some bearing on the fact that the maximum average electron density is limited to $\sim 2\times 10^{12}$ cm^{-3}. For the observed breakdown waves the maximum values of the function $n_e(t)$ typically showed no dependence on the electric field strength. A threefold reduction in the radiation power caused no change in the average electron density in the first peak.

The effect described can be interpreted quite easily by a purely electrodynamic model of an above-threshold discharge.[9] However, the electron density peak observed in oxygen in the post-discharge period suggests that kinetic processes play an important role in the dynamics of a microwave plasma. In fact, the rise in n_e may be associated with a sharp falloff in the rate of the high-threshold reactions of dissociative attachment of electrons to oxygen atoms (i.e., with degradation of the main channel for production of nega-

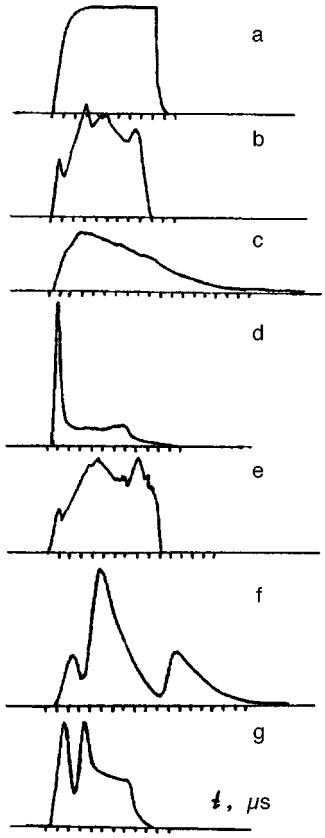

FIG. 1. Oscilloscope traces showing the microwave radiation power signals on the beam axis at the end of the chamber (a, b, e), the phase shift signals from the interferometer (c, f), and the photomultiplier signals (d, g): a — no discharge; b, c, d — nitrogen, 10 Torr; e, f, g – oxygen, 10 Torr.

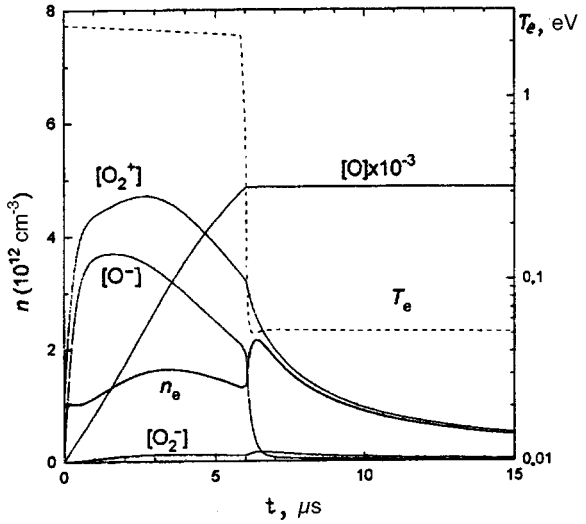

FIG. 2. Results of calculating the parameters of an oxygen discharge for the conditions: $p=10$ Torr, $T_0=300$ K, the gas heating is assumed to be isochoric; $E_0(t)/[O_2]\sqrt{2} = (6.9-3\times10^5 t)10^{-15}$ V·cm^{-2}, and microwave pulse length 6 μs.

tive ions in molecular oxygen in the discharge zone) and with a transition to conditions where detachment of electrons from O^- particles, caused by their interaction with oxygen atoms and electronically excited molecules, predominates over three-particle attachment of electrons to O_2, O, and O_3 particles. The proposed mechanism to explain the electron density peak in the post-discharge period was supported by numerical calculations. The calculations were performed for close to experimental conditions, using a kinetic scheme[11] supplemented by the vibrational kinetic processes of oxygen molecules. The rate constants of the reactions involving electrons were determined by a numerical solution of the Boltzmann transport equation for the electron energy distribution function. The results of one set of calculations are plotted in Fig. 2. It can be seen that the presence of an electron density spike during and after the electromagnetic pulse was substantiated, not only qualitatively but also quantitatively, using this branching kinetic scheme for a freely localized nonequilibrium discharge in molecular oxygen.

It is important to note that the results of the calculations convince us of the universality (for this series of experiments) of this mechanism for the observed electron density peaks during and after the microwave pulse. This statement becomes clear if we analyze the oscilloscope traces of the discharge radiation and the electron density. These traces reveal that drops in the intensity of the optical signal from the discharge, i.e., a decrease in the amplitude of the electric field strength in the discharge zone (caused by the absorption and refraction of electromagnetic waves) are associated with spikes in the average electron density in the oxygen plasma.

Similar results were also obtained for discharges in water vapor, mixtures with nitrogen and oxygen, and in air.

For an above-threshold wave discharge in nitrogen, only one bright plasma luminescence peak is observed (see Fig. 1d) at the leading edge of the electromagnetic pulse. The electron density reaches its maximum 1–1.5 μs after this luminescence peak, i.e., after the field has decayed. We attribute this increase in electron density (with decreasing plasma luminescence) to associative ionization of electronically excited nitrogen molecules (see Refs. 4–8).

A consequence of the space-time variation of the plasma electron density in the discharge should be a spatial redistribution of the microwave field, which should then influence the space-time dynamics of the charge component of the ionized gas. In our case, this redistribution of the field is recorded as a displacement of the focus of the microwave beam in the direction of propagation of the radiation (this effect was observed and studied in detail by I. A. Kossyĭ *et al.* in 1992). An increase in the electric field in the region beyond the focus leads to the formation of ''transfocal'' plasmoids in nitrogen and in oxygen. Interestingly, the largest displacement of the focus of a microwave beam is identified just when the average electron density in the focal plane of the unperturbed microwave beam reaches its maximum. This can be seen by comparing the oscilloscope traces of the signals from the interferometer (Figs. 1c and 1f) and the detector (Figs. 1b and 1e). Ultimately, we find that the kinetic processes of electron detachment from negative ions or associative ionization of electronically excited gas molecules play a significant role in the interaction of the above-threshold microwave radiation and the discharge plasma.

To conclude, the propagation of a breakdown wave generated by a focused microwave beam in oxygen is accompanied by spikes of electron density. The appearance of these

spikes both during and after the discharge is determined by the kinetic processes of electron detachment from O^- particles. No repeated spikes of electron density were identified when studying an above-threshold microwave discharge in nitrogen. An analysis of the breakdown waves in both gases indicated that the discharge plasma strongly influences the propagation of the microwave radiation. This influence was observed as a displacement of the beam focus in the direction of propagation of the radiation and by the formation of transfocal plasmoids.

The authors would like to thank the Russian Fund for Fundamental Research for supporting this work (Project No. 96-02-16162a).

[1)]The possible operation of this mechanism for increasing in the electron density in an air plasma in the post-discharge period was first indicated by O. A. Ivanov (1984, Institute of Applied Physics, Russian Academy of Sciences).

[1] A. L. Vikharev, O. A. Ivanov, and A. N. Stepanov, Zh. Tekh. Fiz. **64**, 1617 (1984) [Sov. Phys. Tech. Phys. **29**, 945 (1984)].
[2] S. V. Golubev, S. I. Gritsinin, V. G. Zorin *et al.*, *Radio-Frequency Discharge in Wave Fields* [in Russian], Gorki (1988), pp. 136–197.
[3] K. V. Baiadze, V. N. Kulikov and V. E. Mitsuk, Abstracts of *Papers presented at Eighth All-union Conference on the Physics of Low-Temperature Plasmas*, Minsk, 1991 [in Russian], pp. 45–46.
[4] V. P. Silakov, Fiz. Plazmy **14**, 1209 (1988) [Sov. J. Plasma Phys. **14**, 708 (1988)].
[5] V. P. Silakov, Preprint No. 10 [in Russian], Engineering-Physics Institute, Moscow (1990).
[6] I. V. Bezmenov, V. V. Rusanov, and V. P. Silakov, Preprint No. 30 [in Russian], M. V. Keldysh Institute of Applied Mathematics, Moscow (1992).
[7] I. V. Bezmenov, V. V. Rusanov, and V. P. Silakov, Tr. Inst. Obshch. Fiz. Akad. Nauk **47**, 74 (1994).
[8] S. I. Gritsinin, I. A. Kossyĭ, V. P. Silakov *et al.*, Teplofiz. Vys. Temp. **24**, 662 (1986).
[9] A. L. Vikharev, V. B. Gil'denburg, A. V. Kim, A. G. Litvak, and V. E. Semenov, *Radio-Frequency Discharge in Wave Fields* [in Russian], Gorki (1988), pp. 41–135.
[10] I. N. Inovenkov, A. V. Kim, E. I. Rakova, V. E. Semenov, and A. E. Chukhin, Preprint No. 271 [in Russian], Institute of Applied Physics, Academy of Sciences of the USSR, Moscow (1990).
[11] I. A. Kossyi, A. Ya. Kostinsky, A. A. Matveyev, and V. P. Silakov, Plasma Sources Sci. Technol. **1**, 207 (1992).

Translated by R. M. Durham

Dynamic chaos in acoustoelectronic systems

V. A. V'yun

Institute of Semiconductor Physics, Siberian Branch of the Russian Academy of Sciences, Novosibirsk
(Submitted January 6, 1997)
Pis'ma Zh. Tekh. Fiz. **23**, 81–85 (May 26, 1997)

The experimental observation and study of dynamic chaos in acoustoelectronic systems is reported. For these investigations we selected an object, well-known in physical acoustics and acoustoelectronics, in which these new nonlinear properties are observed. This work provides further scope for experimental modeling of stochastic self-excited oscillations. © *1997 American Institute of Physics.* [S1063-7850(97)03205-9]

Nonlinear dynamic systems have recently formed the subject of intensive study in physics and other sciences. One interesting result of this research has been the observation of stochastic self-oscillations (or dynamic chaos and strange attractors).[1–5] This phenomenon in various systems is still attracting the attention of researchers.

In the present paper we report room-temperature experimental investigations of piezoelectric-semiconductor (YZ-$LiNbO_3$/*n*-Si) layered structures with external feedback. A layered structure and its proposed circuit diagram are shown in Fig. 1. Electrodes are deposited on the opposite sides of piezoelectric and semiconductor wafers, separated by an air gap of 0.1 μm, to record the voltage of induced by the transverse acoustoelectric effect (this effect occurs as a result of nonlinear acoustoelectronic interaction between semiconductor charge carriers and the electric fields accompanying a surface acoustic wave propagating in the piezoelectric[6]). A surface acoustic wave is excited in the piezoelectric by an interdigital transducer.[7] The voltage induced by the transverse acoustoelectric effect is amplified by a low-frequency amplifier and then fed to an amplitude modulator, which modulates the pump signal V_0 from an rf oscillator. The amplitude-modulated rf signal from the modulator is then fed to the transducer, exciting amplitude-modulated surface acoustic waves at the same frequency. In this external-feedback system the percent modulation is regulated by the amplifier gain and depends on the voltage V_a induced by the transverse acoustoelectric effect at its exit (the transducer incorporated twelve pairs of electrodes, the frequency of the pump signal was 105 MHz, and the amplifier gain was 40 dB).

A piezoelectric-semiconductor layered structure was selected because of its nonlinear acoustoelectronic properties. To obtain optimum nonlinear acoustoelectronic interaction of the surface acoustic waves, bearing in mind the calculations made in Ref. 8, we used an *n*-Si semiconductor with a resistivity of 4 $k\Omega \cdot cm$, whose surface had been etched and oxidized in air at room temperature. With this semiconductor, the transverse acoustoelectric effect acted as a trap, and its voltage relaxed with various characteristic relaxation times when the surface acoustic waves were switched on and off (it was noted in Refs. 9–11 that this property of the transverse acoustoelectric effect is a necessary condition for the onset of relaxation-type self-oscillations of the voltage induced by the transverse acoustic effect).

Stochastic self-oscillations of the transverse acoustoelectric voltage were observed in the kilohertz frequency range with increasing pump voltage V_0 after the system had undergone the following bifurcations. For values of V_0 below 0.9 V, no self-oscillations occurred in the system. At a certain threshold $V_0 = -0.9$ V, regular self-oscillations were observed. These oscillations were initially quasiharmonic, they then became highly nonlinear, and at another threshold $V_0 = 2.1$ V, they changed from regular to stochastic (as a result of the feedback in the system, the onset of self-oscillation was naturally accompanied by self-modulation of the surface acoustic waves).

We recorded the phase portraits and spectral dependences to study the self-oscillations observed in the system shown in Fig. 1. The phase portrait was observed on the screen of an oscilloscope when the voltage V_a and its time derivative dV_a/dt were applied to its plates. The spectral

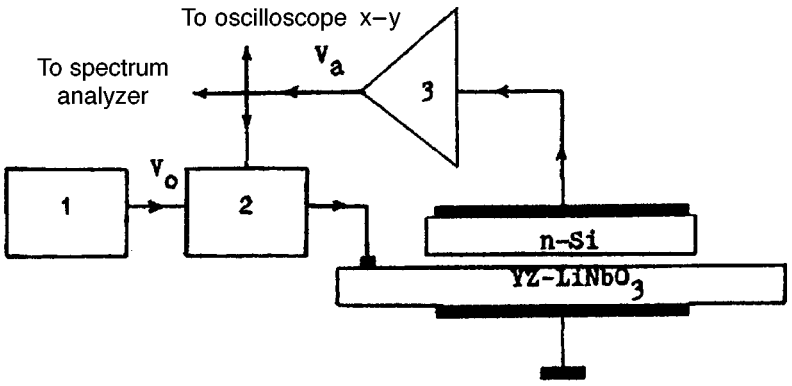

FIG. 1. Diagram of experiment: *1* – rf oscillator, *2* — amplitude modulator, and *3* — low-frequency amplifier.

 1063-7850/97/050408-02$10.00

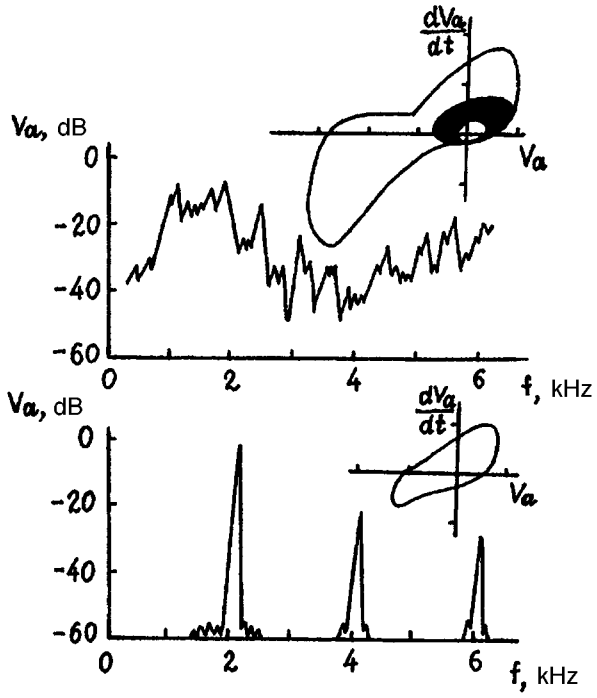

FIG. 2. Phase portraits (scale 2 V/division) and Frequency dependences of the voltage induced by the transverse acoustoelectric effect for stochastic (a) and regular (b) self-oscillations.

dependences were obtained directly with a signal spectrum analyzer. Figure 2 shows the phase portraits and spectral dependences obtained for stochastic self-oscillations at $V_0 = 3.2$ V. Also plotted for comparison are similar curves obtained for regular self-oscillations at $V_0 = 1.1$ V.

It can be seen from the results plotted in Fig. 2 that for stochastic self-oscillations the phase portrait has stable and strange attractors, and the spectrum is continuous (Fig. 2a). This differs from the case of regular periodic self-oscillations, where the phase portrait has only one limit cycle and the spectrum at a frequency of 2 kHz exhibits the fundamental and its harmonics (Fig. 2b). It was established that the transition from regular to stochastic oscillation takes place via intermittence,[12] which is one scenario for the transition to dynamic chaos.

To sum up, stochastic self-oscillations may also occur in acoustoelectronic systems, in addition to the known radiophysical, electronic, semiconductor, and other systems (see Refs. 1–5, 13, and 14). Unlike the simplest phenomenological model of self-oscillations of the voltage induced by the transverse acoustoelectric effect,[9–11] there is clearly a need to take into account several different types of surface states of the semiconductor with different charge relaxation times in order to explain these results. The phase space of these system will then have dimensions greater than two, which is a necessary condition for the onset of stochastic self-oscillations.[1–5]

This work was supported by the Russian Fund for Fundamental Research (Grant No. 96-02-19393).

[1] B. V. Chirikov, Phys. Rep. **52**, 263 (1979).
[2] H. Haken, *Advanced Synergetics: Instability Hierarchies of Self-Organizing Systems and Devices* (Springer-Verlag, New York, 1983) [Russ. transl., Mir, Moscow,1985].
[3] G. M. Zaslavsky, *Chaos in Dynamical Systems* (Harwood, Chur, 1985) [Russ. original, Nauka, Moscow, 1984].
[4] H. G. Shuster, *Deterministic Chaos* (Physik-Verlag, Weinheim, 1984) [Russ. transl., Mir, Moscow, 1988].
[5] Yu. N. Neimark and P. S. Landa, *Stochastic and Chaotic Oscillations* (Kluwer, Dordrecht, 1992) [Russ. original, Nauka, Moscow, 1988].
[6] Yu. V. Gulyaev, A. Yu. Karabanov, A. M. Kmita, A. V. Medved', and Sh. S. Tursunov, Fiz. Tverd. Tela (Leningrad) **12**, 2595 (1970) [Sov. Phys. Solid State **12**, 2085 (1970)].
[7] D. P. Morgan, *Surface-Wave Devices for Signal Processing* (Elsevier, New York, 1985) (Russ. transl., Mir, Moscow 1990).
[8] V. A. Vyun, *Proceedings of the IEEE Ultrasonics Symposium*, Cannes, France, 1994, pp. 441–445.
[9] V. A. V'yun, Pis'ma Zh. Tekh. Fiz. **16**(5), 14 (1990) [Sov. Tech. Phys. Lett. **16**, 169 (1990)].
[10] V. A. V'yun, Poverkhnost' No. 6, 73 (1991).
[11] V. A. Vyun, Lith. J. Phys. **35**, 478 (1995).
[12] P. Manneville and Y. Pomeau, Physica D **1**, 219 (1980).
[13] E. Shöll, *Nonequilibrium Phase transitions in Semiconductors. Self-Organization Induced by Generation-Recombination Processes* (Springer-Verlag, Berlin 1987) [Russ. transl., Mir, Moscow, 1991].
[14] A. S. Dmitriev and V. Ya. Kislov, *Stochastic Oscillations in Radio Physics and Electronics* [in Russian], Nauka, Moscow (1989).

Translated by R. M. Durham

Waveguide properties of optical structures fabricated by oxidation of porous silicon

A. V. Tomov, V. V. Filippov, and V. P. Bondarenko

Institute of Applied Optics, Belarus Academy of Sciences, Mogilev;
Institute of Physics, Belarus Academy of Sciences, Minsk
(Submitted January 28, 1997)
Pis'ma Zh. Tekh. Fiz. **23**, 86–89 (May 26, 1997)

Results of an investigation of the optical properties of channel waveguides fabricated by oxidation of porous silicon are described. The waveguide parameters are estimated and the existence of optical anisotropy is established. The effective refractive index of the dominant quasi-TM waveguide mode is measured. The results suggest that a buffer layer exists between the waveguide and the silicon substrate. It is hypothesized that a second refractive index peak exists within this layer. © *1997 American Institute of Physics.* [S1063-7850(97)03305-3]

Porous silicon has been attracting interest because of its potential for fabricating basic components for optoelectronics devices. This is because intense visible photoluminescence and electroluminescence have been observed in porous silicon.[1] It has also been shown that porous silicon is a promising material for developing efficient photodetectors,[2] and the possibility of waveguide propagation of light in oxidized porous silicon has been demonstrated,[3] although the waveguide properties of these structures have not been studied.

In the present paper we report the first results of a study of the optical properties of channel waveguides fabricated by oxidation of porous silicon.[3] The initial samples were boron-doped silicon wafers having a resistivity of 0.01 $\Omega\cdot$cm. The working side of the wafers was oriented in the (100) plane and was polished to class 14. The silicon wafers were treated in boiling ammonium peroxide solution, washed with deionized water, and dried using a centrifuge in a nitrogen atmosphere. A 0.22 μm thick layer of silicon nitride was then deposited on the working surface of the wafers. Windows comprising stripes 10 μm wide and around 1.5 cm long, were formed in the nitride film by standard techniques of contact photolithography and plasma-chemical etching. After removal of the photoresist and chemical cleaning, the wafers were subjected to anodic treatment in an aqueous solution of hydrofluoric acid (24% by volume). A galvanostatic regime with an anode current density of 10–20 mA/cm^2 was used for the anodization. As a result of the anodic treatment, the sections of the silicon unprotected by the silicon nitride mask were converted to porous silicon to a thickness of around 12 μm. After removing the masking layer of silicon nitride, the wafers underwent three-stage thermal oxidation.[3] This resulted in the formation of a 0.45 μm thick SiO_2 film on the surface and the porous silicon was oxidized to its total depth. Increasing the volume led to the formation of a monolithic oxide channel, 35 μm wide and 13 μm thick, in the porous silicon.

This channel possesses waveguide properties. The waveguide effect was observed when the structure was excited with helium–neon laser radiation via the end and via a prism coupling device.[4] In this case, the surface of the wafer incorporating the waveguide, was prepolished to prevent any oxide expelled from the waveguide channel during oxidation of the porous silicon from projecting along the waveguide boundaries. The prism method allowed us to achieve some degree of selectivity in the excitation of the waveguide modes and to measure their effective refractive indices n_{p1}^*. The mode spectrum was analyzed using the pattern of m-lines in the beam reflected from the base of the prism. In addition, a microscope was used to monitor the mode propagation losses in the waveguide by measuring the radiation intensity from the end. It was observed that more than fifty modes are excited in the waveguide, and these may be divided into two groups with sharply differing levels of propagation losses. The effective refractive index boundary between the groups is near $n_c \approx 1.4460$ for quasi-TE modes. The first group contains the modes lowest in terms of the index p, which propagate with low losses of less than 1 dB/cm (Ref. 3). The second group contains the highest-order modes in terms of p, which were only identified in the reflected beam. This confirms that the waveguide structure incorporates a buffer layer, separating the waveguide from the silicon substrate, which has a high complex refractive index ($n_{si}=3.86-i\times 0.028$). Then, modes having the effective refractive index $n_{p1}^* > n_c$ are guided and weakly attenuated, whereas modes with $n_{p1}^* < n_c$ are leaky. A visual assessment of the light intensity distribution pattern at the end of the excited waveguide indicated that the buffer layer thickness may reach 6 μm. The maximum refractive index $n_{\max}$ of the waveguide was estimated using measurements of n_{00}^* for the dominant, quasi-TE mode. It is known[5] that for a multimode waveguide, these values are similar, i.e., $n_{\max} \approx n_{00}^*$. In our case, $n_{00}^* = 1.4575$, which corresponds to the refractive index of quartz glass. The refractive index increment in the waveguide is $\Delta n = n_{\max} - n_c \approx 115\times 10^{-4}$.

On the basis of the waveguide fabrication technology, it may be assumed that mechanical stresses are induced in the structure, thus producing optical anisotropy. There is also the possibility that crystalline modifications of SiO_2 are formed during the thermal oxidation of the porous silicon. Measurements of the effective refractive index of the dominant quasi-TM mode ($n_{00}^* = 1.4582$) confirmed this assumption. The anisotropy was also studied using a polarizing microscope with a Senarmont compensator for plane-parallel samples of cross sections of the waveguide channel

150 μm thick. The maximum birefringence was observed in the central part of the cross section and was -8×10^{-4}. This is lower by at least a factor of 2 than the birefringence of γ-tridymite — an optically anisotropic phase of SiO_2 with the lowest birefringence of all known crystalline modifications of silicon dioxide.[6]

To conclude, we have estimated the parameters of optical channel waveguides fabricated by oxidation of porous silicon and have established that they possess optical anisotropy. The results suggest that there is a buffer layer separating the waveguide from the silicon substrate. An analysis of the mode spectrum of the waveguide structure and the thickness of this layer suggest that a second refractive index peak may exist within this layer. The results also lead to the conclusion that various high-refracting polymorphic phases of silicon dioxide such as stishovite or the metamict phase[7] (with a modified Si–O–Si bond angle) are not involved in the formation of these waveguides.

[1] S. S. Iyer, R. T. Collins, and L. T. Collins, *Light Emission from Silicon*, Proc. MRS Symposium, Boston, MA, 1992, pp. 256–257.
[2] J. P. Zheng, K. L. Jiao, W. P. Shen, W. A. Anderson, and H. S. Kwok, Appl. Phys. Lett. **61**, 459 (1992).
[3] V. P. Bondarenko, A. M. Dorofeev, and N. M. Kozuchic, Microelectron. Eng. **28**, 447 (1995).
[4] J. J. Danko, and D. P. Ryan-Howard, Appl. Opt. **25**, 1505 (1986).
[5] H. -G. Unger, *Planar Optical Waveguides and Fibres* (Clarendon Press, Oxford, 1977) [Russ. transl., Mir, Moscow, 1980].
[6] *The Oxide Handbook*, edited by V. V. Samsonov (Plenum Press, New York, 1973) [Russ. original, Metallurgiya, Moscow, 1969].
[7] L. M. Landa and I. N. Nikolaeva, Dokl. Akad. Nauk SSSR **244**, 1407 (1979).

Translated by R. M. Durham

Polarization-induced curvature of a laser damage channel

G. M. Mikheev

Institute of Applied Mechanics, Ural Branch of the Russian Academy of Sciences, Izhevsk
(Submitted May 29, 1996)
Pis'ma Zh. Tekh. Fiz. **23**, 90–94 (May 26, 1997)

Significant curvature of a laser damage channel in a metal has been observed and a correlation is reported between this effect and the polarization of the radiation. [S1063-7850(97)03405-8]

It has been established that at sufficiently high powers, laser radiation can pass through a material because the material is removed from the molten zone by evaporation and hydrodynamic effects.[1] A narrow damage channel is formed in the material along the axis of the laser beam even if the angle of incidence of the beam on the surface is nonzero. In some cases however, some deviation of the axial line of the channel (crater) from the normal to the surface has been observed for a normally incident beam.[2,3] This has usually been attributed to error in the coaxial alignment of the laser beam and the optical system.[4] The influence of polarization has not been considered.

In the present paper it is demonstrated that the damage channel formed in a metal by a laser beam incident normally on the surface may exhibit significant curvature and the aim is to establish an interrelation between this effect and the polarization of the radiation.

The influence of polarization on the speed and quality of laser cutting was discussed in Ref. 4. As the material is moved relative to the laser beam a cut is made, whose normal to the surface forms an angle α with the incident beam (see Fig. 1a). The reflectivity of a surface being treated with a plane-polarized beam depends on the optical properties of the material, the angle of incidence of the beam, and the angle between the plane of polarization and the plane of incidence. Let us take R_p and R_s to be the reflection coefficients of the p-component of the polarization, lying in the plane of incidence of the beam, and of the s-component, perpendicular to the plane of incidence, respectively. In accordance with Ref. 4, at the $\lambda = 10.6$ μm wavelength for iron at room temperature, the ratio R_s/R_p tends to unity as α tends to zero and increases substantially as α departs from zero. Thus, when the cutting plane and the plane of polarization of the beam coincide, the absorbed power (and therefore the cutting efficiency) will be substantially higher than when these planes are perpendicular. The polarization of the laser radiation has a similar appreciable influence on the formation of the damage channel. We shall consider a very simple model. We assume that the distribution of the radiation intensity I in the beam cross section is asymmetric and has a clearly defined maximum for $x<0$ (Fig. 1b). When such a beam is incident normally to the surface of the material, the crater formed at the initial stage of interaction between the radiation and the material will have a longitudinal cross section determined by the function $I(x)$ (Fig. 1c). At the next stage of the interaction in time, the beam rays corresponding to the lower-intensity zone will be retroreflected in the direction of the geometric axis of the beam (Fig. 1c). According to the above reasoning, the efficiency of this retroreflection depends on the polarization. If the radiation is polarized in the plane of incidence, the reflection coefficient is low and the absorption high. Thus the shape of the longitudinal cross section of the crater will not change. If the radiation is polarized in the plane perpendicular to the plane of incidence, the reflection efficiency is high and the absorption low. As a result, the retroreflected rays will interact with the opposite

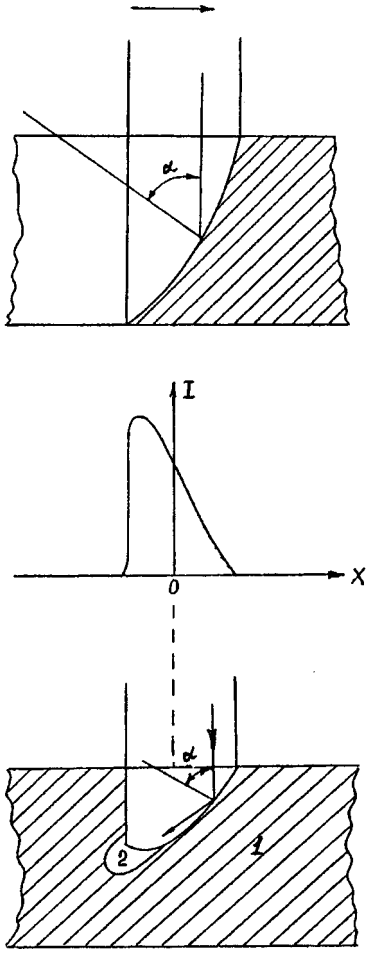

FIG. 1. Diagram showing laser beam cutting of a metal (the arrow indicates the direction of motion of the beam relative to the sample) (a), example of an asymmetric distribution of the laser radiation intensity I along the beam diameter (along the X axis) (b), and corresponding shape of crater longitudinal cross section which may be observed at the initial stage of interaction with the material (c), where *1* is the base metal and *2* is the metal zone which will be removed by the retroreflected rays.

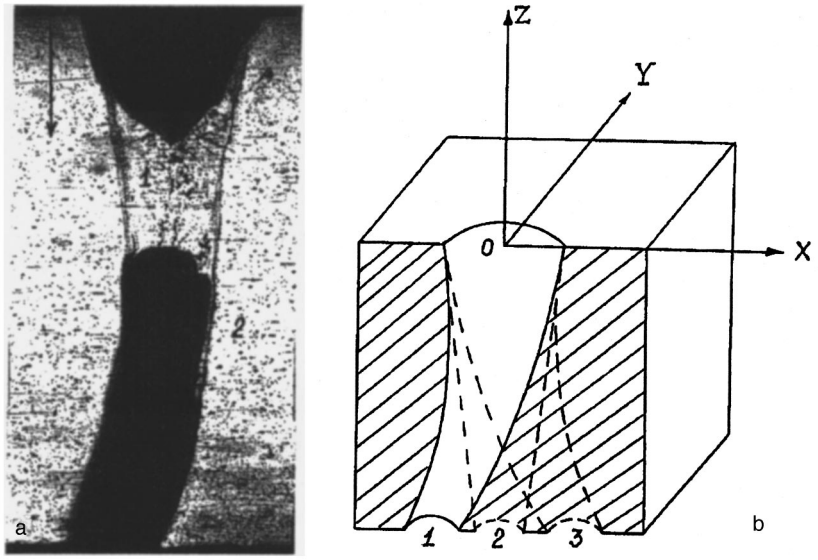

FIG. 2. Experimental shape of longitudinal cross section of laser damage channel (a) (*1* — molten part of channel, *2* — base metal; the arrow shows the initial direction of the beam; magnification ×37) and spatial configuration of the sample relative to the *XYZ* Cartesian coordinate system (b), where profile *2* corresponds to a symmetric distribution of the radiation relative to the axis of the laser beam and profile *1* (*3*) corresponds to an asymmetric distribution with the highest beam power concentrated in the region $X<0$ ($X>0$).

wall of the crater and thereby cause the damage channel to curve in the direction of maximum intensity (Fig. 1c). The real interaction pattern is obviously far more complex.

For the experiments we used linearly polarized pulsed YAG:Nd^{3+} laser radiation, with a pulse length of 4 ms and a maximum pulse energy of 10 J. The radiation was focused by a lens of 0.1 m focal length onto the surface of samples of aluminum alloy 1420 in the form of rectangular parallelepipeds, which were placed in a vacuum chamber at a pressure of 20 Pa. The beam was directed along the normal to the surface of the metal, which coincided with the *Z* axis in the *XYZ* Cartesian coordinates (Fig. 2b). The radiation intensity distribution in the beam cross section was varied by means of special masks placed in the light path before the focusing lens. This type of laser was chosen because, unlike CO_2 laser radiation, the polarization of YAG:Nd^{3+} radiation is easily controlled by half-wave and quarter-wave plates. It should be noted that, on account of its comparatively low thermal conductivity (83 W/m·K at 573 K), the lithium- and magnesium-doped alloy 1420 is superior to other types of aluminum alloys because it is more susceptible to laser damage at lower pulse powers. The laser irradiation was carried out in a rarefied atmosphere to prevent the plasma formed by combustion of the material from having any influence on the laser damage efficiency.

Figure 2a shows a typical profile of the longitudinal cross section of a laser damage channel in the *XZ* plane. The radiation was polarized in the *YZ* plane (Fig. 2b). It can be seen that the radiation propagation channel is significantly curved. The deflection of the beam from its initial direction reaches 30°. The angle of incidence of the radiation on the crater surface varies between 86° and 60°, and the values of $R_s(\alpha)$ and $R_p(\alpha)$ for aluminum, calculated using well-known formulas,[5] decrease according to different laws. When α decreases from 90°, R_s decreases monotonically from 1, with R_s $(\alpha=80°)=0.97$ and $R_s(\alpha=0°)=0.83$, whereas $R_p(\alpha)$ has a minimum of 0.58 for $\alpha=80°$ and then increases to 0.83 for $\alpha=0°$. Thus, the difference between R_s and R_p is greatest near $\alpha=80°$ and remains large for $\alpha=86°$, where $R_s=0.99$, $R_p=0.68$. The experiments have shown that the maximum deflection of the beam from its initial position is observed in the plane perpendicular to the plane of polarization of the light. In the *XZ* plane of curvature, its direction depends on the asymmetry of the radiation intensity distribution along the *X* axis. The curvature is observed in the direction away from the geometric axis of the beam, where the highest radiation power is concentrated. The plane of curvature is determined only by the directions of polarization and propagation, and cannot be changed by varying the power distribution in the beam cross section or by spatial reorientation of the sample.

[1] R. V. Arutyunyan, V. Yu. Baranov, L. A. Bol'shov *et al.*, *Action of Laser Radiation on Materials* [in Russian], Nauka, Moscow (1989).
[2] J. F. Ready, *Effects of High-Power Laser Radiation* (Academic Press, New York, 1971) [Russ. transl., Mir, Moscow, 1974].
[3] S. Kh. Kushnir, B. R. Kiyak, and M. G. Matsko, Ukr. Fiz. Zh. **17**, 1796 (1990).
[4] N. N. Rykalin, A. A. Uglov, I. V. Zuev, and A. N Kokora, *Handbook of Laser and Electron Beam Processing of Materials* [in Russian], Mashinostroenie, Moscow (1985).
[5] V. A. Kizel', *Refraction of Light* [in Russian], Nauka, Moscow (1973).

Translated by R. M. Durham